

UNIVERSITY OF DELHI

DOCTORAL THESIS

Search For Anomalous Gauge Coupling through Vector Boson Scattering and Development of the GEM Detectors at the CMS Experiment

Author:

Ram Krishna Sharma

Supervisor:

Dr. Md. Naimuddin

*A thesis submitted in fulfilment of the requirements
for the degree of Doctor of Philosophy*

in the

Department of Physics & Astrophysics



October, 2018

Declaration

This thesis describes work done by the candidate during his tenure as Ph.D. student at the Department of Physics and Astrophysics, University of Delhi, Delhi, India under the supervision of Dr. Md. Naimuddin. The work reported in this thesis is original and it has not been submitted earlier for any degree to any university.

Candidate
Ram Krishna Sharma

Supervisor
Dr. Md. Naimuddin

Head of Department
Prof. Sanjay Jain



Department of Physics and Astrophysics

University of Delhi

Delhi-110007, India

Date:

Certificate of Originality

The research work embodied in this thesis entitled "**Search For Anomalous Gauge Coupling through Vector Boson Scattering and Development of the GEM Detectors at the CMS Experiment**" has been carried out by me at the **Department of Physics and Astrophysics**, University of Delhi, Delhi, India. The manuscript has been subjected to plagiarism check by **Turnitin** software. The work submitted for consideration of award of Ph.D. is original.

.....
Ram Krishna Sharma

Name and Signature of the Candidate

Student Approval Form

Name of the Author	Ram Krishna Sharma
Department	Department of Physics and Astrophysics
Degree	Doctor of Philosophy
University	University of Delhi
Guide	Dr. Md. Naimuddin
Thesis Title	Search For Anomalous Gauge Coupling through Vector Boson Scattering and Development of the GEM Detectors at the CMS Experiment
Year of Award	

Agreement

1. I hereby certify that if appropriate, I have obtained and attached hereto a written permission/statement from the owner(s) of each third party copyrighted matter to be included in my thesis/dissertation, allowing distribution as specified below.
2. I hereby grant to the university and its agents the non-exclusive license to archive and make accessible, under the conditions specified below, my thesis/dissertation, in whole or in part in all forms of media, now or hereafter known. I retain all other ownership rights to the copyright of the thesis/dissertation. I also retain the right to use in future works (such as articles or books) all or part of this thesis, dissertation, or project report.

Conditions:

1. Release the entire work for access worldwide	
2. Release the entire work for 'My University' only for: 1 Year 2 Year 3 Year and after this time release the work for access worldwide.	
3. Release the entire work for 'My University' only while at the same time releasing the following parts of the work (e.g. because other parts relate to publications) for worldwide access: a) Bibliographic details and Synopsis only b) Bibliographic details, synopsis and the following chapters only c) Preview/Table of Contents/24 page only	
4. View Only (No Downloads) (worldwide)	

.....
Signature of the Scholar.....
Signature and seal of the Guide

Place:

Date:

List of Publications

Journal Publication:

1. "Development, characterization and qualification of first GEM foils produced in India", Aashaq Shah, Asar Ahmed, Mohit Gola, **Ram Krishna Sharma**, Shivali Malhotra, Ashok Kumar, Md. Naimuddin, Pradeep Menon, K. Srinivasan, "*Nuclear Instruments and Methods in Physics Research Section A: Accelerators, Spectrometers, Detectors and Associated Equipment*", 892 (2018), pp. 10-17 (**Corresponding Author**)
2. "Search for anomalous electroweak production of WW/WZ/ZZ boson pairs in association with two jets in proton-proton collision at 13 TeV", CMS Collaboration

To be submitted in: *Physics Letters B*

CMS Analysis Notes:

1. "Search for anomalous electroweak production of WW/WZ/ZZ boson pairs in association with two jets in proton-proton collision at 13 TeV", Aram Apyan, Andrew Beretva, Jeffrey Berryhill, Pietro Govoni, Dan Green, Md. Naimuddin, Jakob Salfeld-Nebgen, **Ram Krishna Sharma**, Patricia Rebello Teles, Davide Valsecchi
CMS Analysis Note - 2017/236.

CMS Detector Notes:

1. "Test beam studies of Gas Electron Multiplier (GEM) detectors for the upgrade of CMS endcap muon system", Vipin Bhatnagar, Brian Dorney, Marek Michal Gruchala, Priyanka Kumari, Ankita Mehta, Md Naimuddin, Jeremie Alexandre Merlin, Archana Sharma, **Ram Krishna Sharma**, J.B. Singh
CMS Detector Note - 16/017.

Conference Proceedings/Poster Presentations:

1. "Test Beam Study of Gas Electron Multiplier (GEM) Detectors for the Upgrade of CMS Endcap Muon System", **Ram Krishna Sharma**.

Talk presented at the **XXII DAE High Energy Physics Symposium**, University of Delhi, India, December 12-16, 2016.

Published Proceeding: **Ram Krishna Sharma** et al. “Test Beam Study of Gas Electron Multiplier (GEM) Detectors for the Upgrade of CMS Endcap Muon System”. In: XXII DAE High Energy Physics Symposium. Springer International Publishing, 2018, pp. 179–183. doi:10.1007/978-3-319-73171-1_40.

2. “Charged particle detection performance of Gas Electron Multiplier (GEM) detectors for the upgrade of CMS endcap muon system at the CERN LHC”, **Ram Krishna Sharma**.

Poster presented at the **2015 IEEE Nuclear Science Symposium and Medical Imaging Conference (NSS/MIC)**, Town and Country Hotel, San Diego, California, USA, 31 October - 7 November 2015.

Published Proceeding: D. Abbaneo,..., **R. Sharma**, et al. “Charged particle detection performance of Gas Electron Multiplier (GEM) detectors for the upgrade of CMS endcap muon system at the CERN LHC”. 2015 IEEE Nuclear Science Symposium and Medical Imaging Conference (NSS/MIC). IEEE, 2015. doi:10.1109/nssmic.2015.7581797.

*Dedicated To
My Respected Parents*

Acknowledgments

It is a matter of immense pleasure to pen down these lines to express my sincere thanks to the people who have bestowed upon me their loving blessings and the heart pledged support because of which I am able to stand where I am today.

First, I would like to express my sincere gratitude to my PhD supervisor Dr Md. Naimuddin, for accepting me as a student. I could not have imagined having a better supervisor and mentor for my PhD study, who not only guided me for the research work but also taught me a lot about life, how to work with different people in a group/collaboration and many more.

Besides him, my sincere thanks also go to our group professors - Dr. Ashutosh Bhardwaj, Dr. Ashok Kumar, Prof. Brajesh Choudhury and Prof. Kirti Ranjan for their guidance and discussion during my PhD study. I gratefully thank Prof. Sanjay Jain, Head, Department of Physics, for allowing me to utilize facilities of the department.

Along with this, I would like to thank Archana Sharma, Dan Green, Jeffrey Berry-hill for their helpful discussion and support during my thesis work.

I would also like to thank INDIA-CMS collaboration for providing me with a platform to discuss my work by arranging regular Collaboration meetings.

This research work has been carried out based on the CMS experiment at the CERN LHC, Fermilab and University of Delhi lab. My endeavour in research got boosted due to the excellent academic, cordial and conversant atmosphere prevailing in these institutions of excellence. I would like to thank the whole CMS collaboration, the scientists, and the technical and the administrative staff at the LHC accelerator complex and the CMS experiment. A special word of thanks goes to my seniors Dr Arun Kumar, Dr Ajay Gupta and Dr Varun Sharma. I am extremely grateful for their enormous support during the early stages of my PhD.

I am thankful to the lab staff Md Yunus, Amir Hussain, Sanjay and Pradhan at the

University of Delhi who contributed directly or indirectly throughout this research work. I gratefully acknowledge the financial support received from DAE-DST and UGC during the entire period of my research work.

I am lucky enough to have been given the supportive gift of amazing people in my life, without all of whom, this work would not have been completed. I would like to thank my seniors and colleagues at our research laboratory at the University of Delhi - Dr Daljeet Kaur, Dr Shivali Malhotra, Geetika Jain, Sumit Keshri, Aashiq Shah, Aman Phogat, Asar Ahmed, Mohit Gola, Priyanka Phogat, Arjun Chettri, Prajesh Sharma, Mohd. Rafiq, Rizwan and Hemant. I cannot express how much I have learnt and enjoyed working with all of them during the last six years. Also, I would like to thank my other friends - Ankita Mehta, Anterpreet Kaur, Ridhi Chawla and Dr Archie Sharma - from India-CMS collaboration. I am happy to acknowledge Ankita Mehta for critically reviewing this thesis and putting her valuable suggestions which helped me a lot. I would also like to thank my some of the school and college friends like Sunil Pandey, Rajesh Patel, Vijay Bhatt, Ved Prakash, Dinesh Kumar Verma, Praveen Gautam, Ramesh Sharma, Nitika Mangala, Jitender, Sumit Kumar and Dheeraj Chandwani for numerous cheerful and unforgettable moments I have shared with them.

I would like to express my special thanks to Sumit Kumar for being my roommate for three years. His continuous admiration, support and trust has always helped me maintain my confidence level and given me the morale boost to overcome the hurdles of my life. You will always be the brother of my soul and the friend of my heart.

I would also like to thank my wife Archana for her immense care and helping me in thesis writing. Also, I would like to thank my brother-in-law Dr. Arvind Kumar for supporting and giving me his help during my thesis writing.

I do not have words to express my obligation and gratitude to my beloved parents, who always supported me in this journey. I very much remember with gratitude my parents, who played a big role in shaping me what I am today through their continuous counselling and suggestions. I remember the blessings and affections of all my relatives and well-wishers since my childhood with has contributed in shaping my life and career. I owe my knowledge and desire to learn more to all my respected teachers - Manju Sharma, Mani Shankar Pandey, Dr. Arijit Choudhury, Dr. Manisha Verma, Dr. Sanjeeta Gupta and Prof. Vinay Gupta - inspired me at the different stages of my life.

Last but not least, I would like to thank the most compassionate Almighty for giving me the strength, courage, ability and opportunity to undertake this research study and to accomplish it.

Date:

Place: Delhi

Ram Krishna Sharma

Abstract

In the Standard Model (SM) of particle physics, masses for the particles are generated by the Higgs mechanism which requires the existence of a spin-0 particle called the Higgs boson. In July 2012, a new Higgs-like particle, with mass ≈ 125 GeV, was discovered at the Large Hadron Collider (LHC). This might be the long-sought SM Higgs boson predicted in the 1960s, or one of the Higgs bosons predicted by the several beyond the SM scenarios. Several beyond SM scenarios, such as, super-symmetry, little-Higgs models, and others from the extended Higgs sectors such as the Georgi-Machacek model, contain a multitude of neutral as well as charged Higgs bosons. Till now the existing results contain large uncertainties, thus various extensions of the SM cannot be confirmed or ruled out decisively. This necessitates to scrutinize, the ElectroWeak Symmetry Breaking (EWSB) mechanism rigorously by carrying out the precision measurements of the Higgs boson properties and the couplings of the electroweak vector bosons (W and Z) with the Higgs boson via the Vector Boson Scattering (VBS) processes.

VBS processes violate the unitarity at an energy scale ≈ 1 TeV in the absence of the Higgs boson. Thus, it is one of the most important studies that could help us to understand the EWSB mechanism. Due to the statistical constraints, VBS could be probed indirectly by measuring the quartic vertices. This thesis is based on the study of the anomalous Quartic Gauge Coupling (aQGC) processes using the proton-proton collision data at a centre-of-mass energy of 13 TeV, collected using the Compact Muon Solenoid (CMS) detector at the CERN LHC.

The aQGC measurement is performed using two channels: WV and ZV (here, V could be either a W or a Z boson) in association with the two jets produced in the forward pseudo-rapidity regions. For the WV (ZV) channel, only leptonic decays of W (Z) bosons are considered, while the V decays hadronically into jet having large radii (having radius parameter 0.8). The events are selected by requiring two jets with

large rapidity separation and di-jet invariant mass, one or two leptons (electrons or muons), a fat jet with large radii and missing transverse momentum. Constraints are imposed on the quartic vector boson interactions in the framework of dimension-eight effective field theory operators at 95% confidence level (CL).

Furthermore, a theoretical interpretation of the observed results is given using the Georgi-Machacek model. This model predicts the existence of doubly and singly charged Higgs bosons using the Higgs triplets. The main feature of this model is that it preserves the custodial symmetry and provides neutrino with a Majorana mass. The exclusion limits on the production cross-section for the charged Higgs bosons times the branching fraction at 95% CL as a function of the mass of the charged Higgs boson are reported in this thesis.

On the hardware front, work performed for the upgrade studies of the CMS detector's muon endcap system is reported. For the CMS muon endcap detector system upgrade, the Gas Electron Multiplier (GEM) detectors are proposed to be installed during the Long Shutdown-2 (2019-2020) period. To test the functionality of these GEM detectors, several beam tests were carried out to measure their properties and evaluate their performance in terms of spatial and timing resolution, cluster size and efficiency measurements. I actively participated in these beam test campaigns and also during the data analysis for the GEM detectors. Also, the characterisation studies for the GEM foils developed in India for the CMS upgrade are also described.

Contents

1	Introduction	1
1.1	Brief Introduction of SM	3
1.1.1	Standard Model as Gauge theory	3
1.1.2	Brief Introduction to Higgs Mechanism	9
1.2	Vector Boson Scattering	12
1.3	Anomalous Quartic Gauge Coupling	14
1.4	Georgi-Machacek Model	17
1.5	Thesis Organization	20
2	The LHC and CMS Detector	23
2.1	The Large Hadron Collider	23
2.1.1	Beam Pipes	24
2.1.2	Accelerating Structure	25
2.1.3	Magnet System	26
2.2	Key requirements of a particle accelerator	28
2.3	Experiments at the LHC	32
2.4	CMS Detector	34
2.4.1	Coordinate System	37
2.4.2	CMS sub-systems	37
2.4.3	CMS Trigger and Data Acquisition system	41
2.4.4	CMS Offline Computing	48
3	Gas Electron Multiplier	51
3.1	Introduction	51
3.2	Design and working principle of GEM detector	52
3.3	GEM for the CMS Phase-II Upgrade	55

3.3.1	CMS GE1/1 Detector Specification	56
3.3.2	GE1/1 Beam Test Studies	60
3.3.3	Beam Test Experimental Set-up	66
3.3.4	Data Analysis	68
3.4	Characterization and Production of GEM Foil	81
3.4.1	Visual Inspection of Foils	83
3.4.2	Optical Test	83
3.4.3	Electrical Test	87
4	Anomalous Quartic Gauge Coupling Measurement	91
4.1	Sample Used	92
4.1.1	Data samples	92
4.1.2	Simulated Samples	93
4.2	Object Selection	96
4.2.1	Trigger	96
4.2.2	Electron selection	97
4.2.3	Muon selection	99
4.2.4	Jets	100
4.2.5	V-tag jets	100
4.2.6	B-tagging	101
4.2.7	Missing transverse energy	101
4.3	Event Selection	102
4.4	Background Estimation	103
4.4.1	Diboson	104
4.4.2	Top	104
4.4.3	W+jets	104
4.4.4	Z+jets	115
4.5	Systematic Uncertainty	115
4.5.1	Luminosity	116
4.5.2	Trigger, lepton reconstruction and identification efficiencies . .	116
4.5.3	Jet energy scale and resolution	116
4.5.4	V tagging efficiency	117
4.5.5	Pileup	117
4.5.6	MC statistics	117

4.5.7	Theoretical uncertainties	117
4.5.8	$V+jets$	118
4.5.9	Top	119
4.5.10	Summary	120
4.6	Results	121
5	Summary and Outlook	127
5.1	Future Outlook	133

List of Figures

1.1	sm triple and quartic gauge coupling.	8
1.2	Higgs potential [16]	11
1.3	VBS diagram	13
1.4	All possible VBS diagrams.	13
1.5	Other processes that fake the final state of the VBS analysis. The signal sample contains all these type of diagrams along with the VBS type diagrams as shown in Fig. 1.4	14
2.1	Other experiments at the LHC accelerating chain [30]	25
2.2	The LHC accelerator chain along with all its other experiments which use proton beam from different parts of the accelerator, either from PSB, PS or SPS [31]	27
2.3	Pair of quadrupole magnets [32].	28
2.4	Layout decribing the bunch parameters and interaction area.	30
2.5	The integrated luminosity of the LHC with proton-proton collisions in 2016 compared to previous years [41]. The recorded luminosity in 2016 far surpassed the expected luminosity and it almost doubled the luminosity recorded in 2012.	32
2.6	LHC geometry with arcs and straight sections [42].	33
2.7	Mean number of interactions per bunch crossing in p-p collision [43].	35
2.8	CMS detector drawing [44].	36
2.9	The right handed coordinate system used by CMS.	37
2.10	CMS Magnet system [45].	38
2.11	A systematic cross section view of CMS tracker showing silicon pixel and strip detectors. Double lines show back-to-back modules that deliver stereo hits.	39

2.12 A muon leaves curved trajectory in LHC and the bending changes as the magnetic field direction of solenoid inside and outside are opposite.	41
2.13 Longitudinal layout of one quadrant of the CMS detector. There are four DT stations named MB1-MB4 marked with green colour. Four CMS systems in high pseudo-rapidity region named ME1-ME4 in blue colour. Also, there are several RPC stations in barrel region and part of endcap region marked with red colour.	42
2.14 Standard Model cross sections as a function of collider energy [48]. The total hadronic cross-section is based on parametrisation of the Particle Data Group [14]. Other cross-sections are calculated at NLO or NNLO perturbative QCD, using MSTW2008 parton distributions [49].	43
2.15 CMS trigger flow diagram that uses two level trigger. At Level 1, CMS uses information from muon system and calorimeter. Using this information it decides to reject or pass the event to the HLT farm for further processing. HLT uses fast offline reconstruction algorithm that uses information from all sub-system, i.e., calorimeters, muon system as well as tracker to decide to keep or reject the event.	44
2.16 CMS Level-1 trigger flow diagram [53]. On left the hierarchy of calorimeter trigger is shown. On right the different layers of the muon trigger system is shown. Finally the global trigger combines information from both system to take the Level-1 decision.	46
2.17 The systematic representation of HLT menu and its path[55].	47
 3.1 Cross-sectional view of a GEM foil etched with holes (left). The strong electric field generated in the vicinity and inside the holes after the application of potential difference across the GEM foil (right).	53
3.2 Outline of a single GEM detector.	54
3.3 Comparison of total effective gain on anode as a function of applied voltage for single, double and triple layered GEM detectors (left). The discharge probability as a function of applied voltage is shown for the single, double and triple layered GEM detectors (right) [74].	54
3.4 The working mechanism of a GEM detector.	55
3.5 Cross-sectional view of the CMS quadrant highlighting the proposed location of GEM detectors (red).	56
3.6 The layout of different GEM layers inside a CMS GE1/1 detector.	57

3.7	Drawing of a large trapezoidal CMS GEM chamber showing $8 - \eta$ and $3 - \phi$ par partitions.	57
3.8	Layer by layer view of CMS GE1/1 detector	58
3.9	Five different generations of GE11 detector developed and improved with time.	59
3.10	Block diagram of the VFAT2 chip showing signal flow [81].	62
3.11	TURBO board [83].	63
3.12	High voltage divider configuration as used in the 2014 beam test campaign.	64
3.13	Electric field (left) and voltage across each GEM foil (right) for the tested GE1/1 detector.	64
3.14	Gain and rate variation for $Ar : CO_2$ (70:30) with respect to the current supplied to the high voltage divider for GE1/1-IV (left) and GE1/1-IV-GIF (right).	65
3.15	Gain and rate variation for $Ar : CO_2 : CF_4$ (45:15:40) with respect to the current supplied to the high voltage divider for GE1/1-IV (left) and GE1/1-IV-GIF (right).	65
3.16	Schematic view of the beam test set-up with the three tracking GEM detectors and a GE1/1 prototype.	67
3.17	Perspective view of the experimental set-up used for performance measurement in the beam test studies. The trigger system is generated using the signal collected from three scintillators connected in coincidence unit.	67
3.18	Different ($i\eta, i\phi$) sectors of a full-size GE1/1 detector prototype. The red and yellow colour shows which sector of GE1/1 is exposed to the beam. Red sectors are collected with $Ar/CO_2/CF_4$ (45/15/40) gas mixture while the yellow sectors are taken with Ar/CO_2 (70/30) gas mixture.	68
3.19	Tracker hit distribution along x and y axis and GE1/1 hit distribution along y. This is plotted from one of the runs taken during test-beam.	69

3.20 2D- beam profile plot for the first, second and third tracker. The X and Y axis of the plots correspond to the distance (in mm) measured from the central position of the trackers in X and Y direction respectively. The different colours in the colour palette correspond to the number of hits registered in the detector at a particular (x,y) position.	69
3.21 Flowchart illustrating the workflow of detector alignment algorithm.	70
3.22 Variation of track residuals for three trackers with respect to the iteration number along different directions	72
3.23 2D distributions showing events with hits registered in the trackers (top left), events registered in three trackers and GE1/1's (top right) and the division of the two histograms used to define the fiducial region for GE1/1 efficiency measurements (bottom).	73
3.24 Efficiency with respect to E_{gain} for two different gases and three different ($i\eta, i\phi$) sectors.	75
3.25 Time-resolution with respect to E_{drift} (top) and current supplied to high voltage divider (bottom) for two different gas mixture.	79
3.26 Cluster size distribution for GE1/1 detectors obtained during the beam test campaign: for run number 1644 in region $(\eta, \phi) = (5,2)$ (left), for the Run number 1869 in region $(\eta, \phi) = (8,2)$ (middle) and for Run number 2066 in region $(\eta, \phi) = (1,2)$ (right).	80
3.27 Mean value of cluster size distribution at different current supplied to high voltage divider obtained during the beam test campaign: for 2014H4A which was taken for region $(\eta, \phi) = (5,2)$ (left), for 2014H4C taken for region $(\eta, \phi) = (8,2)$ (middle) and for 2014H4D taken for region $(\eta, \phi) = (1,2)$	80
3.28 Cluster size distribution: Left - GE1/1-IV, Right - GE1/1-IV-GIF . .	81
3.29 (a) 10 cm \times 10 cm GEM foil encapsulated in a frame and (b) Cross-sectional view of the foil showing the double cone structure of the engraved holes, developed by Micropack.	82
3.30 A schematic representation of the clean room of class 100 at University of Delhi, where the characterisation of foils was performed.	83
3.31 Adhesive roller used for the cleaning of GEM foil.	84

3.32 Real gain and effective gain variation with GEM hole diameter [87] having a foil thickness of $60 \mu m$ ($= 50 \mu m + 5\mu m + 5 \mu m$). As the hole diameter decreases, the effective gain increases till $70 \mu m$ and after that it reaches saturation. This is due to loss of generated electrons in the avalanche to the bottom of the GEM electrode when hole diameter is reduced below the foil thickness.	85
3.33 Sketch of the set-up used for optical measurements of the GEM foil.	85
3.34 Observed imperfections in the GEM foils: (a) Un-etched area, (b) under-size hole, (c) over-size hole (d) missing hole, (e) excess etching and (f) burnt area.	86
3.35 Number of defects seen in (a) Insulator (Apical Type NP) and (b) Copper, for one of the $10 \text{ cm} \times 10 \text{ cm}$ foil.	86
3.36 Sketch of the set-up used for the measurement of leakage current.	88
3.37 Leakage Current for (a) Micropack Foils and (b) CERN Foils, at an average temperature of $T=27^\circ \text{ C}$ and 20% relative humidity.	88
4.1 VBS Feynman diagrams contributing to the EW induced production of events containing a hadronically decaying gauge boson (V), a W (left) or Z (right) boson decaying to leptons (electrons or muons), and two forward jets. New physics in the EW sector can modify the quartic gauge coupling.	91
4.2 Distributions of m_{WV} (left) and m_{jj} (right) in the signal region with interference contribution (red) and without interereference contribution (blue).	94
4.3 Mass distributions of the WW system for the SM EW and few aQGC parameters for the operators $S0$ (left) and $T2$ (right).	95
4.4 Distributions of m_{WV} (left) and m_{ZV} (right) in the signal region. The gray bands include uncertainties from the predicted yields. The histograms for other backgrounds include the contributions from QCD initiated dibosons, top, $W+jets$, and Drell–Yan processes. The overflow is included in the last bin. The bottom inset in each figure shows the ratio of the number of events observed in data to that of the total background prediction.	103
4.5 Kinematic distributions in the top background control region. The hatched bands include statistical uncertainties from the predicted yields.105	105

4.6	Kinematic distributions in the W+jets background sideband region. W+jets predictions are taken from the simulation. The hatched bands include statistical uncertainties from the predicted yields.	106
4.7	Kinematic distributions in the W+jets background sideband region. W+jets predictions are taken from the simulation. The hatched bands include statistical uncertainties from the predicted yields.	107
4.8	MC-data and fit shape m_{WV} distributions in the sideband region. From top to bottom: single top, $t\bar{t}$, W+jets and dibosons.	109
4.9	The data distribution and the corresponding fit of the m_{WV} distribution in the sideband region for the nominal parametric function (left) and a modified parametric function (right).	109
4.10	Alpha-ratio value (ratios of the W+jets MC contribution in the signal region to the sideband region) distribution. Red line is the fitted function used in the result.	110
4.11	Comparison of the W+jets predictions using simulation (red) and the data-driven estimation in the sideband (left) and signal regions (right). The uncertainty band shows the fit uncertainty.	111
4.12	MC fit distribution for m_V . Top Left: Single top, Top right: TTbar, Middle left: Wjets with f_{ErfExp} , Middle right: Wjets with f_{User1} , Bottom: Diboson distribution	112
4.13	Result of the normalization fit in the m_V spectrum.	114
4.14	The data and predicted m_{WV} distribution obtained from the alpha-ratio method (left) and simulation (right).	114
4.15	The data distribution and the corresponding fit of the m_{ZV} distribution in the sideband region (left) and alpha-ratio value distribution (right).	115
4.16	Nominal and up/down one standard deviation predictions for the SM EW (top) and SM QCD (bottom) background processes showing the effects of the QCD scale (left) and PDF (right) uncertainties.	118
4.17	Nominal and up/down one standard deviation predictions of the V+jets processes for the c_1 (left) and c_0 (right) fit parameters.	119
4.18	Predictions of the V+jets processes for the $f = \exp[-m/c_0]$ functions compared to the nominal prediction (left). The fit uncertainties with this functions are also shown (right).	120

4.19 Impacts and pulls of the systematic uncertainties for the Asimov dataset in the WV final state. The impacts are shown for a doubly charged Higgs with a mass of 2000GeV.	121
4.20 Yield ratios of the operator $S0$ and the fitted quadratic interpolation for the most relevant bins used in the statistical analysis. The yields for the mass bins $m_{WV} = [2025, \infty]$ (left) and $m_{WV} = [1550, 2025]$ (right) are shown.	122
4.21 Expected and observed exclusion limits at 95% confidence level as functions of $m(H^{\pm\pm})$ and $m(H^\pm)$ for $\sigma_{VBF}(H^{\pm\pm}) \mathcal{B}(H^{\pm\pm} \rightarrow WW)$ (top left) and $\sigma_{VBF}(H^\pm) \mathcal{B}(H^\pm \rightarrow WZ)$ in the WV (top right) and ZV (bottom left) final states, and on the ratio of vacuum expectation values in the GM model (bottom right). The blue shaded area covers the theoretically not allowed parameter space [152].	125
5.1 Expected and observed exclusion limits at 95% confidence level as functions of $m(H^{\pm\pm})$ and $m(H^\pm)$ for $\sigma_{VBF}(H^{\pm\pm}) \mathcal{B}(H^{\pm\pm} \rightarrow WW)$ (top left) and $\sigma_{VBF}(H^\pm) \mathcal{B}(H^\pm \rightarrow WZ)$ in the WV (top right) and ZV (bottom left) final states, and on the ratio of vacuum expectation values in the GM model (bottom right). The blue shaded area covers the theoretically not allowed parameter space [152].	132

List of Tables

1.1	Fermions list in SM [14].	4
1.2	Bosons list in SM [14].	4
1.3	Quartic vertices modified by the different operators are marked with \times	17
2.1	LHC technical parameters for proton-proton collisions: nominal, 2012 and 2016 values.[34, 35, 36, 22, 24].	29
2.2	Main characteristics of the CMS sub-system [47]	42
2.3	Examples of some of the electron and muons HLT trigger paths with their description used during data taken in 2016.	48
3.1	List of golden runs selected to measure the GE1/1 properties.	61
4.1	List of data samples used in the analysis. Here different run names corresponds to the different time stamp during which data was collected, and the date in the data sample name corresponds to the time stamp at which it was converted to the physics objects, i.e, electrons, muons, jets, etc from the hit and energy deposit information.	93
4.2	aQGC signal sample names and cross sections of simulated samples used in the analysis	94
4.3	SM EWK signal sample names and cross sections of simulated samples used in the analysis	94
4.4	Background sample names and cross sections of simulated samples used in the analysis. The naming	96
4.5	Summary of object selection.	96
4.6	The cut based electron identification working points for $ \eta$ supercluster $<=$ 1.479	98

4.7	The cut based electron identification working points for $ \eta_{\text{supercluster}} > 1.479$	99
4.8	PF-loose Jet ID requirements based on the content of jets.	101
4.9	Expected yields from various background processes in WV and ZV final states. The statistical and systematic uncertainties are shown. The aQGC and charged higgs signal yields are also shown.	104
4.10	Extracted fit parameters for the functions describing the m_{WV} distributions.	110
4.11	Extracted fit parameters for the functions describing the m_V distributions.	113
4.12	Relative systematic uncertainties in the estimated signal and background yields in units of percent.	120
4.13	Observed and expected 95% C.L. limits on the coefficients for higher-order (dimension-8) operators in the effective field theory Lagrangian in WV final state.	123
4.14	Observed and expected 95% C.L. limits on the coefficients for higher-order (dimension-8) operators in the effective field theory Lagrangian in ZV final state.	123
4.15	Observed and expected 95% C.L. combined limits on the coefficients for higher-order (dimension-8) operators in the effective field theory Lagrangian in WV and ZV final states.	124
5.1	Quartic vertices modified by the different operators are marked with \times . In the first row W, Z and A refer to the W-boson, Z-boson and photon respectively. In the first column, the bold parameters are measured and the limits are reported.	129
5.2	Observed and expected 95% CL limits on the coefficients for higher-order (dimension-8) operators in the effective field theory Lagrangian in WV final state.	130
5.3	Observed and expected 95% CL limits on the coefficients for higher-order (dimension-8) operators in the effective field theory Lagrangian in ZV final state.	131
5.4	Observed and expected 95% CL combined limits on the coefficients for higher-order (dimension-8) operators in the effective field theory Lagrangian in WV and ZV final states.	131

1

Introduction

“Particle physics is a modern name for the centuries old effort to understand the basic laws of physics.”

– Edward Witten

Ever since the existence, mankind is striving to unravel mysteries of nature around us. Several theoretical frameworks have been developed to answer key questions regarding our existence in this Universe. Continuous endeavours of the thinkers and scientists in this regard lead to the evolution of a branch of physics, namely “*particle physics*”, dealing with the study of fundamental particles and the interactions amongst them.

Standard Model (SM) of particle physics is a theoretical framework, developed in the 1960s and 70s, which encapsulates nearly all that is known about the elementary particles and forces in a concise set of principles and equations. SM has been very successful in predicting the behaviour and certain characteristics of the elementary particles. It gives a compelling explanation of the existing experimental data. During 1960’s, while trying to unify the theories of electromagnetic and weak interactions it was realized that gauge bosons mediating these interactions should be massless which was in contradiction with the experimental evidences [1, 2, 3]. This dilemma was resolved by P.W. Higgs, F. Englert, R. Brout and others, by postulating that the electroweak gauge symmetry is spontaneously broken [4, 5, 6, 7, 8, 9], which gives mass to the elementary particles and the force carriers but it requires a new scalar (spin-zero) particle, namely the Higgs boson. This new scalar boson not only provides mass to the elementary particles but it solves other problems such as: it preserves the

unitarity of the Vector-Boson Scattering (VBS). It was the only missing link from SM till 2012. In 2012, it was observed at the CERN Large Hadron Collider (LHC) [10, 11], and its properties were measured in the following years. This completes the picture of the elementary particles predicted by the SM. However, the SM still leaves some unexplained phenomena, such as:

- reason behind spontaneous symmetry breaking?
- Is the Higgs boson only source for preserving the unitization in vector-boson scattering?
- reason behind the baryon asymmetry in universe? and many more.

After the discovery of Higgs Boson, the major goal of the physics programme at the LHC is to provide a definitive answer to these open questions by significantly expanding both the energy reach and the collision rate with respect to the previous experiments and its own Run periods. Ongoing measurements at the LHC also include the precision measurements in the electroweak sectors and to look for VBS which could also hint towards the existence of new physics phenomenon, indirectly [12]. These measurements could provide information on the structure of $SU(2) \times U(1)$ -breaking physics and its experimental signatures. The scattering of the vector bosons is strongly connected to the electroweak symmetry breaking (EWSB) in the SM, regulated by the Brout-Englert-Higgs mechanism. This study will help one to clearly understand the role of the observed Higgs boson in the EWSB. Because Recent discovery of the Higgs boson indicates that the ultimate EWSB should be similar to the existing Higgs mechanism which needs to be scrutinized.

VBS processes can also provides information on the quartic vector boson interactions, a part of the SM which has not been tested yet and could be modified by the existence of new physics. Given the large amount of high-luminosity data available at the LHC, it is possible to probe this rare physics process using different final states. Thus, the VBS emerges as a strong candidate process to serve the two-fold purpose to perform the precision measurements and side-by-side look for the new physics phenomenon. In this chapter, a brief introduction of the SM along with the EWSB is given. Also, the anomalous quartic gauge coupling and VBS are discussed briefly along with the doubly charged Higgs model in the framework of model created by the Georgi and Machacek.

1.1 Brief Introduction of SM

SM is the theory of elementary particles and their interactions. It is well tested and in good agreement with experimental results, obtained so far.

Till now we know of four fundamental interactions. Out of the four, the gravitational interaction is not included in SM. The other three forces - the strong force interaction as described by Quantum Chromodynamics (QCD), the electromagnetic interaction as described by Quantum Electrodynamics (QED) and the weak interaction - are included in the SM. In 1979, Sheldon Glashow, Abdus Salam, and Steven Weinberg were awarded Nobel prize for their effort to unify the theory of weak interaction and the quantum electrodynamics [1, 2]. This unified theory of weak interaction and quantum electrodynamics is known as the electroweak theory.

According to SM all the fundamental particles can be classified into two categories. They are fermions and bosons.

Fermions are the particles that obey the Fermi-Dirac statistics with half-integer spin. In SM, fermions are further classified into leptons and quarks, which are listed in Table 1.1. The quarks and leptons create the subatomic scaffolding for solid matter. Quarks bind together to form protons and neutrons and the electrons orbit these cluster of quarks to form atoms and the atoms combine into all the known stable matter of universe [13]. Till now we know the three generations of leptons as well as quarks. The different generations are differing only in the particle mass.

Bosons are the particles that obey the Bose-Einstein statistics with integer spin. In SM the bosons are the mediator of interactions between the particles, described by a local gauge theory. Thus, these bosons are called gauge bosons. All the bosons in SM are listed in Table 1.2. The photon and gluons are massless carrying electromagnetic and strong force respectively. The W^\pm and Z bosons carry the weak force. These bosons are the spin 1 bosons and known as the vector-bosons. Whereas, the Higgs boson, H , is a scalar boson with spin 0. This is responsible for the mass generation (by giving longitudinal polarization) to the fundamental particles through EWSB, which is explained in section 1.1.2.

1.1.1 Standard Model as Gauge theory

Gauge invariance is the key ingredient in the construction of the SM of electromagnetic, weak and strong interactions of elementary particles. In general gauge principle

Generation	Fermion	Electric Charge	Weak isospin I_3	Mass in MeV
		left-handed	right-handed	
1^{st}	electron (e^-)	-1	1/2	$0.511 \pm 3.1 \times 10^{-8}$
	electron-neutrino (ν_e)	0	1/2	$< 2 \times 10^{-6}$
	up quark (u)	2/3	1/2	$2.2^{+0.5}_{-0.4}$
	down quark (d)	-1/3	1/2	$4.7^{+0.5}_{-0.3}$
2^{nd}	muon (μ^-)	-1	1/2	$105.658 \pm 2.4 \times 10^{-6}$
	muon-neutrino (ν_μ)	0	1/2	$< 2 \times 10^{-6}$
	charm quark (c)	2/3	1/2	1275^{+25}_{-35}
	strange quark (s)	-1/3	1/2	95^{+9}_{-3}
3^{rd}	tau (τ^-)	-1	1/2	1776.86 ± 0.12
	tau-neutrino (τ_μ)	0	1/2	$< 2 \times 10^{-6}$
	top quark (t)	2/3	1/2	$1.73 \times 10^5 \pm 40$
	bottom quark (b)	-1/3	1/2	$4.18 \times 10^{3+40}_{-30}$

Table 1.1: Fermions list in SM [14].

	Bosons	Electric Charge	Spin	Interaction	Mass in GeV
γ	photon	0	1	electromagnetic	$< 1 \times 10^{-27}$
W^\pm	W bosons	± 1	1	weak	80.379 ± 0.012
Z^0	Z boson	0	1	weak	91.188 ± 0.0023
g	gluons	0	1	strong	0
H	Higgs	0	0		125.18 ± 0.16

Table 1.2: Bosons list in SM [14].

specifies that for a given gauge symmetry group and the transformation of the fields, the quantum field theory can be uniquely defined [15].

The construction of QED is an example of local gauge theory as the Lagrangian function (Eq. 1.1) that describes the QED of the spin-half particle remains invariant by the local gauge transformation of the electron field $\psi(x)$ and the photon field $A_{\mu}(x)$ at all space-time point x.

$$\mathcal{L} = i\bar{\psi}\gamma^{\mu}D_{\mu}\psi - m\bar{\psi}\psi, \quad (1.1)$$

The transformation followed by the electron field and photon field is:

$$\begin{aligned} \psi(x) &\rightarrow e^{iq\chi(x)}\psi(x), \\ A_{\mu}(x) &\rightarrow A_{\mu}(x) - \partial_{\mu}\chi(x), \end{aligned} \quad (1.2)$$

Where the $\chi(x)$ is the arbitrary phase transformation, q is the electron-photon coupling. And the D_{μ} given in the eq. 1.1 is known as covariant derivative and is given as:

$$D_{\mu} = \partial_{\mu} + iqA_{\mu}, \quad (1.3)$$

Here, the photon field plays an intrinsic role without which there could be no local gauge invariance. In the construction of the local gauge invariance of QED, we realize that the local gauge invariance of a spin-half particle requires the existence of a gauge boson and their coupling with the fermions. Also, for the exact gauge invariance, the gauge bosons must be massless.

In Eq. 1.2, the phase factor $e^{iq\chi(x)}$ belongs to the symmetry group $U(1)$ of the unitarity transformations in one dimension. Thus, the generalization of the QED can be made to the other forces by exploring other possibilities of the symmetry group.

For example, the electrons and neutrino can be chosen as a double (ν_e, e) , i.e. as two members of the same family, since both of them are spin-half particles. Thus, it can be described as the doublet by a two-component field $\phi = (\nu_e(x), e(x))$ and imposes a gauge transformation where α is a 2×2 hermitian matrix operating on the ϕ .

The weak interaction, $SU(2)$, local gauge transformation can be written for the electron doublet field as

$$\phi(x) = e^{ig_w\alpha(\mathbf{x})\cdot\mathbf{T}}\phi(x)$$

$$\simeq (I + ig_w \boldsymbol{\alpha}(\mathbf{x}) \cdot \mathbf{T}) \phi(x), \quad (1.4)$$

where $\boldsymbol{\alpha}(\mathbf{x})$ is the arbitrary infinitesimal vector in the isospin space and the $\mathbf{T} = \{T_1, T_2, T_3\}$ is the three generators of the SU(2) symmetry group, which can be expressed using Pauli spin matrices as $\mathbf{T} = \boldsymbol{\sigma}/2$. Also, the T_i do not commute,

$$[T_i, T_j] = i\epsilon_{ijk}T_k, \quad (1.5)$$

and the doublet field $\phi(x)$ is given as:

$$\phi(x) = \begin{bmatrix} \nu_e(x) \\ e(x) \end{bmatrix}. \quad (1.6)$$

As the generator of this group, T_i 's do not commute it is said to be the non-Abelian group.

Assuming the fermion mass to be zero the Lagrangian for the electron and electron-neutrino can be written as

$$\mathcal{L} = i\bar{\phi}\gamma_\mu\partial^\mu\phi = i\bar{\nu}_e\gamma_\mu\partial^\mu\nu_e + i\bar{e}\gamma_\mu\partial^\mu e \quad (1.7)$$

The ψ -field in the Lagrangian, Eq. 1.7 can be made gauge invariant by using the covariant derivative instead of derivative, which is defined using the three gauge fields given by $\mathbf{W} = \{W_1, W_2, W_3\}$ as

$$\partial_\mu \rightarrow D_\mu = \partial_\mu + ig_w \mathbf{W}_\mu \cdot \mathbf{T} \quad (1.8)$$

Also the gauge fields $\mathbf{W}_{i\mu}$ transforms as

$$\mathbf{W}_\mu(x) \rightarrow \mathbf{W}_\mu(x) + \partial_\mu \boldsymbol{\alpha}(\mathbf{x}) + g\boldsymbol{\alpha}(\mathbf{x}) \times \mathbf{W}_\mu(x) \quad (1.9)$$

Unlike the QED (Eq. 1.2), the gauge field transformation in weak interaction (or SU(3) group) is complicated because of the non-Abelian property of its generator. Using Eq. 1.7, 1.9, and 1.8, we can show that the Lagrangian of weak interaction, Eq. 1.7, remains gauge invariant.

Still, we need to add the kinetic term for the W fields. This can be taken similar

to the QED and given by

$$\mathcal{L}_W = -\frac{1}{4} \mathbf{W}_{\mu\nu} \cdot \mathbf{W}^{\mu\nu} \quad (1.10)$$

where,

$$\mathbf{W}_{\mu\nu} = \partial_\mu \mathbf{W}_\nu - \partial_\nu \mathbf{W}_\mu - g \mathbf{W}_\mu \times \mathbf{W}_\nu \quad (1.11)$$

Here, the term $\mathbf{W}_\mu \times \mathbf{W}_\nu$ shows that the Lagrangian of weak interaction contains the W-boson self-interaction terms and written as

$$\mathbf{W}^\mu \times \mathbf{W}^\nu = \epsilon_{ijk} W_j^\mu W_k^\nu \quad (1.12)$$

Now, using Eq. 1.11, Eq. 1.10 becomes

$$\begin{aligned} \mathcal{L} &= -\frac{1}{4} \left[(\partial_\mu \mathbf{W}_\nu - \partial_\nu \mathbf{W}_\mu) - g_w \mathbf{W}_\mu \times \mathbf{W}_\nu \right] \left[(\partial^\mu \mathbf{W}^\nu - \partial^\nu \mathbf{W}^\mu) - g_w \mathbf{W}^\mu \times \mathbf{W}^\nu \right] \\ &= -\frac{1}{4} (\partial_\mu \mathbf{W}_\nu - \partial_\nu \mathbf{W}_\mu) (\partial^\mu \mathbf{W}^\nu - \partial^\nu \mathbf{W}^\mu) \\ &\quad + \frac{1}{4} \left[g_w (\partial_\mu \mathbf{W}_\nu - \partial_\nu \mathbf{W}_\mu) \mathbf{W}^\mu \times \mathbf{W}^\nu \right] + \frac{1}{4} \left[g_w \mathbf{W}_\mu \times \mathbf{W}_\nu (\partial^\mu \mathbf{W}^\nu - \partial^\nu \mathbf{W}^\mu) \right] \\ &\quad - \frac{1}{4} g_W^2 (\mathbf{W}_\mu \times \mathbf{W}_\nu) (\mathbf{W}^\mu \times \mathbf{W}^\nu) \end{aligned} \quad (1.13)$$

Now, we can explicitly divide the weak interaction Lagrangian into the kinetic and interaction parts, as

$$\mathcal{L}_W = \mathcal{L}_{kin} + \mathcal{L}_{int}, \quad (1.14)$$

where,

$$\mathcal{L}_{kin} = -\frac{1}{4} (\partial_\mu \mathbf{W}_\nu - \partial_\nu \mathbf{W}_\mu) (\partial^\mu \mathbf{W}^\nu - \partial^\nu \mathbf{W}^\mu)$$

and,

$$\begin{aligned} \mathcal{L}_{int} &= \frac{1}{4} \left[g_w (\partial_\mu \mathbf{W}_\nu - \partial_\nu \mathbf{W}_\mu) \mathbf{W}^\mu \times \mathbf{W}^\nu \right] + \frac{1}{4} \left[g_w \mathbf{W}_\mu \times \mathbf{W}_\nu (\partial^\mu \mathbf{W}^\nu - \partial^\nu \mathbf{W}^\mu) \right] \\ &\quad - \frac{1}{4} g_W^2 (\mathbf{W}_\mu \times \mathbf{W}_\nu) (\mathbf{W}^\mu \times \mathbf{W}^\nu) \end{aligned} \quad (1.15)$$

In component form it can be written as:

$$\begin{aligned} \mathcal{L}_{int} &= \frac{1}{2} \left[g_w \epsilon_{ijk} (\partial_\mu W_{\nu i} - \partial_\nu W_{\mu i}) W_j^\mu \times W_k^\nu \right] \\ &\quad - \frac{1}{4} g_W^2 \epsilon_{ijk} \epsilon_{imn} W_j^\mu W_k^\nu W_{m\mu} W_{n\nu} \end{aligned} \quad (1.16)$$

Here, the interaction part of Lagrangian shows that in weak interaction there are triple as well as quartic both types of self-couplings are allowed, as shown in Fig. 1.1. In weak interaction, these self-couplings are the consequences of the non-Abelian nature of the $SU(2)$ group algebra. In terms of the physical fields, there are two types of triple gauge couplings - $\gamma W^+ W^-$ and $Z W^+ W^-$ - and three types of quartic gauge couplings, $W^+ W^- W^+ W^-$, $W^+ W^- ZZ$, and $W^+ W^- \gamma\gamma$, which are allowed in the SM.

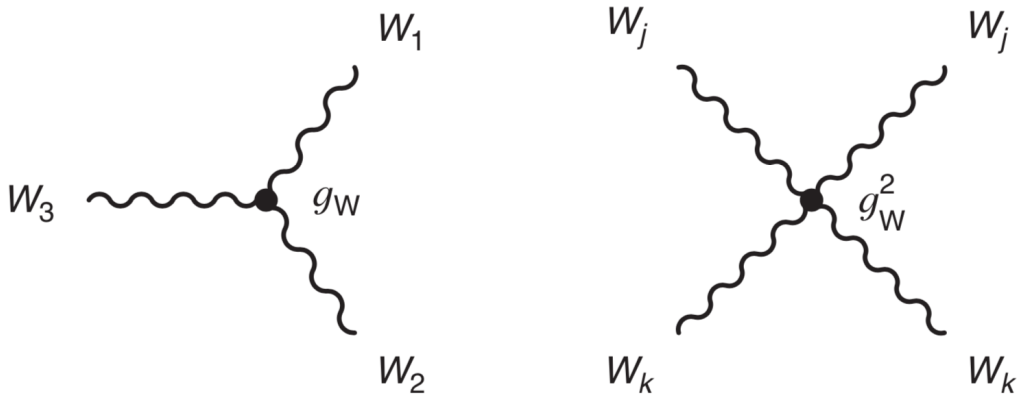


Figure 1.1: sm triple and quartic gauge coupling.

Similarly, the other leptons and the quarks can also be put in doublets (ν_μ, μ) , (ν_τ, τ) , (u, d) , etc. and subject to the similar transformations. Furthermore, these transformations are not only the phase factors, as the off-diagonal elements of χ can change one member of a doublet into the another as it belongs to the same symmetry group $SU(2)$ of the unitary unimodular transformations in 2-dimensions. And the local gauge invariance in these cases requires the introduction of three massless spin-1 gauge bosons W^+ , W^- and W^0 . Furthermore, if it can be combined with a simultaneous $U(1)$ symmetry it brings one more gauge boson B^0 . This group is known as the $SU(2)_L \times U(1)$ gauge group, which is formulated successfully by Glashow, Salam, and Weinberg for the unification of QED and weak interaction (known as electroweak interactions) [2] having massless gauge bosons. But all the gauge bosons cannot be massless. The masses of gauge bosons W^+ , W^- and Z bosons has already been measured by experiments. Thus the symmetry cannot be exact. It should be broken spontaneously in such a way that it retains the renormalizable feature in such a way that it retain three massive bosons W^+ , W^- and Z and one massless boson γ . This

is explained in Sec. 1.1.2.

The subscript in the $SU(2)_L$ in the electroweak theory tells that the gauge transformation $SU(2)$ only acts on the left-handed particles. This condition is imposed since the process like the beta-decay are observed to involve the quark and leptons with left-handed spins relative to their motions. The first generation of the spin-half particles can be classified in doublet and singlets representations of $SU(2)_L$ as below:

$$(u_L, d_L), (\nu_{eL}, e_L), \bar{u}_L, \bar{d}_L, \bar{e}_L, \\ (\bar{d}_R, \bar{u}_R), (\bar{e}_R, \bar{\nu}_{eR}), u_R, d_R, e_R.$$

Furthermore, we did not find the right-handed neutrino state experimentally yet. Thus we have 15 left-handed (and 15 right-handed) fermion states in each generation counting three colours for each quark flavour, in this gauge theory of electroweak interactions.

The strong interaction is described by $SU(3)$ local gauge invariance. It is described by the three-component field $\psi(x) = [\psi(\text{red}, x), \psi(\text{blue}, x), \psi(\text{green}, x)]$ having local gauge transformation χ which is a 3×3 hermitian matrix operating on ψ , as each quark has three possible colours. To achieve the local gauge invariance this requires the introduction of eight massless gauge boson, known as gluons, which carry pairs of color labels. This gauge theory of strong interaction is known as QCD. This gauge theory combined with electroweak theory gives $SU(3) \times SU(2) \times U(1)$ gauge invariant theory of strong and electroweak forces combined, becomes the Standard Model.

1.1.2 Brief Introduction to Higgs Mechanism

One of the main issues with the electroweak theory was that all the particles were assumed to be massless. The mass term was not invariant under the local gauge transformation under $SU(2)_L \times U(1)_Y$ and therefore, breaks symmetry. This issue was solved by the Higgs mechanism. The Higgs mechanism predicts a symmetrical Higgs field having non-invariant lowest energy state. This gives mass to the fermions and boson by interacting with the Higgs field. The Higgs field can only be observed via its excitation known as the Higgs boson, H .

The electroweak theory contains $SU(2)_L \times U(1)_Y$ symmetry and the Higgs part of

full Lagrangian is given by :

$$L_H = (D_\mu \Phi)^\dagger (D^\mu \Phi) - V(\Phi) \quad (1.17)$$

The SM Lagrangian extends the experimentally well established particle content of the SM by the complex scalar SU(2) doublet $\Phi = (\phi^+, \phi^0)^T$ of weak hypercharge $Y_{w,\Phi} = 1$, so that ϕ^+ carries charge +e and ϕ^0 is neutral. In total Φ involves four degree of freedom. The self-interaction of Φ is described by the potential

$$V(\Phi) = -\mu^2(\Phi^\dagger \Phi) + \frac{\lambda}{4}(\Phi^\dagger \Phi)^2, \quad (1.18)$$

Here, the term $\lambda > 0$ ensures that the potential is bounded from below. Here we need to generate masses for the three gauge bosons W^\pm and Z but the photon should remain massless. Therefore, we need at least 3 degree of freedom for the scalar fields. The simplest choice is a complex SU(2) doublet of scalar field ϕ :

$$\Phi = \begin{bmatrix} \phi^+ \\ \phi^0 \end{bmatrix} = \frac{1}{\sqrt{2}} \begin{bmatrix} \phi_1 + i\phi_2 \\ \phi_3 + i\phi_4 \end{bmatrix} \quad (1.19)$$

where ϕ_i are 4 real scalar fields (4 degree of freedom). The Lagrangian is invariant under the local gauge transformations ¹

$$\Phi(x) \rightarrow \Phi(x)' = e^{i\alpha_i(x)\tau_i/2} \Phi(x) \quad (1.20)$$

where τ_i are Pauli matrices and $\alpha_i(x)$ are transformation parameters. Now the product

$$\Phi^\dagger \Phi = \begin{bmatrix} \phi^{+*} & \phi^{0*} \end{bmatrix} \begin{bmatrix} \phi^+ \\ \phi^0 \end{bmatrix} = \phi^{+*}\phi^+ + \phi^{0*}\phi^0 = \frac{1}{2}(\phi_1^2 + \phi_2^2 + \phi_3^2 + \phi_4^2) = \frac{1}{2}\phi_i\phi^i \quad (1.21)$$

For $\mu^2 < 0$, corresponds to the “Mexican Hat” potential shown in Fig. 1.2, the

¹The concept of gauge invariance is fundamental in the construction of the Standard Model of strong, weak and electromagnetic interactions of elementary particles. The gauge principle prescribes that, given the gauge symmetry group and the transformations of the fields, the quantum field theory is uniquely defined [15].

potential $V(\Phi)$ has a minimum at

$$\Phi^\dagger \Phi = -\frac{\mu^2}{2\lambda} = \frac{v^2}{2} \quad (1.22)$$

From equation 1.21, we know that there is an infinite number of possible solutions of this equation. To preserve electric charge conservation ($U(1)_{QED}$ symmetry), this non zero vacuum expectation value should not be reached in the charged direction. A convenient choice of the neutral direction is $\phi_1 = \phi_2 = \phi_4 = 0$. So, the equation 1.19:

$$\Phi = \frac{1}{\sqrt{2}} \begin{bmatrix} 0 \\ \phi_3 \end{bmatrix} \quad (1.23)$$

Therefore, the neutral component (ϕ_3) of the doublet field Φ develops a nonzero

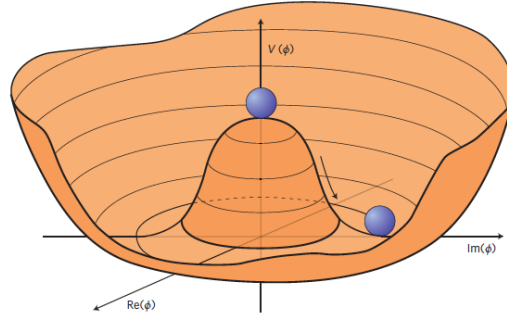


Figure 1.2: Higgs potential [16]

vacuum expectation value

$$\langle \Phi \rangle_0 = \langle 0 | \Phi | 0 \rangle = \frac{1}{\sqrt{2}} \begin{bmatrix} 0 \\ v \end{bmatrix} \text{ with } v = -\left[\frac{\mu^2}{\lambda}\right]^{1/2} \quad (1.24)$$

Now by using the unitarity gauge² means of proper gauge transformation of the field we get

$$\Phi(x) = \frac{1}{\sqrt{2}} \begin{bmatrix} 0 \\ v + h(x) \end{bmatrix} \quad (1.25)$$

With $\Phi(x)$ we can expand kinetic term $D_\mu \Phi^\dagger (D_\mu \Phi) = |D_\mu \Phi|^2$ of lagrangian

$$|D_\mu \Phi|^2 = |(\partial_\mu - ig_2 \frac{\tau_a}{2} W_\mu^a - ig_1 \frac{Y_H}{2} B_\mu) \Phi|^2$$

²It removes the unphysical degree of freedom

$$= \frac{1}{2}(\partial_\mu H)^2 + \frac{1}{8}g_2^2(v+H)^2|W_\mu^1 + iW_\mu^2|^2 + \frac{1}{8}|g_2 W_\mu^3 - g_1 B_\mu|^2 \quad (1.26)$$

Lets define the new fields W_μ^\pm and Z_μ [A_μ is the field orthogonal to Z_μ]:

$$W^\pm = \frac{1}{\sqrt{2}}(W_\mu^1 \mp iW_\mu^2), \quad Z_\mu = \frac{g_2 W_\mu^3 - g_1 B_\mu}{\sqrt{g_2^2 + g_1^2}}, \quad A_\mu = \frac{g_2 W_\mu^3 + g_1 B_\mu}{\sqrt{g_2^2 + g_1^2}} \quad (1.27)$$

Now we pick the term from equation 1.26 which are bilinear in the fields W^\pm, Z, A :

$$M_w^2 W_\mu^+ W^{-\mu}, \quad \frac{1}{2} M_z^2 Z_\mu Z^\mu, \quad \text{and} \quad \frac{1}{2} M_A^2 A_\mu A^\mu \quad (1.28)$$

Then we noted that W and Z boson have acquired masses, while the photon is still massless

$$M_w = \frac{1}{2}vg_2, \quad M_z = \frac{1}{2}v\sqrt{g_2^2 + g_1^2}, \quad M_A = 0 \quad (1.29)$$

So, by spontaneously breaking the symmetry, three Goldstone bosons have been absorbed by the W^\pm and Z boson to form their longitudinal components and to get their masses. Since the U(1) symmetry is still unbroken, the photon which is its generator, remains massless.

Thus, it is established that the Higgs mechanism generates the mass for the vector boson, So, it follows naturally.

1.2 Vector Boson Scattering

As discussed in the previous section, the VBS is one of the important measurements to be performed at the LHC. It is known that the VBS includes both triple and quartic gauge coupling. In VBS, the radiated gauge bosons by quarks from the two protons and interact with each other and decay afterwards. The Feynman diagram corresponding to the VBS is shown in fig. 1.3.

There are several different ways by which the gauge bosons can interact via a quartic vertices or exchange of Z or γ or W or a Higgs boson. This is shown using the Feynman diagram in Fig. 1.4

Vector Boson Scattering requires six weak vertices, so it is a $\mathcal{O}(\alpha_W^6)$ process with a small cross section compared to most of the processes observed at the LHC. Another difficulty is that we could not generate only $\mathcal{O}(\alpha_W^6)$ process for VBS alone from any

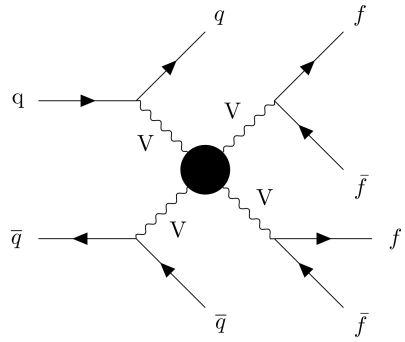


Figure 1.3: VBS diagram

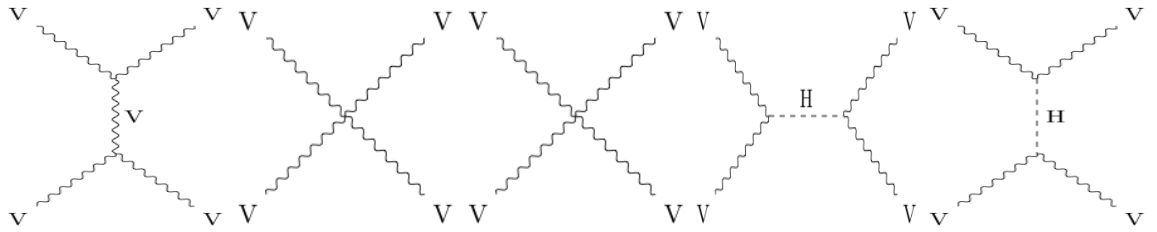


Figure 1.4: All possible VBS diagrams.

available generator in a gauge invariant way. Along with the VBS diagrams it contains lots of other Feynman diagrams, as shown in Fig. 1.5.

One of the important signatures of VBS are the two jets in the forward pseudo-rapidity region, called as tagging jets, resulting from the quark emitting the gauge bosons. Thus, the pseudo-rapidity between the tagging jets is expected to be large.

Furthermore, there are different modes of decay of w-bosons like $WW \rightarrow l\nu l\nu$, $WW \rightarrow jjjj$, and $WW \rightarrow l\nu jj$. The leptonic channel is considered to have less background specially if working with same sign W-bosons but it has very less cross-section than semi-leptonic or fully hadronic. While the fully hadronic channel has comparatively larger cross-section but it suffers from huge QCD background. Thus, one of best ways to work with semi-leptonic channel is that it has larger branching fraction than fully leptonic and comparatively lesser background than fully-hadronic, for which the analysis was performed and the details are given in Section ??.

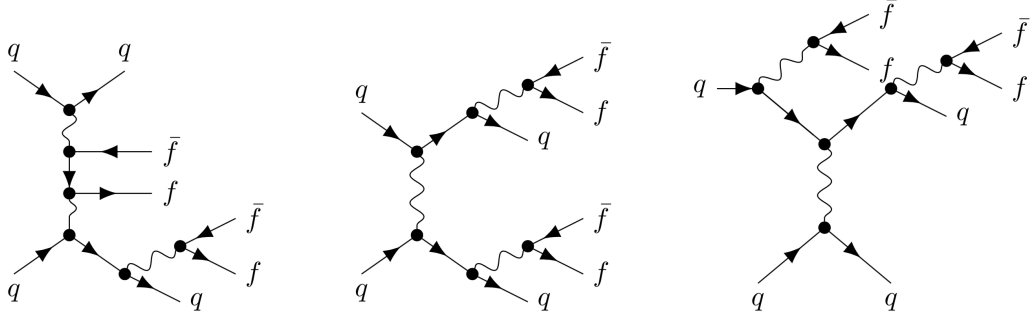


Figure 1.5: Other processes that fake the final state of the VBS analysis. The signal sample contains all these type of diagrams along with the VBS type diagrams as shown in Fig. 1.4

1.3 Anomalous Quartic Gauge Coupling

The SM has been found to be in good agreement with experimental results but it is quite possible that the SM is correct only up to an unknown centre of mass energy scale Λ . Thus, it is possible that the new effect or completely new physics lie above this scale but the sign of it can be observed indirectly at the currently accessible energy. One of the possible ways to detect these signs is to build an Effective Field Theory (EFT) to parametrize the effects of high energy scale effect on the energy scale available to us. This introduces new degree of freedom to the SM.

The new effective Lagrangian using the EFT is

$$\mathcal{L}_{eff} = \mathcal{L}_{SM} + \sum_{i=www,w,B,\phi W,\phi B} \frac{c_i}{\Lambda^2} \mathcal{O}_i + \sum_{j=0,1} \frac{f_{S,j}}{\Lambda^4} \mathcal{O}_{S,j} + \sum_{j=0,...,9} \frac{f_{T,j}}{\Lambda^4} \mathcal{O}_{T,j} + \sum_{j=0,...,7} \frac{f_{M,j}}{\Lambda^4} \mathcal{O}_{M,j}, \quad (1.30)$$

here, Λ is the new physics scale, the parameter c_i , is the dimensionless coupling-strength coefficient of order $\mathcal{O}(1)$ and $f_{S,j}$, $f_{T,j}$ and $f_{M,j}$ are for the dimensionless coupling-strength coefficient for the quartic gauge couplings. Also, in EFT at $\Lambda \rightarrow \infty$ the effective Lagrangian should reduce to the SM one.

Due to higher dimension these operators \mathcal{O} have coefficients of inverse power of mass so the operators with the lowest dimension are dominant. Most of the SM operators are of dimension four and since only operators with even dimension satisfy conservation of lepton and baryon number the new operators have to be at least

dimension six operators [17]. These new operators effect also double and triple gauge boson couplings; these can be studied more easily in other processes. .

Dimension eight operators have no effects in double or triple couplings so they have to be searched for in quartic gauge couplings. Vector Boson Scattering allows these examinations of these couplings. In general the following are the possible operators for the quartic gauge boson vertex:

Operators containing only $D_\mu\phi$

In this category there are two independent operators. They are:

$$\mathcal{O}_{S,0} = \left[(D_\mu\phi)^\dagger \times D_\nu\phi \right] \times \left[(D^\mu\phi)^\dagger D^\nu\phi \right], \quad (1.31)$$

$$\mathcal{O}_{S,1} = \left[(D_\mu\phi)^\dagger \times D^\mu\phi \right] \times \left[(D_\nu\phi)^\dagger D^\nu\phi \right], \quad (1.32)$$

where the Higgs covariant derivative is given as

$$D_\mu = \partial_\mu + i\frac{g'}{2}B_\mu + ig_w W_\mu^i \frac{T^i}{2} \quad (1.33)$$

and the field strength tensors of the $SU(2)_L$ (W_μ^i) and $U(1)_Y$ (B_μ) gauge fields are given as

$$W_{\mu\nu} = \frac{i}{2}gT^i(\partial_\mu W_\nu^i - \partial_\nu W_\mu^i + g\epsilon_{ijk}W_\mu^j W_\nu^k) \quad (1.34)$$

$$B_{\mu\nu} = \frac{i}{2}g'(\partial B_\nu - \partial_\nu B_\mu) \quad (1.35)$$

The operators $\mathcal{O}_{S,0}$ and $\mathcal{O}_{S,1}$ contains the quartic gauge coupling for process $\mathbf{W}^+\mathbf{W}^-\mathbf{W}^+\mathbf{W}^-$, $\mathbf{W}^+\mathbf{W}^-ZZ$ and $ZZZZ$ interactions which do not depend on the gauge boson momenta.

Operators containing $D_\mu\phi$ and two field strength tensors

The quartic gauge coupling is also generated by using the two electroweak field strength tensors and two covariant derivatives of the Higgs doublet as:

$$\mathcal{O}_{M,0} = Tr \left[W_{\mu\nu} W^{\mu\nu} \right] \times \left[(D_\beta\phi)^\dagger D^\beta\phi \right] \quad (1.36)$$

$$\mathcal{O}_{M,1} = Tr \left[W_{\mu\nu} W^{\nu\beta} \right] \times \left[(D_\beta\phi)^\dagger D^\mu\phi \right] \quad (1.37)$$

$$\mathcal{O}_{M,2} = \left[B_{\mu\nu} B^{\mu\nu} \right] \times \left[(D_\beta \phi)^\dagger D^\beta \phi \right] \quad (1.38)$$

$$\mathcal{O}_{M,3} = \left[B_{\mu\nu} B^{\nu\beta} \right] \times \left[(D_\beta \phi)^\dagger D^\mu \phi \right] \quad (1.39)$$

$$\mathcal{O}_{M,4} = \left[(D_\mu \phi)^\dagger W_{\beta\nu} D^\mu \phi \right] \times B^{\beta\nu} \quad (1.40)$$

$$\mathcal{O}_{M,5} = \left[(D_\mu \phi)^\dagger W_{\beta\nu} D^\nu \phi \right] \times B^{\beta\mu} \quad (1.41)$$

$$\mathcal{O}_{M,6} = \left[(D_\mu \phi)^\dagger W_{\beta\nu} W^{\beta\nu} D^\mu \phi \right] \quad (1.42)$$

$$\mathcal{O}_{M,7} = \left[(D_\mu \phi)^\dagger W_{\beta\nu} W^{\beta\nu} D^\mu \phi \right] \quad (1.43)$$

Here, the field strength tensors $W_{\mu\nu}$ and $B_{\mu\nu}$ is defined as Eq. 1.34. This class of operators of the quartic gauge-boson interaction depends on the vector boson momenta due to the presence of the field strength tensors.

Operators containing only field strength tensors

In this class only the field strength tensors lead to the anomalous quartic couplings, which is given by following operators:

$$\mathcal{O}_{T,0} = Tr \left[W_{\mu\nu} W^{\mu\nu} \right] \times Tr \left[W_{\alpha\beta} W^{\alpha\beta} \right] \quad (1.44)$$

$$\mathcal{O}_{T,1} = Tr \left[W_{\alpha\nu} W^{\mu\beta} \right] \times Tr \left[W_{\mu\beta} W^{\alpha\nu} \right] \quad (1.45)$$

$$\mathcal{O}_{T,2} = Tr \left[W_{\alpha\mu} W^{\mu\beta} \right] \times Tr \left[W_{\beta\nu} W^{\nu\alpha} \right] \quad (1.46)$$

$$\mathcal{O}_{T,5} = Tr \left[W_{\mu\nu} W^{\mu\nu} \right] \times B_{\alpha\beta} B^{\alpha\beta} \quad (1.47)$$

$$\mathcal{O}_{T,6} = Tr \left[W_{\alpha\nu} W^{\mu\beta} \right] \times B_{\mu\beta} B^{\alpha\nu} \quad (1.48)$$

$$\mathcal{O}_{T,7} = Tr \left[W_{\alpha\mu} W^{\mu\beta} \right] \times B_{\beta\nu} B^{\nu\alpha} \quad (1.49)$$

$$\mathcal{O}_{T,8} = B_{\nu\mu} B^{\nu\mu} B_{\alpha\beta} B^{\alpha\beta} \quad (1.50)$$

$$\mathcal{O}_{T,9} = B_{\alpha\mu} B^{\mu\beta} B_{\beta\nu} B^{\nu\alpha} \quad (1.51)$$

The last two operators $\mathcal{O}_{T,8}$ and $\mathcal{O}_{T,9}$ are the operators which contain only neutral electroweak gauge bosons. The list of all quartic vertices modified by all the dimension-8 operators are listed in Table 5.1.

In this thesis, the aQGC study is performed in channel $pp \rightarrow W^\pm V jj$ and $pp \rightarrow ZV jj$, where V could be W-boson or the Z-boson which is only allowed to decay hadronically and the other boson is allowed to decay leptonic. This channel, WV and

	WWWW	WWZZ	ZZZZ	WWAZ	WWAA	ZZZA	ZZAA	ZAAA	AAAA
$f_{S,0}, f_{S,1}$	×	×	×						
$f_{M,0}, f_{M,1},$ $f_{M,6}, f_{M,7}$	×	×	×	×	×	×	×		
$f_{M,2}, f_{M,3},$ $f_{M,4}, f_{M,5}$		×	×	×	×	×	×		
$f_{T,0}, f_{T,1},$ $f_{T,2}$	×	×	×	×	×	×	×	×	×
$f_{T,5}, f_{T,6},$ $f_{T,7}$		×	×	×	×	×	×	×	×
$f_{T,8}, f_{T,9}$			×			×	×	×	×

Table 1.3: Quartic vertices modified by the different operators are marked with \times .

ZV (specially, the $W^\pm W^\pm$ and $W^\pm Z$) fusion channels are also of interest because they are involved during the production and decay of a heavy, singly or doubly charged Higgs boson. Thus, these channel also provide us the means of study the couplings of type $W^\pm ZH^\pm$ and $H^{\pm\pm}W^\pm W^\pm$ [18]. In this thesis the singly and doubly charged Higgs are considered in the framework of a specific model suggested by Georgi and Machacek [19] which is described in next section.

1.4 Georgi-Machacek Model

In Georgi-Machacek (GM) model along with the SM Higgs doublet $\Phi = (\phi^+, \phi^0)^T$ having hypercharge³, $Y = 1$, alongwith a real triplet $(\zeta^+, \zeta^0, -\zeta^{+*})^T$ with $Y = 0$ and a complex triplet $(\chi^{++}, \chi^+, \chi^0)^T$ with $Y = 2$ is introduced.

Also, a constraint from the electroweak parameter, ρ , also known as “*Custodial Symmetry*”, is imposed by the global $SU(2)_L \times SU(2)_R$ symmetry upon the scalar potential. The parameter ρ is given as

$$\rho = \frac{M_W}{M_Z \cos(\theta)} = 1, \quad (1.52)$$

where, θ is the weak mixing angle. An isospin doublet of the $SU(2)_L \times SU(2)_R$ is given as

$$\Phi = \begin{bmatrix} \phi^{0*} & \phi^+ \\ -\phi^{+*} & \phi^0 \end{bmatrix} \quad (1.53)$$

³ $Q = T^3 + \frac{Y}{2}$

and the triplet Higgs field is given as

$$X = (\epsilon_3 \chi^*, \zeta, \chi) = \begin{bmatrix} (\chi^0)^* & \zeta^+ & \chi^{++} \\ -(\chi^+)^* & \zeta^0 & \chi^+ \\ (\chi^{++})^* & (-\zeta^+)^* & \chi^0 \end{bmatrix} \quad (1.54)$$

The vacuum expectation values (vev) for the Φ

$$\langle \Phi \rangle = \frac{V_\phi}{\sqrt{2}} \mathbb{1}_{2 \times 2} \quad (1.55)$$

and for the field X is

$$\langle X \rangle = v_x \mathbb{1}_{3 \times 3} \quad (1.56)$$

where, $\mathbb{1}$ is the unit matrix and the W and Z boson to be massless provides a condition that

$$v_\phi^2 + 8v_\chi^2 = v = \frac{1}{\sqrt{2}G_F} \approx (246 \text{ GeV})^2 \quad (1.57)$$

The most general gauge invariant potential involving these fields that preserve the custodial symmetry is given as

$$\begin{aligned} V\Phi, X = & \frac{\mu_2^2}{2} Tr(\Phi^\dagger \Phi) + \frac{\mu_3^2}{2} Tr(X^\dagger X) \\ & + \lambda_1 [Tr(\phi^\dagger \phi)] + \lambda_2 Tr[(\phi^\dagger \phi) Tr(X^\dagger X)] \\ & + \lambda_3 Tr(X^\dagger X X^\dagger X) + \lambda_4 [Tr(X^\dagger X)]^2 \\ & - \lambda_5 Tr(\phi^\dagger \tau^a \phi \tau^b) Tr(X^\dagger t^a X t^b) \\ & - M_1 Tr(\phi^\dagger \tau^a \phi \tau^b) (UXU^\dagger)_{ab} \\ & - M_2 Tr(X^\dagger t^a X t^b) (UXU^\dagger)_{ab} \end{aligned} \quad (1.58)$$

where $\tau^a = \frac{\sigma^a}{2}$,

$$t^1 = \frac{1}{\sqrt{2}} \begin{bmatrix} 0 & 1 & 0 \\ 1 & 0 & 1 \\ 0 & 1 & 0 \end{bmatrix}, \quad t^2 = \frac{1}{\sqrt{2}} \begin{bmatrix} 0 & -i & 0 \\ i & 0 & -i \\ 0 & i & 0 \end{bmatrix}, \quad t^3 = \begin{bmatrix} 1 & 0 & 0 \\ 0 & 0 & 0 \\ 0 & 0 & -1 \end{bmatrix}, \quad (1.59)$$

The physical fields generated can be organized by the transformation properties under the custodial $SU(2)$ symmetry into pentaplet and a triplet and two singlets. They are:

$$\text{Pentaplet} : \quad H_5^{++} = \chi^{++} \quad (1.60)$$

$$H_5^+ = \frac{\chi^+ - \zeta^+}{\sqrt{2}} \quad (1.61)$$

$$H_5^0 = \sqrt{\frac{2}{3}}\zeta^{0,r} - \sqrt{\frac{1}{3}}\chi^{0,r} \quad (1.62)$$

$$(1.63)$$

$$\text{Triplet} : \quad H_3^+ = -S_H\phi^+ + C_H \frac{\chi^+ + X^+}{\sqrt{2}} \quad (1.64)$$

$$H_3^0 = -S_H\phi^{0,i} + C_H\chi^{0,i} \quad (1.65)$$

$$(1.66)$$

$$\text{Singlet} : \quad H_1^0 = \phi^{0,r} \quad (1.67)$$

$$H_1^{0'} = \sqrt{\frac{1}{3}}\zeta^{0,r} + \sqrt{\frac{2}{3}}\chi^{0,r}, \quad (1.68)$$

where,

$$S_H = \sin(\theta_H) = \frac{2\sqrt{2}v_\chi}{v} \quad (1.69)$$

$$C_H = \cos(\theta_H) = \frac{v_\phi}{v} \quad (1.70)$$

Here, within the pentaplets and the triplets, the masses are degenerated at the tree level and are given in terms of the parameters of scalar potential by

$$m_5^2 = \frac{M_1}{4v_\chi}v_\phi^2 + 12M_2v_\chi + \frac{3}{2}\lambda_5v_\phi^2 + 8\lambda_3v_\chi^2 \quad (1.71)$$

$$m_3^2 = \frac{M_1}{4v_\chi}v^2 + \frac{\lambda_5}{2}v^2 \quad (1.72)$$

The two custodial singlets will mix by an angle α to give the two mass eigenstate h and H ,

$$h = C_\alpha H_1^0 - S_\alpha H_1^{0'} \quad (1.73)$$

$$H = S_\alpha H_1^0 + C_\alpha H_1^{0'} \quad (1.74)$$

where, $C_\alpha = \cos(\alpha)$ and $S_\alpha = \sin(\alpha)$. The mixing is controlled by the mass matrix

$$M^2 = \begin{bmatrix} M_{11}^2 & M_{12}^2 \\ M_{12}^2 & M_{22}^2 \end{bmatrix} \quad (1.75)$$

where,

$$M_{11}^2 = 8\lambda_1 v_\phi^2 \quad (1.76)$$

$$M_{12}^2 = \frac{\sqrt{2}}{2} v_\phi \left[-M_1 + 4(2\lambda_2 - \lambda_5) v_x \right] \quad (1.77)$$

$$M_{22}^2 = \frac{M_1}{4v_\chi} v_\phi^2 - 6M_2 v_\chi + 8(\lambda_3 + 3\lambda_4) v_\chi^2 \quad (1.78)$$

A remarkable feature of the GM model is that the HWW and HZZ coupling may be larger than in the SM. The pentaplet Higgs bosons have coupling with the weak bosons while the triplet do not. Thus, the triplet Higgs bosons are said to be gauge-phobic while the pentaplets are known as fermi-phobic. But these pentaplets can couple to the massive vector boson where the coupling strength is proportional to the parameter S_H .

1.5 Thesis Organization

The current thesis is based on the hardware activities and physics analysis performed during the course of my Ph.D. The layout of the thesis is as follows:

The current chapter begins with a brief introduction to the Standard Model (SM) of particle physics, followed by a prelude to the main thesis topic, i.e. triple or quartic gauge couplings. A mathematical framework is discussed to explain the generation of triple/quartic gauge couplings in the SM, followed by the brief introduction of the Higgs mechanism and the anomalous triple and quartic gauge interactions based on the approach of Effective Field Theory (EFT). Finally, the chapter concludes with a discussion on the doubly charged Higgs model, i.e., Georgi-Machacek model.

Chapter 2 basically discusses the experimental apparatus used to collect the data for the physics studies reported in this thesis. This contains a description of the Large Hadron Collider (LHC) [20, 21, 22] and its one of the two general purpose detectors, i.e. the CMS detector [23]. The LHC is the world's most powerful particle accelerator and collider, located in a 27 km long tunnel, about 100 m underground

at Swiss-France border. Currently, the LHC is operating at 13 TeV center of mass energy with peak luminosity, $\mathcal{L} = 2.1 \times 10^{34} \text{ cm}^{-2}\text{s}^{-1}$ [24, 25]. Also, different sub-detector components of the CMS detector and their working mechanisms are outlined. The trigger system being used in the CMS detector for the data collection is also discussed which consists of the two-tier trigger. The first level (L1) of the CMS trigger consists of custom hardware process running synchronously with the LHC bunch crossing frequency of 40 MHz . This uses information from the calorimeters and muon detectors only to select the most interesting events within the time interval of less than $4 \mu\text{s}$. The second level trigger is known as the High-Level Trigger (HLT). This uses fast offline reconstruction algorithm that uses information from all sub-systems, i.e., calorimeters, muon system as well as tracker to decide to keep or reject the event. This step further decreases the event rate from around 100 kHz to about 100 Hz , before data storage.

Chapter 3 is devoted to the hardware activities carried out for the CMS muon detector system upgrade. Starting from a brief history of the gaseous detectors, the focus is shifted to the Gas Electron Multiplier (GEM) detectors which is one of the excellent gaseous detectors having unprecedented spatial resolution, larger sensitive/detection area, with higher rate capability and good operational stability over the longer operating periods. This detector is approved by the CMS collaboration for the upgrade of the CMS muon endcap system during Long Shutdown 2 (2019-2020). This upgrade project is named as GE1/1 upgrade, where the letter “G” stands for GEM, “E” stands for End-cap, the first “1” corresponds to the first muon station and the second “1” corresponds to the first ring of the station [26]. The proposed design and configuration of these GEM detectors are discussed along with their working principle. For observing the performance of the prototype of GEM in the real environment the GE1/1 detector was tested in several beam tests. This thesis describes the details and results from the 2014 beam test in terms of measured efficiency, time resolution and cluster size. In this beam test we tested the GE1/1 detector with both gases Ar : CO_2 and $\text{Ar : CO}_2 : \text{CF}_4$. One of important conclusion that we can operate our detector without using the CF_4 gas, which is non-eco friendly, without compromising with the efficiency and the time resolution of $> 98\%$ and $5 - 7 \text{ ns}$ respectively.

Also, this thesis contains the characterization studies of the GEM foil developed in India. An Indian company, Micropack Pvt. Ltd., got the technology of GEM foil

production through the Transfer of Technology (TOT) agreement with CERN. After several trials, Micropack successfully produced the $10\text{ cm} \times 10\text{ cm}$ GEM foils using the double mask technique [27]. This GEM foil is characterized by using the optical and electrical method. The results are mentioned in terms of the defects and the leakage current in GEM foil that we observed about 0.13% and $\pm 5\text{ nA}$ at 600 V, respectively.

Chapter 4 reports the various steps and procedures followed in the analysis for the Anomalous Quartic Gauge Couplings (aQGC) measurement using the model independent way using the Effective Field Theory (EFT) for the dimension-eight operators with the data collected during 2016 (36 fb^{-1}) in the proton-proton collision at 13 TeV by the CMS detector. Among all the allowed processes, the process $pp \rightarrow WVjj$ and $pp \rightarrow ZVjj$ is used for the study. Here V denotes for W or Z boson and it always decay hadronically. The other vector boson in channel decays leptonically. The study starts with measuring the interference between the electroweak process $pp \rightarrow VVjj$ and the QCD initiated process. The study showed that we have less than 1% interference between the two. The major background $W + jets$ was estimated in a data-driven way using the alpha-ratio method. The events are selected by requiring two jets with large rapidity separation having large di-jet invariant mass, one or two leptons (electrons or muons), and a boosted W or Z boson decaying hadronically. The hadronically decaying W/Z boson is reconstructed as one large radius jet having radius parameter 0.8. Finally, the limits on the dimension-eight operators are given using the frequentist approach in asymptotic approximation.

Chapter 5 provides a summary of the work done during this PhD thesis for the physics analysis and the hardware work on the GE1/1 upgrade along with the lab development and the characterization of the GEM foil at the University of Delhi, India using the Indian made GEM foil. Also, this discusses the future prospects of physics and hardware upgrade.

2

The LHC and CMS Detector

In this chapter, the working and the design parameters of the Large Hadron Collider (LHC) and one of its general purpose detector, Compact Muon Solenoid (CMS), are briefly described.

2.1 The Large Hadron Collider

The famous quote “*history repeats itself*” applies well to the High Energy Physics (HEP) experiments. The starting point of experimental particle physics was the Rutherford α -particle scattering, which was proposed by Ernest Rutherford and carried out by his two assistants - Hans Geiger and Ernest Marsden - in the early 20th century [28]. In this experiment, a beam of α -particles was fired at a thin gold foil and its scattering was observed on the photographic screen. Based on their experimental findings, they suggested the structure of the atom as we know it today, in which most of the mass is centred at the core of the atom known as the nucleus, and electrons revolve around it. One hundred years after this classic experiment, the same techniques are employed today to explore the most basic constituents of the matter. Only, the technique changed from “*natural accelerator*”¹ to the “*man-made*” accelerator. The man made accelerator, also known as particle accelerator, can accelerate particles with speed close to the speed of light. The design and working of the particle accelerator has changed a lot over the period of time in going from eV to GeV and now to TeV range. Nowadays, accelerators are not only used in HEP experiments, but also extend their arenas to medical sciences such as production of

¹radioactivity and cosmic rays

radioisotopes for cancer treatments, 3-D X-rays, etc. and to the industrial applications involving material processing, sterilization, security scan, water treatment, and many more [29].

The Large Hadron Collider (LHC) is one such accelerator, and as the name suggests, it is a hadron collider which can accelerate two proton beams, moving in opposite direction, to a maximum of 14 TeV center of mass energy in a 26.7 km long tunnel which is about 100 m underground spanning border areas of France and Switzerland. The LHC is the latest and the most-powerful particle accelerator and collider is built to improve our understanding of fundamental physics. It started its operation on 21st October 2008 and is housed in the tunnel previously used by Large Electron Positron (LEP) Collider. The European Organization for Nuclear Research (CERN) decided to switch this to hadron collider because of the following advantages:

- A hadron collider can reach higher centre of mass energy because of very low synchrotron radiation² emitted by hadrons as compared to electrons. Synchrotron radiation loss is directly proportional to $(Energy/mass)^4$.
- As hadrons are composite particles, they allow the possibility to scan over wider range of energies.

All particle accelerators have three major components:

- Beam pipes
- Accelerating structure
- Magnet system

These components are explained briefly in the following sub-sections for the LHC.

2.1.1 Beam Pipes

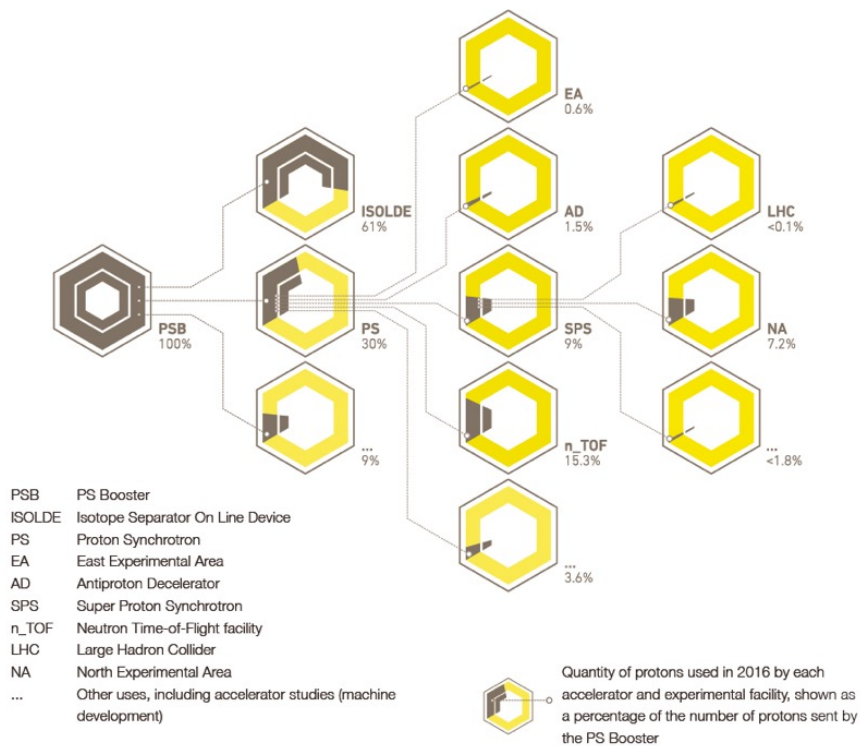
At the LHC, there are two beam pipes - each having a diameter of ≈ 6.3 cm in which proton beams travel in opposite directions. To avoid beam instability and loss of beam particles due to collision with gas molecules the beam pipes are kept at ultra-high vacuum³ maintained at 1.013×10^{-13} bar pressure.

²The radiation emitted by a charged particle during acceleration in a circular path is known as synchrotron radiation. As particles lose energy in emission of this radiation, an additional energy must be provided to keep the beam at constant energy.

³At LHC, three different vacuum systems are used. First one is used for beam pipe; second one for insulating the cryogenically cooled magnets and third one is used for insulating the helium

2.1.2 Accelerating Structure

Another main part of any particle accelerator is its accelerating structure. An accelerator in the TeV range cannot accelerate particles at rest to the energies of the order of TeV in a single go. It should go into several stages depending on the energy. At LHC, the journey of a proton starts with pulling the proton out from the Hydrogen gas and subsequently going into five different acceleration stages. The number of acceleration stages can be decreased but not to one because of hardware restrictions. At LHC, there are five different stages before reaching to maximum energy and at each stage, it serves several other experiments which are shown pictorially in Figure 2.1.



1.34×10^{20} protons were accelerated in the accelerator complex in 2016. This might sound like a huge number, but in reality it corresponds to a minuscule quantity of matter, roughly equivalent to the number of protons in a grain of sand. In fact, protons are so small that this amount is enough to supply all the experiments. The LHC uses only a tiny portion of these protons, less than 0.1%, as shown in the diagram.

Figure 2.1: Other experiments at the LHC accelerating chain [30]

The stages for proton acceleration are:

distribution. In the latter two it just acts as a thermal insulator as the cryogenic parts are kept at 1.9 K (-271.3°C)

- ***Grab proton source***: The Duoplasmatron [21] strips electron from the hydrogen gas and creates a plasma of protons, electrons and molecular ions. This plasma expands towards the extraction electrodes and a proton beam is formed. This feeds protons to the Linear accelerator-2 (LINAC2).
- ***LINAC2***: It is the starting point of proton's journey in the LHC accelerator complex. Here, proton beams are accelerated to an energy of 50 MeV using the radio-frequency (RF) cavities⁴. LINAC2 further feeds to the Proton Synchrotron Booster (PSB).
- ***PSB***: The 50 MeV proton beams from LINAC2 are injected into the PSB. The PSB accelerates them to 1.4 GeV for injection into the Proton Synchrotron (PS).
- ***PS***: It is one of the key components in the LHC accelerator complex. It increases the energy of protons up to 25 GeV and feeds them to the Super Proton Synchrotron (SPS).
- ***SPS***: It has a circumference of 7 km where protons are accelerated to an energy of 450 GeV . Protons are further injected into the LHC ring via two transmission lines.
- ***LHC***: It accepts the two proton beams from SPS which are injected into opposite directions in two parallel pipes. In LHC, proton beams can be accelerated up-to 7 TeV .

The CERN accelerator complex is shown in Figure 2.2.

2.1.3 Magnet System

Since the LHC is a circular collider; the magnet system is one of its core parts as it provides a circular trajectory to the particles in the LHC beam pipes. In order to be economical, LHC has been made in eight arcs and eight straight sections instead of a perfect circle. Apart from bending the beam, it is also necessary to focus the proton beams. This is accomplished using a pair of quadrupole magnets, where the first magnet focuses the width while the second magnet focuses the beam height as

⁴An RF cavity is a metallic cavity that accelerates the charged particles using the electromagnetic field.

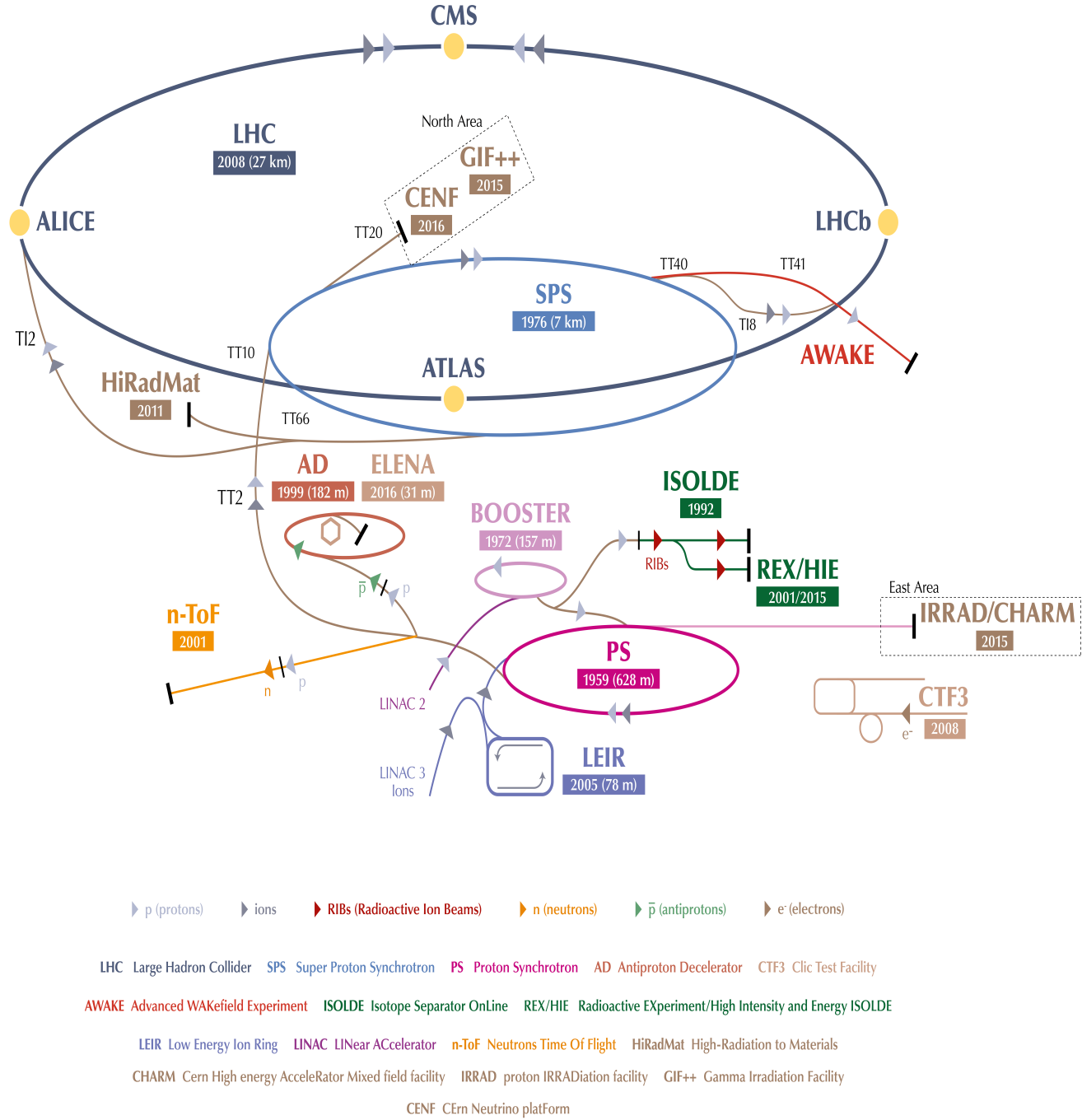


Figure 2.2: The LHC accelerator chain along with all its other experiments which use proton beam from different parts of the accelerator, either from PSB, PS or SPS [31]

shown in Figure 2.3. A total of 858 quadrupole magnets are installed in LHC to keep the beams focused.

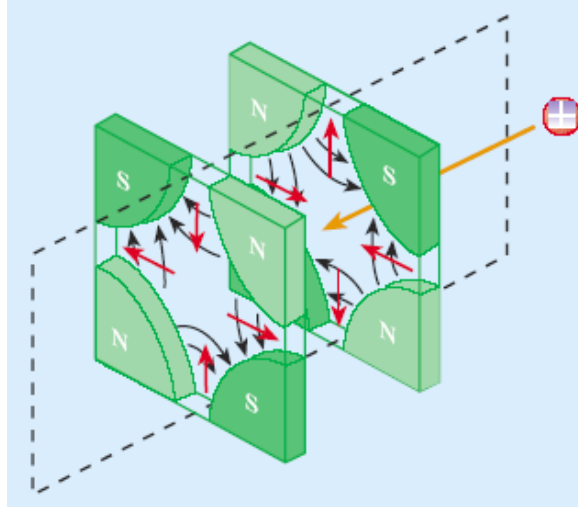


Figure 2.3: Pair of quadrupole magnets [32].

Sextupole magnets are also used for proper focusing as every proton in the beam is not exactly with the same energy and on the same path. Several other magnetic multipoles are used to keep the beam focused in case the beam suffers from gravitational interactions over protons, electromagnetic interactions among bunches or electron clouds from pipe wall, and so on. The details of the different types of magnets used in LHC are listed here [33]. Besides, there are eight sets of “*inner triplets*” used at the four interaction points (IPs) to focus the beams during the collisions to increase the luminosity. The size of the bunch goes from 0.2 mm to 17 μm and 71 μm at the interaction point of ATLAS (A Toroidal LHC Apparatus) & CMS (Compact Muon Solenoid) and ALICE (A Large Ion Collider Experiment) & LHCb (Large Hadron Collider beauty), respectively. A list of important parameters of the LHC is given in Table 2.1.

2.2 Key requirements of a particle accelerator

The HEP collider is characterised on the basis of two parameters - the centre of mass energy and the luminosity. The production rate of heavier particles like Higgs increases with the centre of mass energy. Luminosity (\mathcal{L}) measures the ability of a collider to produce the required number of interactions. It is the proportionality

Parameters	Value
Circumference of LHC ring	26658.883 m
Maximum dipole magnetic field	8.33 T
Dipole operating temperature	1.9 K
Maximum stored energy per beam (nominal)	362 MJ
Maximum stored energy per beam (2012)	143 MJ
Maximum stored energy per beam (2016)	266 MJ
Beam energy at Injection	450 GeV
Beam energy at collision (nominal)	7 TeV
Beam energy at collision (2012)	4 TeV
Beam energy at collision (2016)	6.5 TeV
Maximum instantaneous luminosity (nominal)	$10^{34} \text{ cm}^{-2} \text{ s}^{-1}$
Maximum instantaneous luminosity (2012)	$7.7 \times 10^{33} \text{ cm}^{-2} \text{ s}^{-1}$
Maximum instantaneous luminosity (2016)	$1.4 \times 10^{34} \text{ cm}^{-2} \text{ s}^{-1}$
Number of bunches per proton beam (nominal)	2808
Number of bunches per proton beam (2012)	1380
Number of bunches per proton beam (2016)	2076
Maximum number of protons per bunch	1.6×10^{11}
Protons/bunch (average at start of collision) (nominal)	1.15×10^{11}
Protons/bunch (average at start of collision) (2012)	1.5×10^{11}
Protons/bunch (average at start of collision) (2016)	1.1×10^{11}
Bunch collision frequency (nominal)	40 MHz
Bunch collision frequency (2012)	20 MHz
Bunch collision frequency (2016)	40 MHz
Bunch length (at injection)	1.7 ns
Bunch length (at collision)	1.05 ns
Energy spread (at injection)	1.9×10^{-3}
Energy spread (at collision)	0.45×10^{-3}
Half crossing angle (nominal)	$143 \mu\text{rad}$
Half crossing angle (2012)	$146 \mu\text{rad}$
Half crossing angle (2016)	$185 \mu\text{rad}$
β^* (nominal)	0.55 m
β^* (2012)	0.6 m
β^* (2016)	0.4 m
RMS beam size at IP1 & IP5	$17 \mu\text{m}$
RMS beam size at IP2 & IP8	$71 \mu\text{m}$
ϵ_n (transverse emittance, RMS, normalized) (at injection)	$3.5 \mu\text{m}$
ϵ_n (transverse emittance, RMS, normalized) (at collision point)	$3.75 \mu\text{m}$
total longitudinal emittance (at injection)	1.0 eVs
total longitudinal emittance (at collision)	2.5 eVs
Average mean pile-up (nominal)	25
Average mean pile-up (2012)	21
Average mean pile-up (2016)	27
Energy loss per turn at 14 TeV	7 keV
Energy loss per turn for electrons at 104.6 GeV	40,000 keV

Table 2.1: LHC technical parameters for proton-proton collisions: nominal, 2012 and 2016 values.[34, 35, 36, 22, 24].

factor between the number of events per second dR/dt and the cross-section σ_p [25].

$$\frac{dR}{dt} = \mathcal{L} \cdot \sigma_p , \quad (2.1)$$

The unit of luminosity is $cm^{-2}s^{-1}$.

Luminosity calculation

Luminosity is defined as:

$$\mathcal{L} = \frac{k_b N_1 N_2 f_{rev} \gamma}{A_{eff}} , \quad (2.2)$$

Where, k_b is the number of bunches per beam, N_1 and N_2 are the number of protons in the two bunches, f_{rev} the revolution frequency of proton beams, and A_{eff} is the effective transverse area of the beam. The different parameters of the beam as showing in the Fig. 2.4. For a Gaussian beam with spread σ_x and σ_y in x and y direction

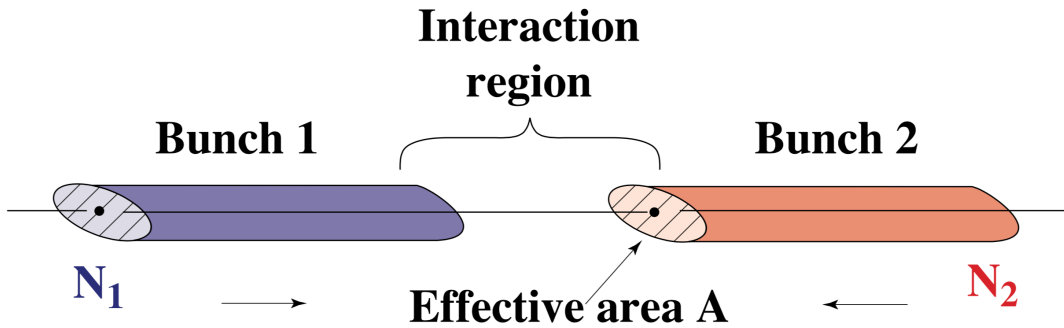


Figure 2.4: Layout describing the bunch parameters and interaction area.

respectively, the effective area will be $4\pi\sigma_x\sigma_y$, so that

$$\mathcal{L} = \frac{k_b N_1 N_2 f_{rev} \gamma}{4\pi\sigma_x\sigma_y} , \quad (2.3)$$

The beam size, $\sigma_x \cdot \sigma_y$, can be expressed in terms of transverse beam emittance⁵ (ϵ_n) and the amplitude function⁶ (β^* , also known as beta-function). The amplitude function can be expressed in terms of cross-sectional size of the bunch ($\sigma_x \cdot \sigma_y$) and the transverse emittance (ϵ_n). The amplitude function β becomes

$$\beta^* = \frac{\pi \cdot \sigma_x \cdot \sigma_y}{\epsilon_n}, \quad (2.4)$$

If the amplitude function is small, the beam will be narrower and squeezed. If it is high, the beam will be wide and straight. It has unit of length. Thus, we can express luminosity in terms of transverse emittance and the amplitude function as

$$\mathcal{L} = \frac{k_b N_1 N_2 f_{rev} \gamma}{4\pi \epsilon_n \beta^*}, \quad (2.5)$$

Based on the definition of luminosity, we can maximise it by following ways:

- By decreasing beam emittance, ϵ_n .
- By improving the cryogenic system as the factor $k_b \cdot N_1 \cdot N_2$ is limited by thermal energy produced by synchrotron radiation.
- By decreasing beam-beam effect [37, 38], since it scales with N_b/ϵ_n which causes the spread in betatron tunes [39].
- Also, the space charge [40] scales with N_b/ϵ_n .

Integrated luminosity

The maximum luminosity or the instantaneous luminosity is an important quantity but the final figure of merit is the **integrated luminosity** as it directly gives us the total number of observed events over a period of time:

$$\mathcal{L}_{int} \cdot \sigma_p = \text{number of events of interest}, \quad (2.6)$$

⁵The transverse emittance is a beam quality concept reflecting the process of bunch preparation (the injector chain), extending all the way back to the source for hadrons. A low emittance particle beam is a beam where the particles are confined to a small distance and have nearly the same momentum. In a colliding beam accelerator, keeping the emittance small means that the likelihood of particle interactions will be greater resulting in higher luminosity. The emittance changes as a function of the beam momentum; increasing the energy of the beam reduces the emittance.

⁶The amplitude function, β^* , is determined by the accelerator magnet configuration (basically, the quadrupole magnet arrangement) and powering.

where, L_{int} is defined as the integral of the delivered luminosity over time. It is the measurement of the collected data size.

$$\mathcal{L}_{int} = \int_0^T L(t') dt' , \quad (2.7)$$

Its unit is $barn^{-1}$. Figure 2.5 shows the integrated luminosity of 2016 as compared to the previous years.

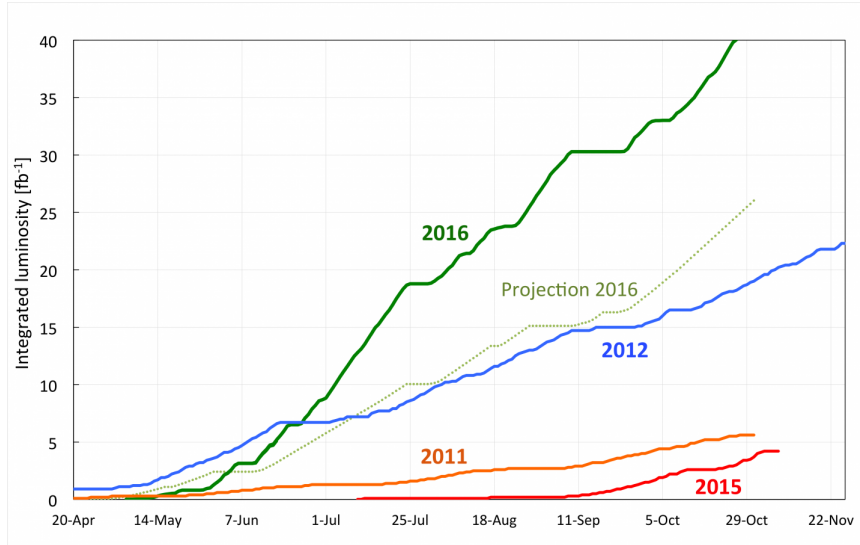


Figure 2.5: The integrated luminosity of the LHC with proton-proton collisions in 2016 compared to previous years [41]. The recorded luminosity in 2016 far surpassed the expected luminosity and it almost doubled the luminosity recorded in 2012.

2.3 Experiments at the LHC

At the LHC there are four IPs where the two proton beams are made to collide. At each IP, one detector is placed. These are - ATLAS, CMS, ALICE, and LHCb as shown in Figure 2.6. In addition to these, there are two more small detectors LHCf and TOTEM installed close to the IP of the two main detectors ATLAS and CMS respectively.

ATLAS (A Toroidal LHC Apparatus) and **CMS** (Compact Muon Solenoid) are large

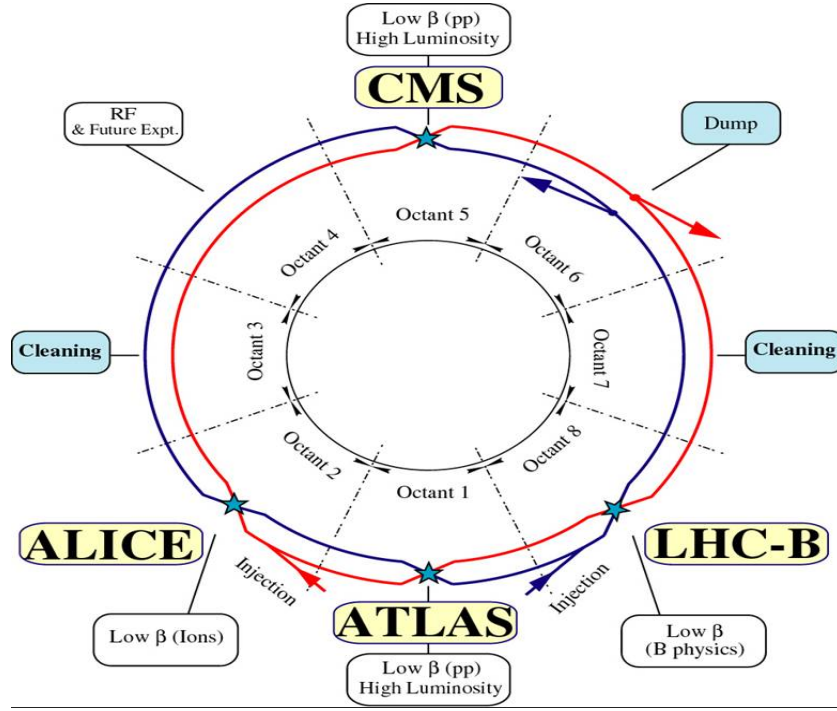


Figure 2.6: LHC geometry with arcs and straight sections [42].

general-purpose⁷ detectors with similar design and physics goal. The main difference between the two is in their magnet systems which is motivated by the momentum resolution of muons. The momentum resolution for muons, $\Delta p_T/p_T$, is proportional to $B^{-1}L^{-2}$, where B is magnetic field and L is the lever arm defined as the distance of momentum measurement from the IP of detector. So, to improve the momentum resolution there are three possible choices.

1. To increase B while maintaining a compact design, or
2. To work with low B with long L , and
3. To increase both L and B , but this increases the cost of the detector by several factors. Hence, it is not the preferred choice usually.

CMS uses the first point, i.e., to increase the magnetic field with compact design⁸ while ATLAS uses the design with low magnetic field with long lever arm.

⁷Here, general purpose means this machines will be used for many different kind of physics searches.

⁸This is why there is word **compact** in the name of CMS.

ALICE (A Large Ion Collider Experiment) is a heavy-ion detector. It is specially designed for the study of strongly interacting matter at high densities in quark-gluon plasma phase.

LHCb (Large Hadron Collider beauty) is made asymmetrically with respect to the IP of the detector. It is designed specially to investigate the matter-antimatter asymmetry through the study of b-quarks.

LHCf (Large Hadron Collider forward) and **TOTEM** (TOTal cross-section, Elastic scattering and diffraction dissociation Measurement at the LHC) are there for the study of forward physics.

2.4 CMS Detector

The design and components of any HEP detector depend upon its physics goals and operational parameters of the particle accelerator where it is installed. In case of the CMS detector, following challenges are imposed by the LHC accelerator:

1. **High luminosity:** A high delivered luminosity implies that whenever two proton bunches cross each other there will be more than one p-p interactions also known as “pile-up”⁹. Figure 2.7 shows the mean number of interactions for year 2016 and previous years. Given this, there will be more than $\mathcal{O}(1000)$ particles passing through detector during every p-p collision. Thus, the detector should be highly granular which means an increased number of readout channels, synchronised with LHC clock.
2. **Response time:** At LHC, the two proton beams cross each other at every 25 ns. So, the response time of all the sub-detector systems should be less than 25 ns.
3. **Radiation hardness:** At every 25 ns, the detector is bombarded with more than 1000 particles so all the sub-detectors should be radiation hard including its electronics, cables, glue, screws, and so on.

⁹Pile-up can be theoretically estimated as the product of inelastic p-p cross-section (σ_{inel}), instantaneous luminosity (\mathcal{L}) and the mean time interval between two collisions, ($< t >$).

$$\text{mean pile-up} = \sigma_{inel} \times \mathcal{L} \times < t > , \quad (2.8)$$

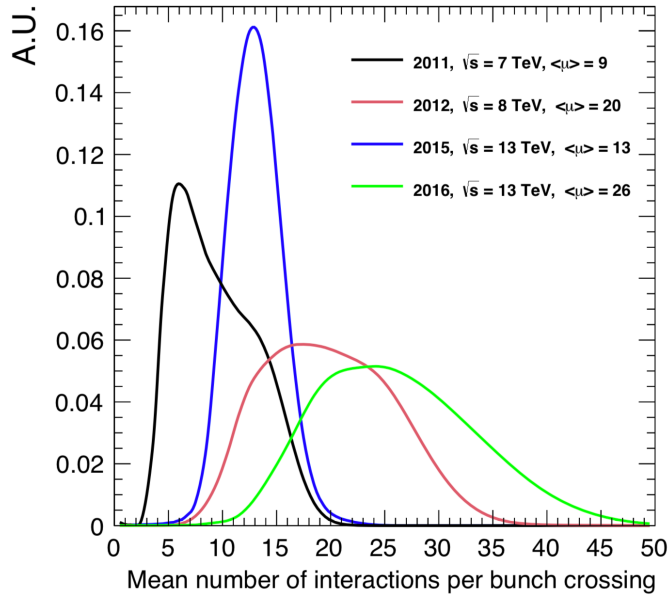


Figure 2.7: Mean number of interactions per bunch crossing in p-p collision [43].

Restrictions imposed on detector from the physics goals of the LHC:

1. Good muon identification and momentum resolution ($\approx 1\%$ at 100 GeV).
2. Efficient triggering and tracking of b-jets and τ 's.
3. Highly efficient and granular electromagnetic calorimeter to detect and measure energies of electrons and photons.
4. Good missing transverse energy resolution and di-jet mass resolution require a “hermetic” hadron calorimeter with full geometric coverage and fine lateral segmentation.

Based on the above conditions the CMS detector is designed in a cylindrical shape such that each sub-detector component is on top of the other, with the beam pipe at the centre. To have a full geometric coverage, it is designed with a barrel region and two endcap regions. The main part of the CMS detector is its superconducting magnet system, capable of producing a highly uniform magnetic field of 4T to accurately measure the high momentum particles. While the muon detector system is kept outside the magnet but sandwiched in its return yoke, the tracking system, the calorimeters Electromagnetic CALorimeter (ECAL) and Hadronic CALorimeter

(HCAL) are placed inside the magnet. The CMS detector design is shown in Figure 2.8.

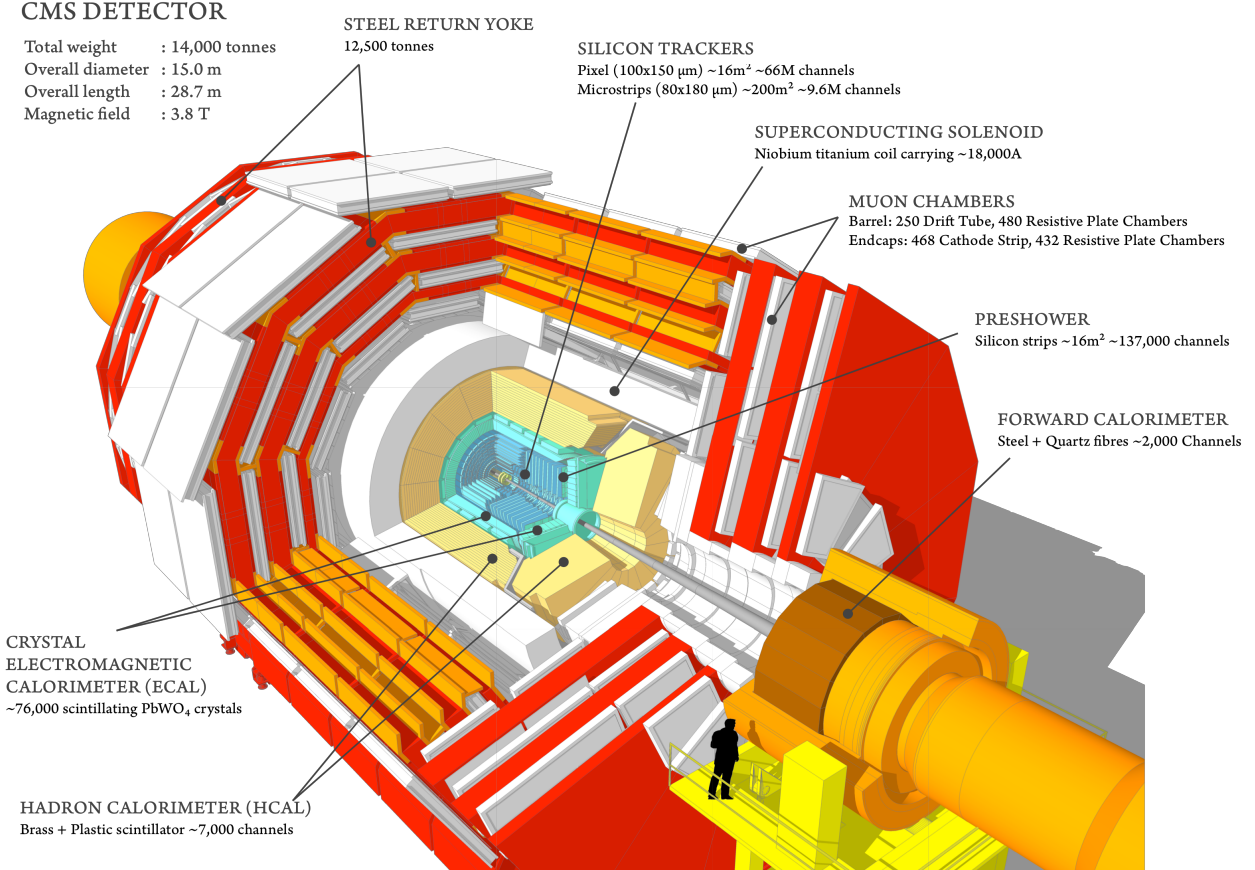


Figure 2.8: CMS detector drawing [44].

The above mentioned shape of CMS was inspired by all the known particles that will reach to the CMS detector. The known particle that will reach CMS detector are e^\pm , μ^\pm , γ , π^\pm , k^\pm , p, n, k_L and k_S . These can be grouped in two categories based on electromagnetic and strong interactions. All the strongly interacting particles will be detected by HCAL while all the electromagnetic interacting particles should be detected by ECAL. But only electrons and photons are detected by ECAL not muons. As it will not bremsstrahlung because it is too heavy than electrons (as bremsstrahlung is inversaly proportional to $mass^4$). Since muons can not interact via strong force it will pass through ECAL as well as HCAL. Thus CMS is installed in a seperate muon system outside ECAL and HCAL.

2.4.1 Coordinate System

The right handed coordinate system is used in the CMS detector having origin at the nominal IP (Figure 2.9). The z-axis is considered along the beam direction in a way that x-axis and y-axis point radially to the centre of the LHC ring and in upward direction, respectively. The azimuthal angle, ϕ , is measured in the x-y plane from x-axis and the polar angle, θ , is measured from the z-axis. Instead of describing a particle at some polar angle, we prefer to use the variable pseudo-rapidity. It is defined as

$$\eta = -\ln \left[\tan \left(\frac{\theta}{2} \right) \right], \quad (2.9)$$

In the hadron collider, the use of pseudo-rapidity was motivated from the invariance of its difference, $\Delta\eta$, with respect to the particle boost direction. Also, the particle density remains constant in the barrel region of the detector, measured in equal rapidity intervals.

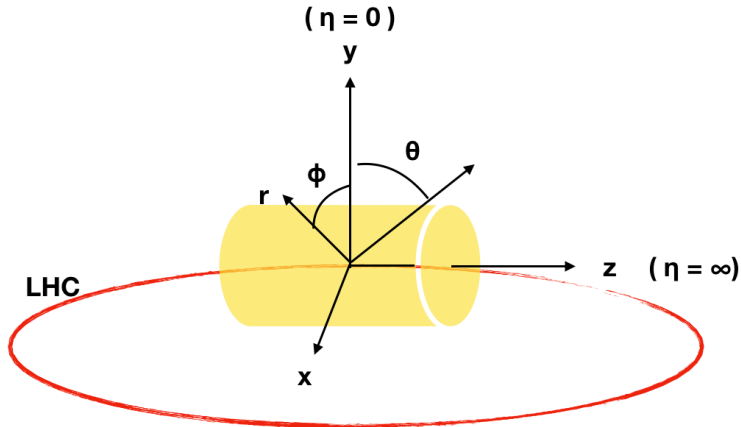


Figure 2.9: The right handed coordinate system used by CMS.

2.4.2 CMS sub-systems

Magnet

The magnet system (see Fig. 2.10) of CMS consists of a superconducting solenoid magnet which is 12.5 m in length and has an inner diameter of 6m. The size of the solenoid is large since the tracker, electromagnetic calorimeter and hadron calorimeter are placed inside it. In the barrel region, it generates a homogeneous magnetic field

of 3.8 T. The high magnetic field ensures an appropriate bending power for the highly energetic charged particles for a precise momentum measurement. Outside the solenoid, an iron yoke is placed for the returning magnetic field. The magnetic field strength inside the iron yoke is 2 T.



Figure 2.10: CMS Magnet system [45].

Tracker

The tracker is the first detector that encounters the particles emerging from the p-p collisions. Its purpose is to measure precisely the tracks of all charged particles crossing it. Also, it helps to reconstruct the secondary vertices to tag heavy flavour particles like b-jets or tau leptons. The particle rate is the highest in the tracker. So, it should be highly granular and response time should be fast. This condition results in a high density of on-detector electronics and this implies a large amount of material that conflicts with the aim of low material to reduce multiple scattering, bremsstrahlung, photon conversion and nuclear interactions. Thus, the type, design and number of layers of the tracker is a trade-off between the performance, the amount of material, and the cost. Considering these things in mind, the CMS collaboration decided to have first three layers of silicon pixel detector to precisely measure the primary vertex, secondary vertex and the impact parameter with a total surface area

of $1\ m^2$ and 66 million pixels followed by 10 layers of silicon micro-strip detectors covering a total area of $200\ m^2$. The tracker has a length of 5.8 m and an outer diameter 2.6 m and acceptance is up to $|\eta| < 2.5$. Tracker's cross sectional view is shown in Figure 2.11.

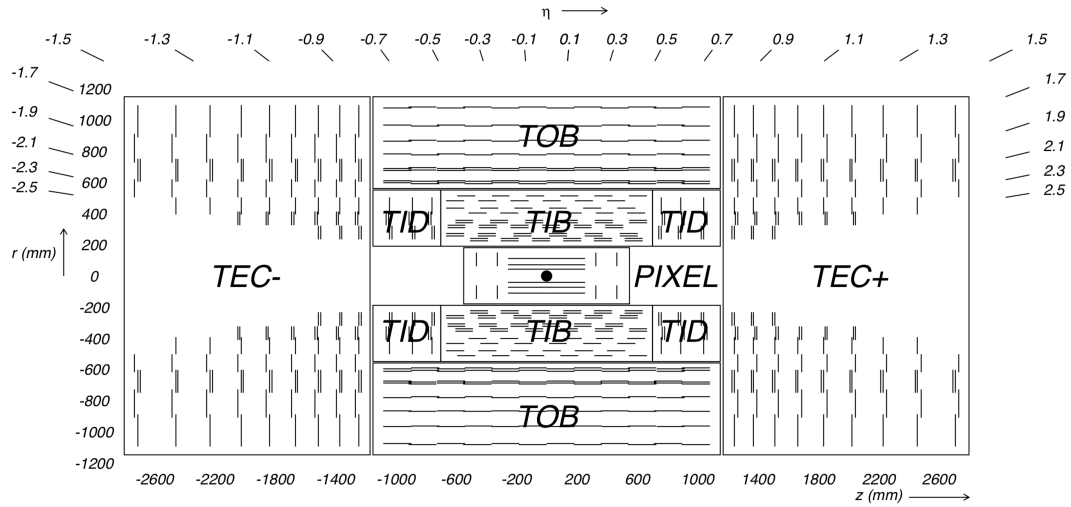


Figure 2.11: A systematic cross section view of CMS tracker showing silicon pixel and strip detectors. Double lines show back-to-back modules that deliver stereo hits.

Calorimetry

In general, a calorimeter is a device that measures the energy of the particles by absorption. The CMS detector uses two different types of calorimeter based on particle interactions- ECAL and HCAL. As the name suggests, the ECAL is designed to measure the particles (like electrons and photons) that primarily interact via electromagnetic interaction while the HCAL is designed to measure particles (Hadrons, particles made up of quarks and gluons for example protons, neutrons, kaons and pions) that interact via strong nuclear interactions.

The ECAL is a homogeneous calorimeter made from lead tungstate ($PbWO_4$) crystals, having a coverage of up to $\eta < 3.0$ including a pre-shower system in the forward region. The scintillation produced in the barrel region is detected by avalanche photo-diodes and it is collected by vacuum photo-triodes in the endcaps. In terms

of radiation length¹⁰, X_0 , its thickness is $25X_0$ which guarantees almost full shower containment.

In between ECAL and magnet system, the brass/scintillator sampling HCAL with coverage up to $\eta < 3.0$ is placed. To have a full geometric coverage it extends up to $\eta < 5.0$ using forward sampling iron/quartz-fibre calorimeter. This is crucial to measure the (missing) transverse energy of the event.

The Muon System

It is evident from the name of the CMS detector that a precise detection of muons is one of its main targets. It is motivated by the presence of muons in the final state of many interesting physics processes, such as the decay of Higgs boson into ZZ which subsequently decays into four leptons and especially, the case where all four leptons are muons, are referred to as the “gold plated” channel as we can detect muons efficiently over higher background contributions at LHC. At CMS, the muon system serves three different functions viz. identification, momentum measurement and triggering of muons. The strong superconducting magnet system with its return yoke of CMS, helps to acquire good momentum measurement and triggering capabilities. The return yoke of magnet system also serves as the hadron absorber. Only muons leave their tracks in the muon detector system, as all other particles are already absorbed by the calorimeters. Thus, the appearance of charged particle in the muon system signifies that it can only be from muon. The track left by muon in the CMS detector is illustrated in Figure 2.12. The layout of the CMS muon detector system is shown in Figure 2.13. Three different types of gaseous detectors used for the muon system were chosen based on the background level, muon rate, uniformity and magnitude of magnetic field. Drift tubes (DT) are used as tracking detector in the barrel region with relatively lower magnetic field intensity and have lower background rates as compared to the endcaps. For the endcap regions, Cathode Strip Chambers (CSC) are employed as they provide precise information about muons momentum and timing information even under high radiation environment. The pseudo-rapidity coverage of DTs is $|\eta| < 1.2$ and for CSCs is $0.9 < |\eta| < 2.4$. Along with DTs and CSCs, Resistive Plate Chamber (RPC) detectors are also installed to have a fast dedicated muon triggering

¹⁰Radiation length is defined as the mean length travelled by the particle to reduce its energy by a factor of $1/e$.

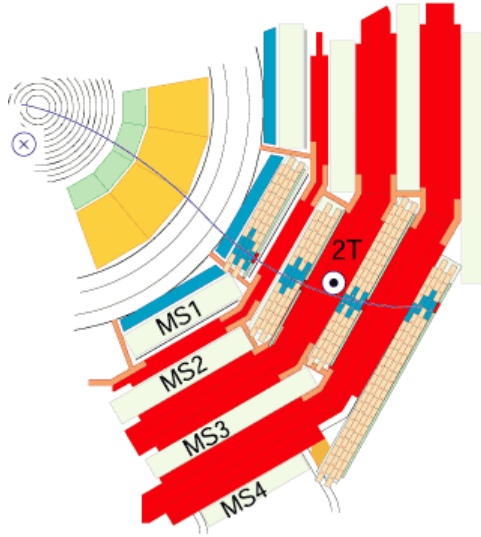


Figure 2.12: A muon leaves curved trajectory in LHC and the bending changes as the magnetic field direction of solenoid inside and outside are opposite.

system in both barrel and endcap region up to $|\eta| < 1.6$ [46]. The CMS muon detector system covers the geometric region up to $|\eta| < 2.4$ but RPCs are deployed up-to $|\eta| < 1.6$ as RPCs cannot withstand the radiation level after pseudo-rapidity region of 1.6. Thus to reconstruct muons in pseudo-rapidity region higher than 1.6 during Long Shutdown-2 (LS2, 2019-2020), CMS collaboration decided to employ Gas Electron Multiplier (GEM) detectors in region $1.6 < |\eta| < 2.2$, which is able to provide good space resolution and time resolution even in high environment radiation. The pseudo-rapidity range is limited to $|\eta| < 2.2$ because of space constrains. GEM detectors are described in details in Chapter 3. Summary of CMS detector sub-system including its main characteristics and composition is given in Table 2.2.

2.4.3 CMS Trigger and Data Acquisition system

The LHC produces about 1 billion of p-p collisions every second. During each collision thousands of particles are produced that cross the CMS detector. Reconstruction of all these particles generate several Terabytes of data. However, till date we neither have a switch with the required bandwidth that can transfer this enormous data for further processing nor the disk space to store all of them. Though if we have one, only a few fractions of data that are interesting for new physics or help us to understand the existing one as most of the collisions are the low-energy glancing collisions instead

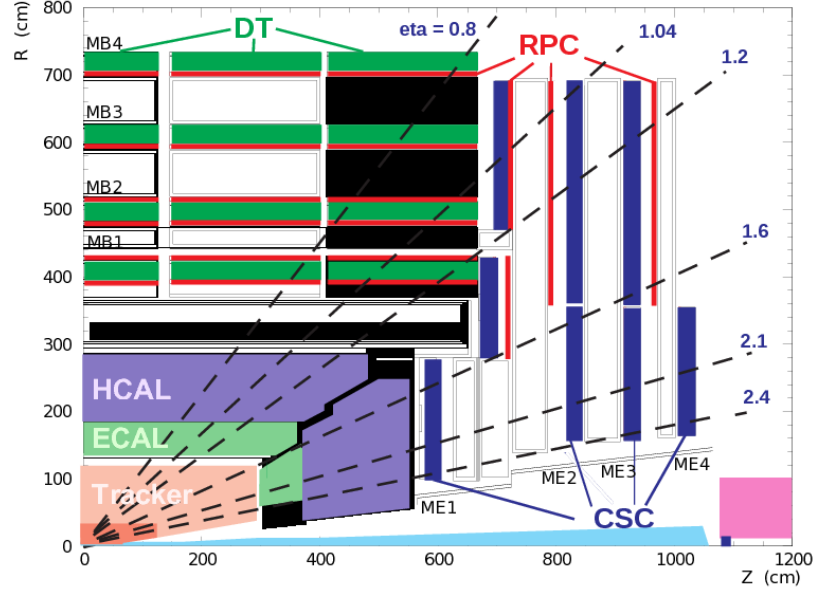


Figure 2.13: Longitudinal layout of one quadrant of the CMS detector. There are four DT stations named MB1-MB4 marked with green colour. Four CMS systems in high pseudo-rapidity region named ME1-ME4 in blue colour. Also, there are several RPC stations in barrel region and part of endcap region marked with red colour.

Sub-system	Composition	Characteristics
Tracker	Silicon strip and pixel detector	isolated track efficiency $\epsilon > 95\%$ within jets $\epsilon \sim 90\%$ primary vertex resolution: $10\text{-}20 \mu\text{m}$ p_T resolution: $\Delta p_T/p_T = 1\% (0.1 \text{ TeV}), 10\% (\text{TeV})$ coverage $\eta < 2.4$
ECAL	$PbWO_4$ crystals	energy resolution: $\left(\frac{\sigma}{E}\right)^2 = \left(\frac{2.7\%}{\sqrt{E}}\right)^2 + \left(\frac{210}{E}\right)^2 + 0.55\% \text{ (barrel)}$ $\left(\frac{\sigma}{E}\right)^2 = \left(\frac{5.7\%}{\sqrt{E}}\right)^2 + \left(\frac{245}{E}\right)^2 + 0.55\% \text{ (end-caps)}$ coverage $\eta < 3$
HCAL	Cu-Zn scintillators	energy resolution: $\left(\frac{\sigma}{E}\right)^2 = \left(\frac{68\%}{\sqrt{E}}\right)^2 + 4.5\%$ coverage $\eta < 3$
Muon system	Gaseous detectors	efficiency $\epsilon \sim 98\%$ $\Delta p_T/p_T = 8\text{-}15 \% (0.01 \text{ TeV})/20\text{-}40\% (\text{TeV})$ coverage $\eta < 2.4$

Table 2.2: Main characteristics of the CMS sub-system [47]

of head-on interaction. Also, this can be understood from the SM cross-section of pp as compared to the other process shown in Fig. 2.14. The maximum amount of

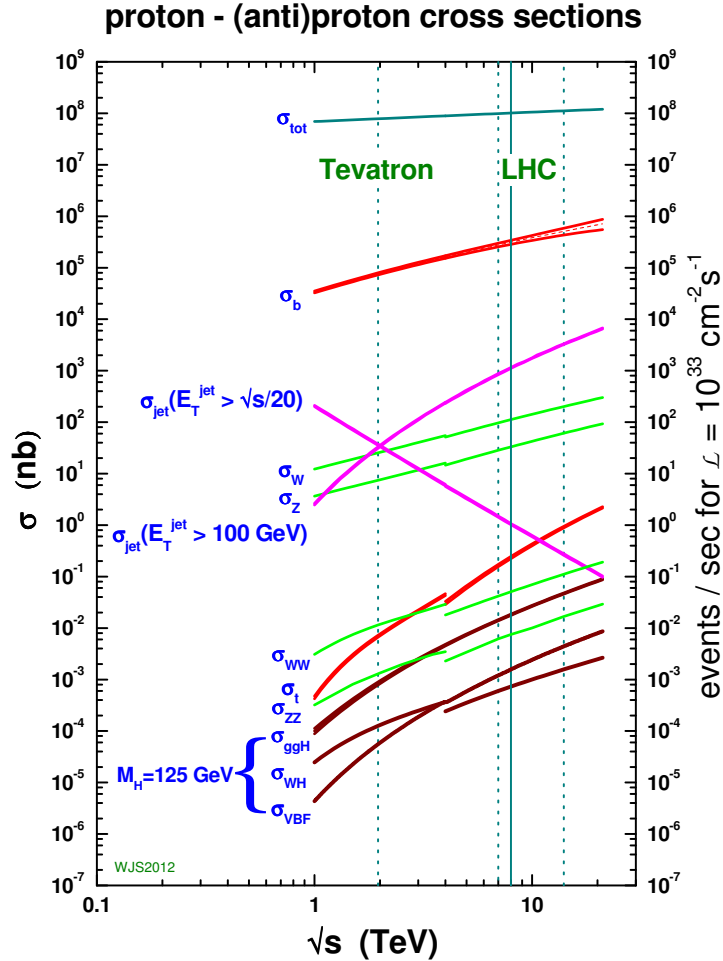


Figure 2.14: Standard Model cross sections as a function of collider energy [48]. The total hadronic cross-section is based on parametrisation of the Particle Data Group [14]. Other cross-sections are calculated at NLO or NNLO perturbative QCD, using MSTW2008 parton distributions [49].

data that can be stored every day is of the order of few Terabytes that decide the rate at which we can accept the events (~ 100 Hz). Thus, the concept of the trigger, method to select events of interest, was first introduced by ZEUS experiment [50], that handles data in real time, coupled with complex data acquisition (DAQ) system. While designing the trigger one has to keep in mind that trigger should efficiently

accept the interesting physics while rejecting the non-interesting ones as whatever information is lost at this level can not be recovered.

The CMS trigger system is divided into two steps - Level-1 trigger which is a custom hardware running synchronously with the LHC bunch crossing frequency of 40 MHz and the High-Level Trigger (HLT) [23, 51, 52]. The CMS trigger flow diagram is shown in Fig. 2.15.

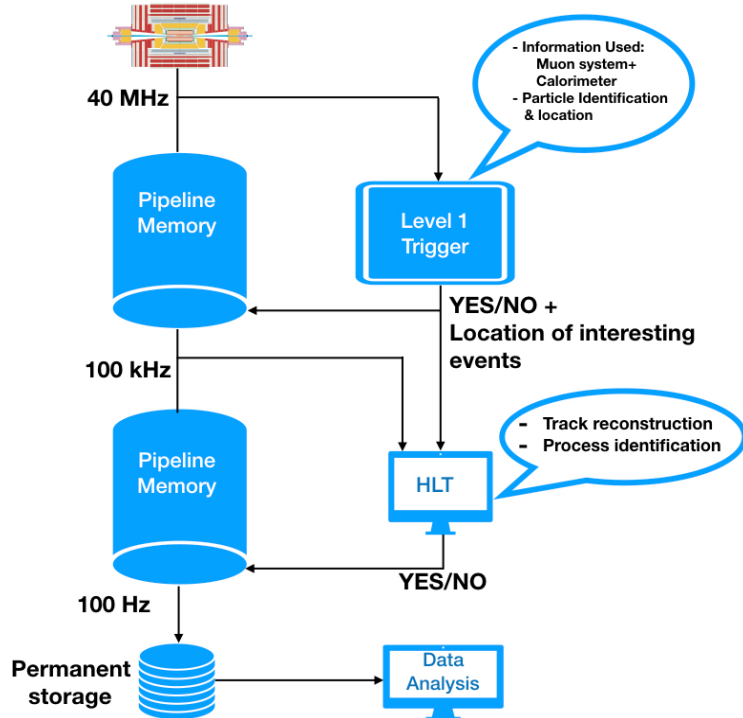


Figure 2.15: CMS trigger flow diagram that uses two level trigger. At Level 1, CMS uses information from muon system and calorimeter. Using this information it decides to reject or pass the event to the HLT farm for further processing. HLT uses fast offline reconstruction algorithm that uses information from all sub-system, i.e., calorimeters, muon system as well as tracker to decide to keep or reject the event.

Level-1 Trigger

The Level-1 trigger checks each event and decides if they can go for further scrutiny by the HLT. It analyses each event based on the coarser level granularity information of calorimeter (both ECAL and HCAL) and tracks from muon system. However, this decision cannot take place within 25 ns (i.e. before arrival of next p-p bunch

crossing), so a latency¹¹ of $3.2 \mu\text{s}$ was added, which is named as pipeline memory in Fig. 2.15. At Level-1 the event reduces rate from 40MHz to 100kHz.

The Level-1 consists of three steps. They are:

- Level-1 calorimeter trigger,
- Level-1 muon trigger,
- Level-1 global trigger

Every step at Level-1 trigger has local, regional and global components. At first the local components, which is also called Trigger Primitive Generators (TPG), are based on the energy deposit in the calorimeter trigger towers¹² and track segments or hit patterns in the muon chambers, respectively. Next, the regional trigger combines this information to identify the pattern logic and determine ranked and sorted objects such as electrons, photons, or muons. Finally, the global component determines the highest-ranked objects across the detectors and transfer it to the Level-1 global trigger. The flow diagram of Level-1 trigger is shown in Fig. 2.16.

Level-1 Calorimeter Trigger

The first step of calorimeter trigger is TPG. The TPG is the sum of transverse energy measured in ECAL crystals or HCAL readout towers to obtain trigger towers and it also attaches bunch crossing information with this. Information in the form of TPG is transferred to the Regional Calorimeter Trigger (RCT). Then the information from RCT is combined to the Global Calorimeter Trigger (GCT) where the best four candidates in each category are chosen and sent to the global trigger.

Level-1 Muon Trigger

In Level-1 muon trigger, all three muon systems, i.e. DT, CSC and RPC, take part. Considering the difference in particle flux and the magnetic field uniformity with η the muon track finding was segmented into three regions: Barrel ($|\eta| < 0.83$), Overlap ($0.83 < |\eta| < 1.24$) and Endcap ($|\eta| > 1.24$). A pattern based track finding

¹¹The latency is the time elapsed between a pp interaction and the arrival of the Level-1 trigger decision at the Front-End. The Front-End system processes and keeps all detector signals in buffer until they are delivered to the Data Acquisition System (DAQ)

¹²Trigger towers are the arrays of crystals where energy is deposited.

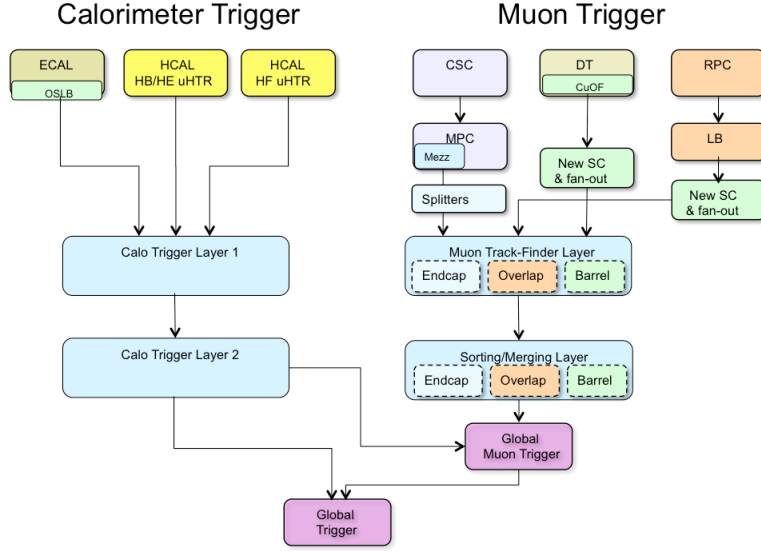


Figure 2.16: CMS Level-1 trigger flow diagram [53]. On left the hierarchy of calorimeter trigger is shown. On right the different layers of the muon trigger system is shown. Finally the global trigger combines information from both system to take the Level-1 decision.

algorithm [54] is used at endcap and overlap region. It assigns p_T to each track using the look-up-table based on multivariate techniques. In barrel region a simple extrapolation track finding algorithm is used. Finally, the Level-1 global muon trigger takes all the muons from three different muon sub-detectors regional track finders, then sorts and ranks them using their p_T value and quality.

Level-1 Global Trigger

The Level-1 global trigger takes input from Level-1 calorimeter and muon triggers. Also, it aligns them in time and decides to accept or reject an event. Additionally, a direct trigger signal is also received from the sub-detectors or the TOTEM experiment for some special purpose such as calibration. These received trigger signal to the level 1 global trigger are known as “technical triggers”.

The main part of the global trigger is known as the “Global Trigger Logic” board, where all the implemented algorithm are performed. The most basic algorithm consists of applying the transverse momentum (p_T) or the transverse energy (E_T) or the jet multiplicity which exceeding the required cut. Finally the passed events are sent

to the data acquisition event manager for further processing by HLT.

High Level Trigger

The complete information of the passed events by Level-1 trigger is sent to HLT processing farm to reduce the event rate to ~ 100 Hz. HLT algorithm runs on commercial computer that have about 16,000 CPU cores and performs fast version of offline object reconstruction using the information from all sub-detectors.

In CMS, the HLT has a modular structure, which is shown in Fig. 2.17. The

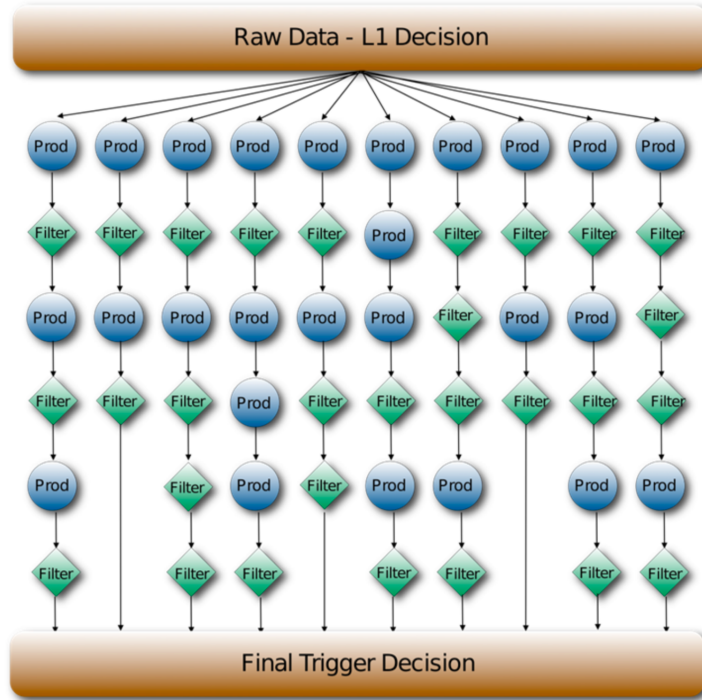


Figure 2.17: The systematic representation of HLT menu and its path[55].

HLT menu is made up of many HLT paths. There are around 400 different HLT paths in the HLT menu for the data taken during Run2. Example of several trigger paths is given in Table: 2.3. Each path consists of a sequence of reconstruction and filtering modules. The modules in each path are either object producers or filters. The producer modules reconstruct the object like electron, photon, muons, jets and their properties. Filter module take decision using the variables reconstructed by producer modules to accept or reject an event. All the producers and filters are arranged in blocks in order of their complexity, so that faster algorithm runs first and

Trigger Path	Explanation
HLT_Ele27_WPTight_Gsf_v7	Requires at least one electron at the HLT level having p_T greater than 27 GeV along with some tight selection criteria on its kinematic variables. The electron is reconstructed using the Gaussian Sum Filter (GSF) technique ¹³ .
HLT_Ele27_eta2p1_WP Loose_Gsf_v8	Requires at least one electron at the HLT level having p_T greater than 27 GeV and passing a loose selection criteria. In addition to this electron should be within a pseudo-rapidity region of 2.1.
HLT_Ele27_eta2p1_WPTight_Gsf_v8	This is similar to the previous trigger except that here a tight working point is applied to select electrons at the HLT level instead of the loose one.
HLT_IsoMu24_v	Requires at least one isolated muon at the HLT level having p_T greater than 24 GeV.
HLT_IsoTkMu24_v	Requires at least one isolated muon at the HLT with p_T greater than 24 GeV. Here the muon signature should be matched to the muon hits registered in the tracker.

Table 2.3: Examples of some of the electron and muons HLT trigger paths with their description used during data taken in 2016.

their products are filtered. If a filter fails the rest of path skips. At last the final decision is the logical OR of all the HLT menu decisions.

All the events that pass HLT path are stored in local disk (in CMS its Tier 0¹⁴)

2.4.4 CMS Offline Computing

Once the events are selected by the trigger system and data are stored to disk, they are ready to be analysed offline but before that, the raw data need to be processed,

¹³In CMS detector we use large amount of material that includes detector itself along with the on detector electronics, mechanical support and power cooling. Thus along with the ionization energy loss and multiple coulomb scattering it also suffers from energy loss due to bremsstrahlung. Thus, to precisely model the track, we have to include the material effects. This is done using the linear generalization of Kalman Filter[56], the GSF[57, 58] in the track reconstruction. It assumes all the different components of different degrees of the bremsstrahlung under consideration as the sum of several Gaussian mixtures [59].

¹⁴The Worldwide LHC Computing Grid (WLCG) is composed of four levels, or “Tiers”, identified with numbers 0, 1, 2 and 3. Each Tier is made up of several computer centres and provides a specific set of services; they process, store and analyse all the data from the LHC. Tier 0 is the CERN Data Centre. The whole data from the LHC pass through this central hub. Tier 0 distributes the raw data and the reconstructed output to Tier 1’s, and reprocesses data when the LHC is not running.

i.e., to convert data into understandable physics objects like electrons, muons, photons, jets, and so on. This step is known as object reconstruction and it is the most CPU intensive task in the data processing chain of CMS. In this step one needs to reconstruct the primary vertices, charged particle tracks, identify electrons, photons, muons, reconstruct jets, apply b-tagging algorithm to reconstruct b-jets, run detector specific filtering and so on. To perform all these steps CMS collaboration had developed its software which is known as CMSSW. This software is based on Event Data Model (EDM) centred around the concept of an event. Here, an event is a C++ object container for all raw and reconstructed data related to a particular collision. Finally, these events are stored in ROOT files [60]. The CMSSW event processing model consists of one executable called cmsRun, and many plug-in modules. These modules contain all the necessary programs needed for event processing such as detector calibration and reconstruction algorithms [61]. To analyse data, we also need MC simulations which are carried out based on the predictions of SM and various new physics models. MC events are generated at parton level using various monte-carlo generators like MadGraph or Pythia followed by showering and hadronization. These events are then passed through the GEANT4 [62] for CMS detector simulation. The resultant data is similar to what one obtains from the actual detector.

3

Gas Electron Multiplier

“New directions in science are launched by new tools much more often than by new concepts.”

– Freeman Dyson

In this chapter, the GEM detectors are introduced, which is proposed for the upgrade of the CMS muon system during the long shutdown-2. The functionality of these GEM detectors were scrutinized during beam test campaigns carried out at the CERN SPS beam test facility. The first half of this chapter deals with the measurements performed on prototypes of CMS GEM detectors using the data collected during different beam tests. University of Delhi in collaboration with other Indian institutes actively participated in these beam test campaigns and data analysis for GEM detectors. The characterisation of GEM foils developed in India for the CMS upgrade is described in the later part of the chapter.

3.1 Introduction

The invention of Multi-Wire Proportional Chamber (MWPC) in 1968 by Georges Charpak was one of the major breakthroughs in the development of gaseous detectors since it had better rate capability vis-a-vis its predecessors [63]. This invention also led to a Nobel prize for George Charpak in 1992. The design and performance of MWPC have improved progressively through all these years. However, because of our increasing demands for acquiring knowledge about particle detection, MWPC reached its limitation in terms of the maximum rate capability and detector granularity. In

1988, Anton Oed invented the Micro-Strip Gas Counter (MSGC) which had a position resolution of few tens of microns and could overcome the rate limitation arising due to positive-ion accumulation in the gas volume. Also, it could sustain a particle flux greater than few MHz/mm^2 . Although, these kinds of detectors performed efficiently, however, the long-term studies revealed following shortcomings:

1. Accumulation of ions on the electrodes, which affects the gain and life of the detector.
2. In some cases, the passage of highly ionising particles could lead to a destructive discharge in the detector medium.

These drawbacks of the MSGC led to the development of Micro-Pattern Gaseous Detectors (MPGD). This class of detectors, specifically the Gas Electron Multiplier (GEM) [64, 65, 66], could provide an unprecedented spatial resolution, larger sensitive/detection area, with higher rate capability and good operational stability over the longer operating periods. Several new studies also revealed that under certain circumstances these detectors might be less vulnerable to the radiation-induced ageing than the standard silicon microstrip detectors [67, 68].

Because of their efficient detection qualities and high rate capabilities, GEM detectors have already been used in various experiments like COMPASS [69], TOTEM [70], LHCb [71]. Recently, these detectors are also proposed for the CMS muon detector system upgrade. A brief description of the working principle and properties of the GEM detectors is provided in the following sections.

3.2 Design and working principle of GEM detector

GEM is a relatively new concept introduced by Fabio Sauli [64] at CERN, which consists of a thin polyimide sheet (usually a thin Kapton foil¹ [72] with thickness 50 μm) coated with thin layer metal (usually copper) on its both sides. It is chemically pierced with a uniform array of holes using the photolithography and acid etching processes [73], as shown in Fig. 3.1 (left).

¹Kapton was chosen as the insulating layer as it can sustain very high radiation as well as it works with the wide range of the temperature. It is a plastic polyamide, created by DuPont.

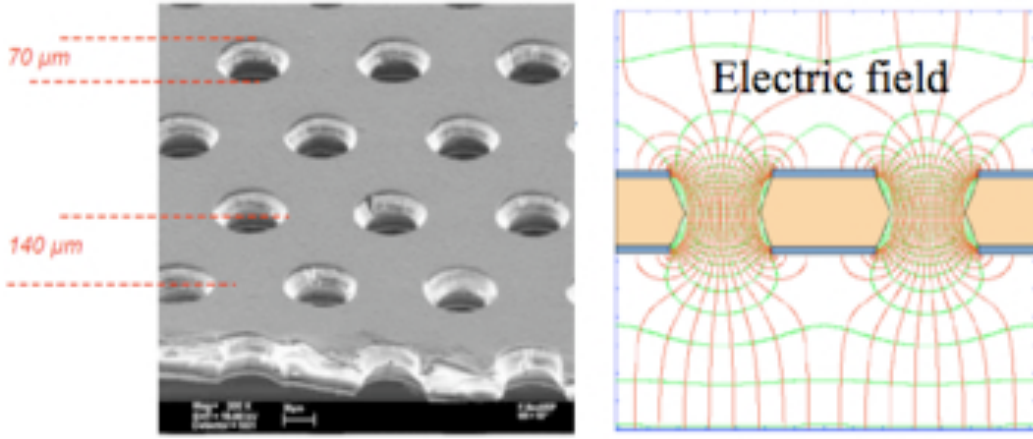


Figure 3.1: Cross-sectional view of a GEM foil etched with holes (left). The strong electric field generated in the vicinity and inside the holes after the application of potential difference across the GEM foil (right).

A potential difference is applied between the two copper layers which create a high electric field inside the holes (Fig. 3.1) and is given as:

$$E = \frac{V}{d} , \quad (3.1)$$

where E is the electric field inside a hole in the GEM foil, V is the voltage applied between the two copper layers and d is the thickness of the GEM foil.

To illustrate the working of a GEM detector, the active detector medium could be divided into three different regions: drift, amplification and induction regions, as shown in Fig. 3.2. The passage of a charged particle leads to ionization in the drift region, and the generated primary electrons drift towards the amplification region (i.e., through GEM holes). The electrons gain kinetic energy from the intense electric field inside the holes which is sufficient to produce secondary ionizations, eventually, leading to an avalanche multiplication. Finally, in the induction region, all the electrons from the amplification regions are collected on the readout plane.

To avoid the problem of electrical breakdown, several GEM foils operating at lower voltages could be stacked together in between the drift cathode and the readout board. For such detector configurations, the transfer region takes almost all the electrons from one GEM foil to another. In view of the fact that the total gain of a detector

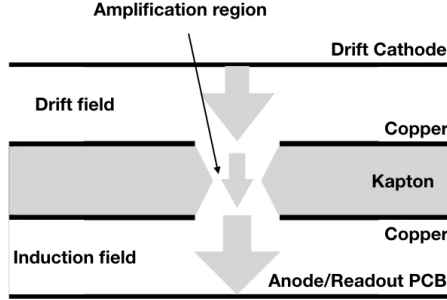


Figure 3.2: Outline of a single GEM detector.

is given as the product of the individual gain of each foil, gains up to an order of 10^5 can be achieved in this way. Besides, in this configuration, the detector can reach its maximum gain without any or with the least probability of electric discharge.

The gain and discharge probability are compared for the single, double and triple-layered GEM detectors as shown in Fig. 3.3, which clearly indicates that the triple GEM detectors can achieve a gain beyond 10^4 without any electrical discharge. Also, the signal readout by the electrode is pretty fast as it uses only electrons to generate a signal. Multi-layered boards could also be used to achieve a two-dimensional readout from these detectors.

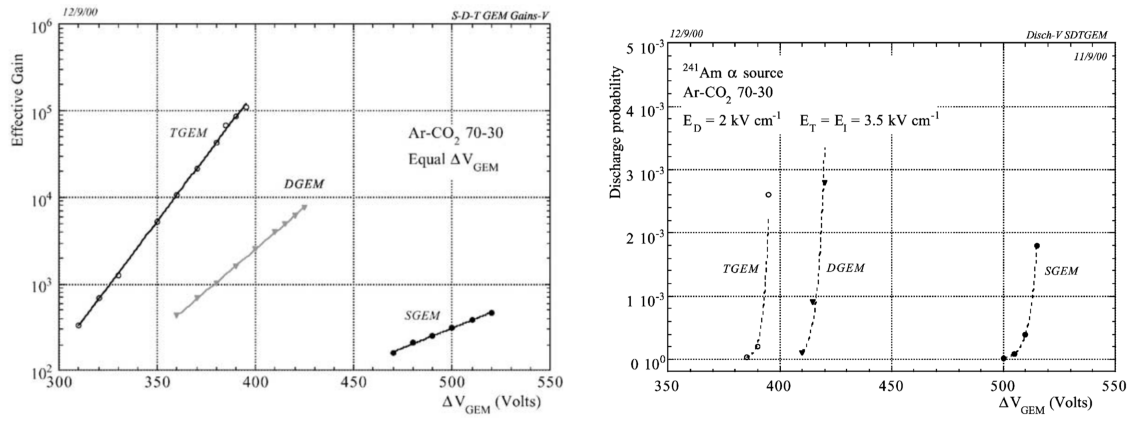


Figure 3.3: Comparison of total effective gain on anode as a function of applied voltage for single, double and triple layered GEM detectors (left). The discharge probability as a function of applied voltage is shown for the single, double and triple layered GEM detectors (right) [74].

A detector arrangement where three GEM foils are stacked together is known as a “***Triple-GEM detector***”, as shown in Fig. 3.4. Such a detector configuration is proposed for the CMS Phase-II upgrade and is discussed in the following section.

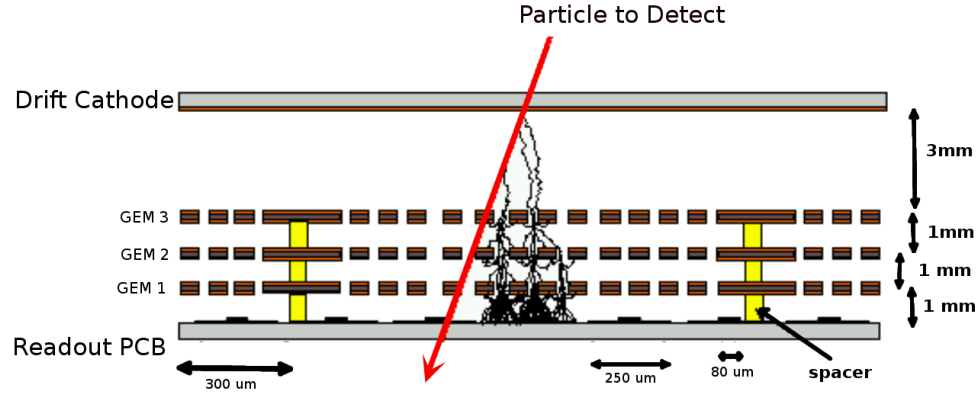


Figure 3.4: The working mechanism of a GEM detector.

3.3 GEM for the CMS Phase-II Upgrade

As mentioned out in Sec. 2.4.2, the CMS Collaboration has finalised to install GEM detectors in the pseudo-rapidity region $1.6 < |\eta| < 2.2$ of the CMS detector. These detectors will support the existing CSC muon sub-system to improve the muon triggering and tracking capabilities in the forward region [26]. The combined operation of CSC and GEM detectors will lead to a precise measurement of the muon bending angle at the trigger level, thus strongly reducing muon mis-reconstruction rate.

This CMS muon detector system upgrade is carried out to achieve the following goals:

- Re-establish the redundancy in the forward region beyond $\eta = 1.6$
- Improve the muon tracking performance during the high-luminosity LHC operation.

The installation of GEM detectors is proposed during the period of Long Shutdown-2 (2019-2020). The upgrade project is named as CMS GE1/1 upgrade, where the letter “G” stands for GEM, “E” stands for End-cap, the first “1” corresponds to the

first muon station and the second “1” corresponds to the first ring of the station. Analogously, the GEM detectors to be installed in the CMS detector are referred to as GE1/1 detectors. The detectors will be inserted in front of the ME1/1 station and into the slots originally foreseen for the RPC detectors, as shown in Fig. 3.5. The design and operational parameter of CMS GE1/1 detectors are described in the following subsections.

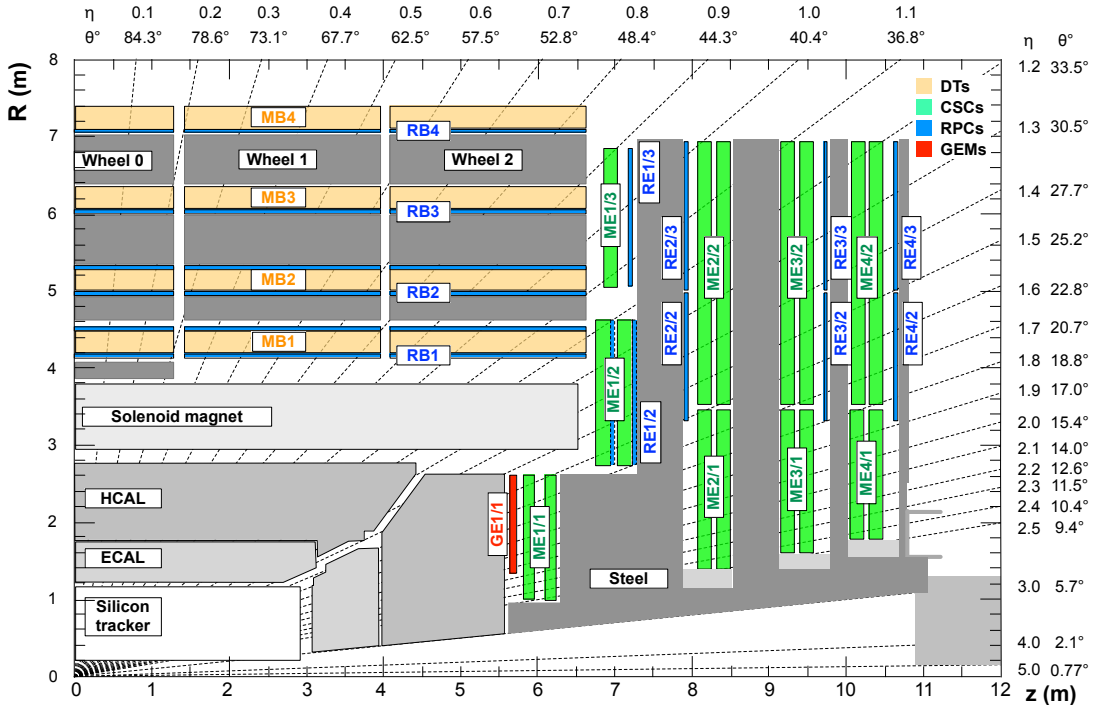


Figure 3.5: Cross-sectional view of the CMS quadrant highlighting the proposed location of GEM detectors (red).

3.3.1 CMS GE1/1 Detector Specification

A typical GE1/1 detector is trapezoidal in shape with an active area of $990 \times (220 - 445) \text{ mm}^2$. The shape and size of the detector was decided based on the geometry of vacant high- η region in the CMS muon endcaps. A GE1/1 chamber consists of a Triple-GEM detector having a 3/1/2/1 mm (drift/transfer 1/transfer 2/induction) electrode gap configuration, as shown in Fig. 3.6.

Each CMS GE1/1 detectors uses a thin Kapton foil ($50 \mu\text{m}$ thick) with a copper cladded ($5 \mu\text{m}$) on its both sides. The detector readout board is divided into eight

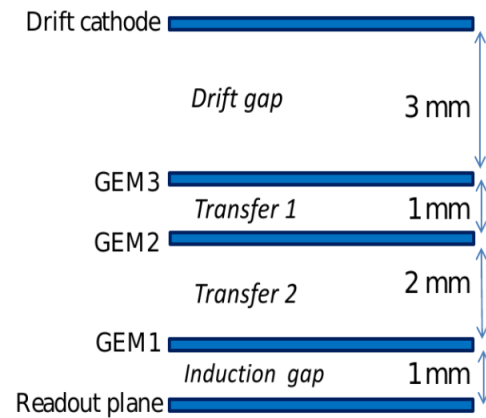


Figure 3.6: The layout of different GEM layers inside a CMS GE1/1 detector.

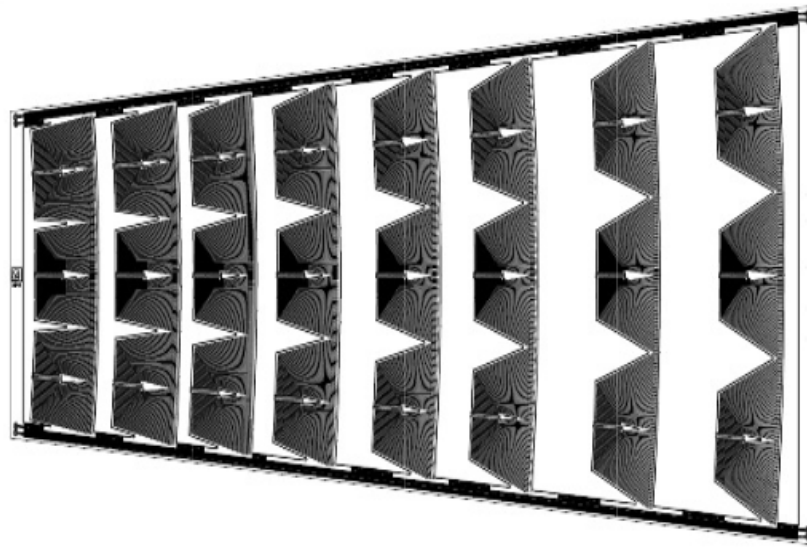


Figure 3.7: Drawing of a large trapezoidal CMS GEM chamber showing $8 - \eta$ and $3 - \phi$ par partitions.

η -partitions with 384 strips. Each strip is radially oriented along the long side of the detector with a pitch varying from 0.6 mm (short side) to 1.2 mm (long side). Each partition is subdivided along the ϕ -coordinate into three readout sectors with 128 strips or channels per sector. The η partition and ϕ portions of the GEM detector are shown in Fig. 3.7. To improve the muon tracking capabilities, two GEM chambers will be mounted face-to-face to form a double layer called “*Super-Chamber*”. Thus each Super-Chamber will provide two impact points for each muon track which can be ORed together to generate the final muon hits. The full layer by layer mechanical design of a GEM chamber is shown in Fig. 3.8. The main parts of a GEM detector are its foil, drift plane, readout board, shielding and high voltage divider. Before being installed into the CMS detector, the working and various operational parameter of CMSge1/1 detectors were deeply scrutinized during several beam test campaigns. A detailed study and results obtained during two of such beam tests is given in the following section.

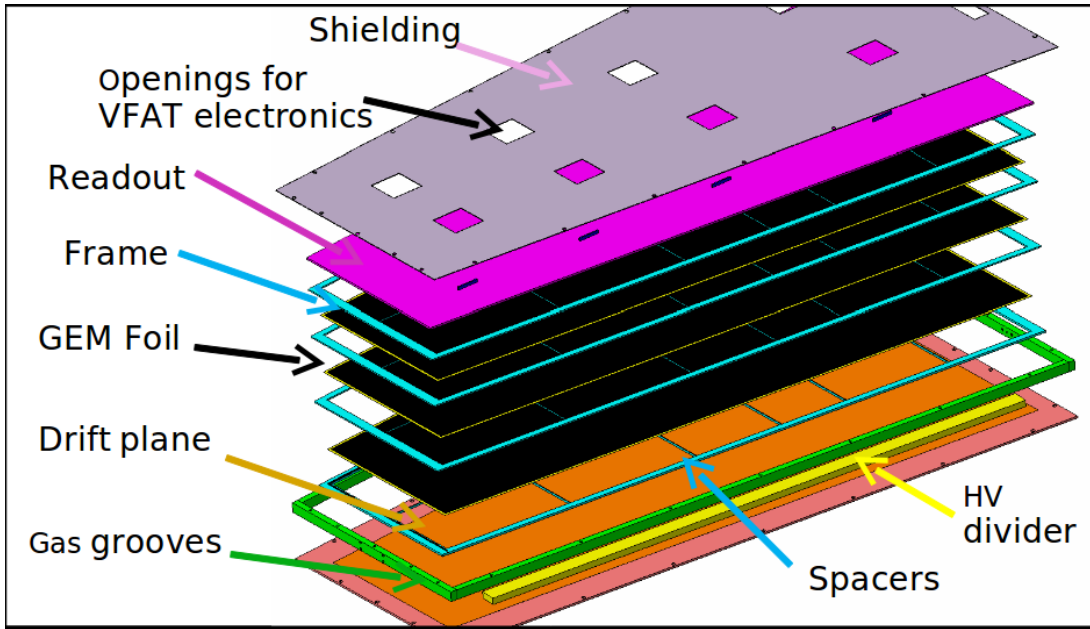


Figure 3.8: Layer by layer view of CMS GE1/1 detector

GE1/1 Generations

From 2010 till now total of five different GE11 versions are developed and tested every year. Based on the experience every new generation was improved from its previous

versions [75]. All the generations are listed in Fig. 3.9.

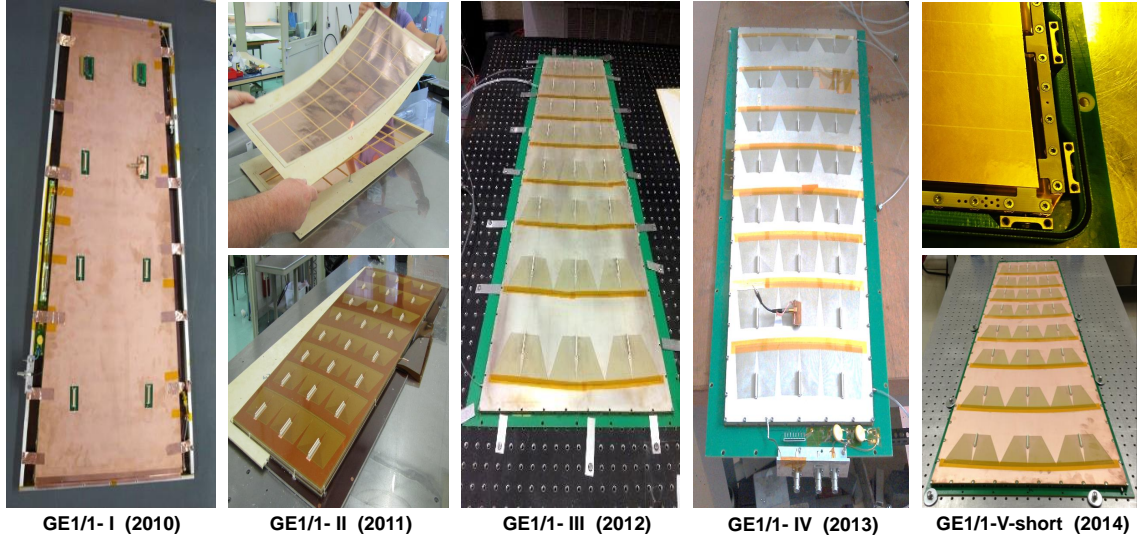


Figure 3.9: Five different generations of GE11 detector developed and improved with time.

In the first version of GE11, GE11-I, prototype was build 1m-class GEM detector and operated. In this detector different components are glued together and to have gaps between different GEMs spacer ribs were used to have the gap configurations 3/2/2/2 mm. In this version total 8 readout sector was there [76].

In the next version, GE11-II, the readout sectors were increased from 8 to 24 which are arranged as 8- η partitions and 3- ϕ partition (columns). Here, each η partitions had 384 radial strips with 455 μrad angular pitch. Also, to speed up the signal, the foil gap configurations are changed to 3/1/2/1 mm [77].

In the third version of GE11, known as GE11-III. In this version it was split into several pieces and used the mechanical stretching during the assembly then glued to the frame and drift board [78].

In the fourth version of GE11, GE11-IV, the major achievement was to abandoned the use of glue while assembling the detector. Because of this the stretching improved and the board deformation issue was resolved as compared to the GE11-III. Still it takes few hour in assembling and need to use the pre-bending of the with respect to the bowing observed. Thus, it was not reliable for the mass production [79].

The pre-bending issue is resolved in the GE11-V prototype by tensioning the foil against the independent “*pull-out*” pieces. This version is opted for the final production of the GE11 chamber for installation in the CMS during Long-Shut-down-2.

3.3.2 GE1/1 Beam Test Studies

The GE1/1 detector was tested using 150 GeV muon and pion beams at CERN SPS beam test facility during October-December 2014.

The goal of the beam test campaign was to measure the efficiency, space & time resolution, and the cluster size of the CMS GEM detector. The detectors that were tested included GE11_IV and GE11_IV_GIF detectors. Both GE11_IV and GE1/1_IV_GIF are generation IV GE1/1 detectors but GE1/1_IV_GIF was irradiated with the γ -ray at the CERN gamma-ray irradiation facility² for an year to perform ageing studies [80]. Also, several important parameters like electric field, voltage across each GEM foil, the rate and gain were measured and are discussed in appendix ??.

Two beam test campaign were carried out during October-December 2014. These campaigns were held in H2 and H4 beam test area of the CERN SPS. The H2 beam test was carried out from 6th October 2014 to 27th October 2014 while the H4 beam test was held from 26 November to 14 December 2014. The main goal of the H2 beam test was to test the two detectors mentioned above with $Ar : CO_2$ gas mixture while in H4 beam test the same detectors were tested with $Ar : CO_2 : CF_4$ gas mixture. Initially, the plan was to scan each sector of the GEM detector but due to timing constraints we were just able to scan sector $(i\eta, i\phi) = \{(5, 2)\}$ and $(i\eta, i\phi) = \{(1, 2), (5, 2), (8, 2)\}$ during H2 and H4 beam tests respectively.

The data collected during these beam test campaigns were grouped into different run names, based on the electronic setup and gas mixtures used during the data taking. Out of these four sets of run ranges were marked as “*good*”, based on certain data quality checks, for further analysis. These run ranges along with their specification are listed in Table 3.1.

²The GIF bunker contains a ^{137}Cs source of 566 GBq. This emits gamma rays of 662 keV. The detector was placed 30 cm from the source where the particle rate was of the order of 100 kHz/cm^2 . This allowed accumulating the charge in twelve months which would be equivalent to the 10-year operation of GEM detector in LHC environment [80].

³1 VFAT unit = 0.08 fC

Run Name	Details
2014H2C	Run range: 306-407 Threshold for each VFAT strip = 15 VFAT units ³ = 1.2fC Asynchronous mode with respect to the LHC clock sector scanned ($i\eta, i\phi$) = (5, 2) Gas mixture used: Ar : CO ₂ =(70:30)
2014H4A	Run range: 1592-1646 Threshold for each VFAT strip = 15 VFAT units = 1.2fC Asynchronous mode with respect to the LHC clock sector scanned ($i\eta, i\phi$) = (5, 2) Gas mixture used: Ar : CO ₂ : CF ₄ =(40:15:45)
2014H4C	Run range: 1868-1906 Threshold for each VFAT strip = 15 VFAT units = 1.2fC Asynchronous mode with respect to the LHC clock sector scanned ($i\eta, i\phi$) = (8, 2) Gas mixture used: Ar : CO ₂ : CF ₄ =(40:15:45)
2014H4D	Run range: 2065-2123 Threshold for each VFAT strip = 15 VFAT units = 1.2fC Asynchronous mode with respect to the LHC clock sector scanned ($i\eta, i\phi$) = (1, 2) Gas mixture used: Ar : CO ₂ : CF ₄ =(40:15:45)

Table 3.1: List of golden runs selected to measure the GE1/1 properties.

Readout Electronics

Front-end electronics used in the beam test was **VFAT2** chips [81, 70]. The upgraded version of the same chip, known as VFAT3, will be used with GE1/1 detectors for Level-1 muon triggering [82]. Its block diagram is shown in Fig. 3.10. VFAT is a front-end Application Specific Integrated Circuit (ASIC) chip. It was primarily designed for the sensors readout in the TOTEM experiment at CERN. VFAT chip is used for both triggering and tracking purpose. For triggering it uses the programmable “*fast OR*” information based on a hit in the detector. It provides a monostable output for the programmed number of channels in a single clock cycle which is referred to as “*S-Bit*”. While, for tracking it provides the step-wise spatial information strip-wise for every triggered event.

VFAT2 has 128 analog input channels, very low noise pre-amplifier, shaper and comparator attached to it. Signal discrimination is done based on the programmable threshold setting and then stored within SRAM⁴ until the trigger information is

⁴Static random-access memory (static RAM or SRAM) is a type of semiconductor memory that uses bistable latching circuitry (flip-flop) to store each bit. SRAM exhibits data remembrance but it is still volatile in the conventional sense that data is eventually lost when the memory is not powered.

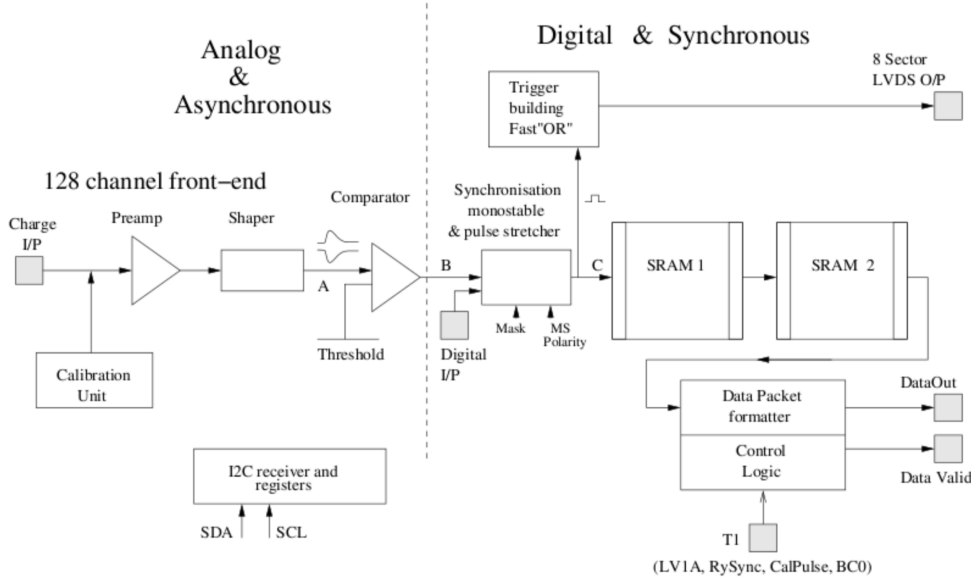


Figure 3.10: Block diagram of the VFAT2 chip showing signal flow [81].

received. It can apply positive as well as a negative threshold value to each channel independently. This feature is named as “*TrimDAC*” and it has two programmable voltages V_{T1} and V_{T2} and the threshold is defined as the difference between these two programmable voltages, i.e., $V_{TH} = V_{T2} - V_{T1}$. VFAT chip also provides the facility to mask individual noisy channels. To synchronize the output of the comparator the monostable block provides 1 clock pulse for each threshold-crossing signal.

Latency is a measure of time at which VFAT2 will read the signal. Technically, for a given trigger, it is defined as the number of SRAM locations the chip has to go back in order to read the digital output of the event corresponding to that trigger. It is measured in terms of clock cycles.

TURBO Readout Board

Once the data is recorded by the VFAT chips, it has to be extracted for further analysis. This is done by using TURBO which is a standalone DAQ system for the VFAT front-end ASIC [83]. It was developed for testing TOTEM hybrid equipped with VFAT chips. TURBO board is portable and capable to provide a real time

response for small and medium-sized experiment. Each TURBO can accommodate up to 8 VFAT chips. A systematic diagram of TURBO board is shown in Fig. 3.11. But,

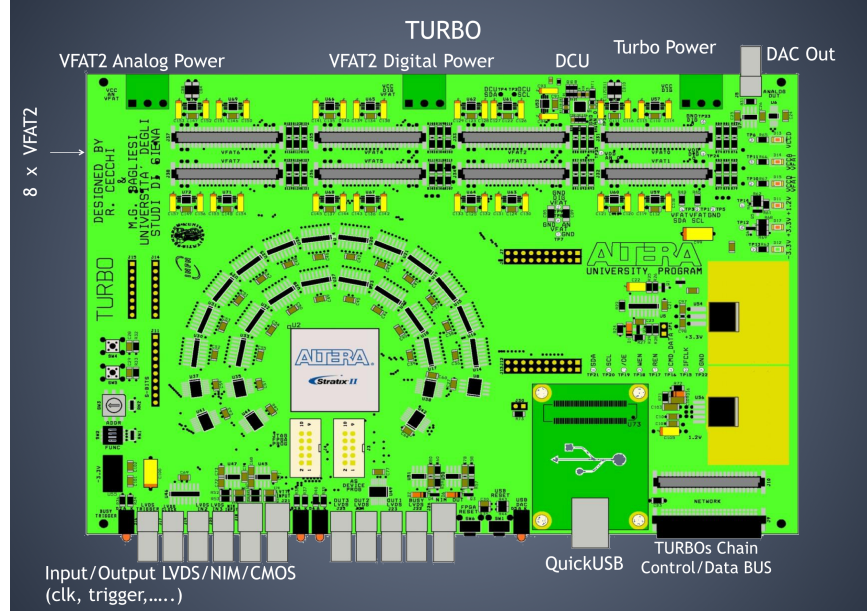


Figure 3.11: TURBO board [83].

one can use more than 1 TURBO boards to accommodate more than 8 VFAT chips. Out of them, one TURBO board will act as the master board that will take care of the clock for other TURBO boards, which act as slaves. A LabView program can be used to control TURBO boards remotely. This program can perform standard threshold and latency calibration scans. Further, it can also be used for data acquisition and to perform quality control tests.

Measurement Mode

Data can be collected in two different modes: synchronous mode and asynchronous mode. In the asynchronous mode, triggers are not correlated with the clock while in a synchronous mode triggers are correlated with the leading edge of the LHC 40 MHz clock. Synchronous mode is used to collect data in sync with the LHC clock.

Detector Details Under Beam Test

In lab at CERN several parameters of the tested GE1/1 detectors are measured. They are - electric field, voltage across each GEM foil, gain and rate for both GE1/1, i.e.,

GE11_IV and GE11_IV_GIF.

The high voltage configuration used during the beam test is shown in Fig. 3.12.

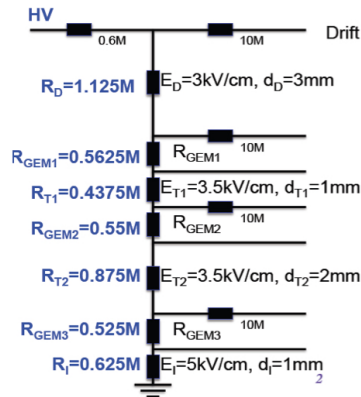


Figure 3.12: High voltage divider configuration as used in the 2014 beam test campaign.

Also, the voltage across the GEM foils and the electric field with respect to the current in the voltage divider is shown in Fig. 3.13.

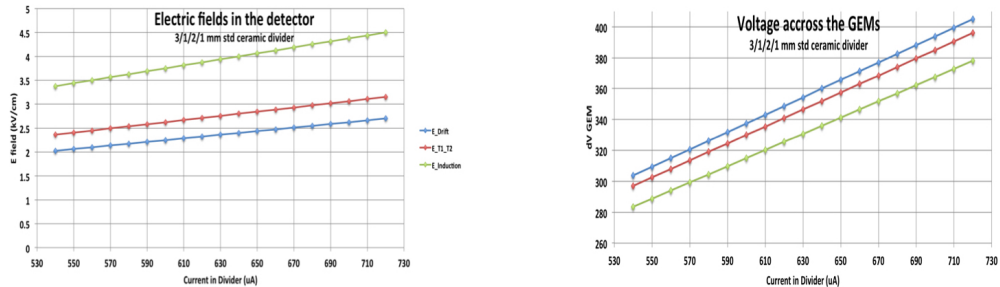


Figure 3.13: Electric field (left) and voltage across each GEM foil (right) for the tested GE1/1 detector.

The gain of the detector was measured in the lab using an X-ray source for both

$Ar : CO_2$ and $Ar : CO_2 : CF_4$ gas mixture and is shown in Fig. 3.14 and 3.15.

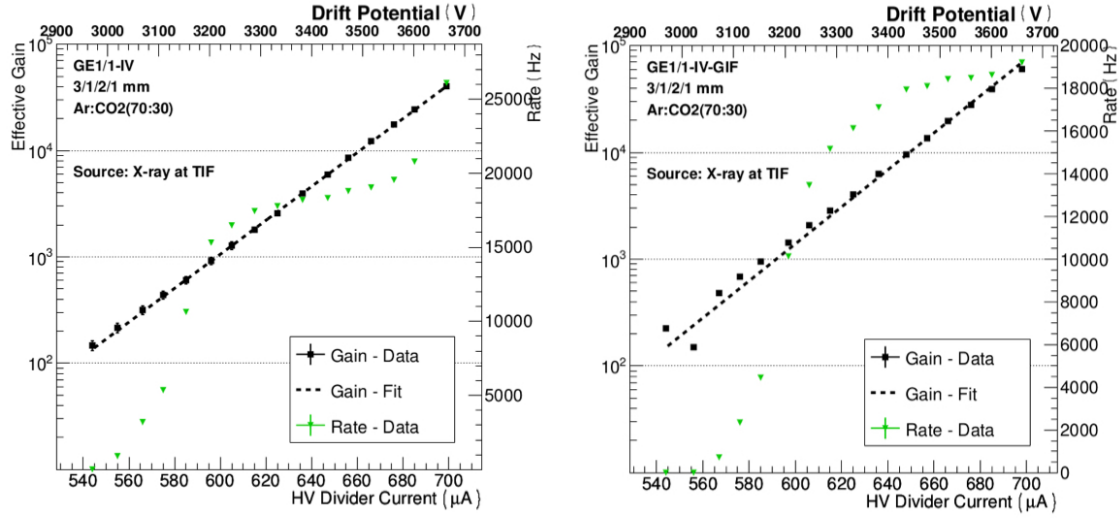


Figure 3.14: Gain and rate variation for $Ar : CO_2$ (70:30) with respect to the current supplied to the high voltage divider for GE1/1-IV (left) and GE1/1-IV-GIF (right).

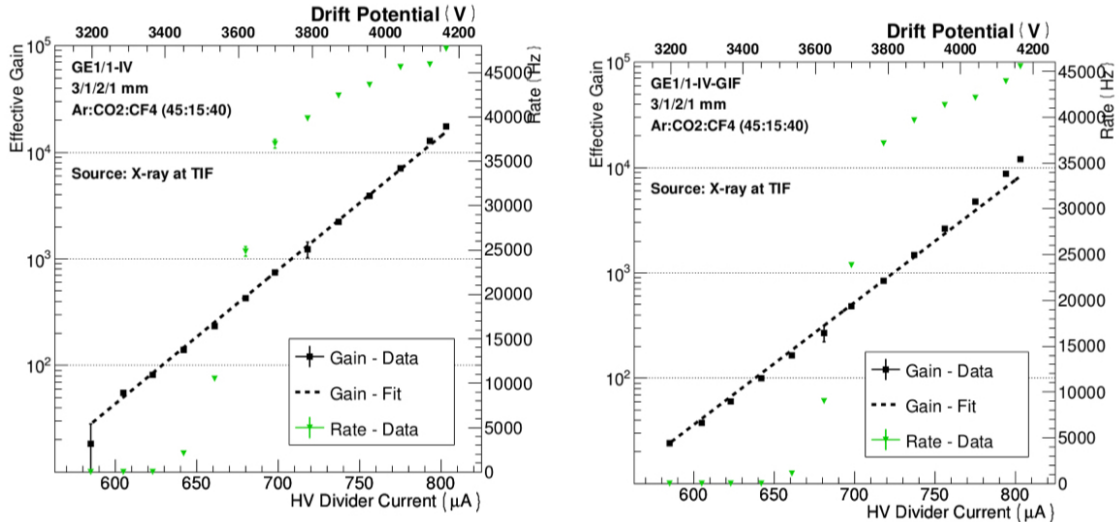


Figure 3.15: Gain and rate variation for $Ar : CO_2 : CF_4$ (45:15:40) with respect to the current supplied to the high voltage divider for GE1/1-IV (left) and GE1/1-IV-GIF (right).

The gain of a detector was calculated using the ratio of output to the input value of current, like:

$$Gain = \frac{I_{out}}{q \times f}, \quad (3.2)$$

where q is the charge collected at the first layer of GEM foil and is calculated as:

$$q = n \times e , \quad (3.3)$$

where e is the electron charge, n is the average number of electrons produced in the drift region by the incident particles and f is the interaction rate of the incident particles in the gas. For the given X-ray source with a specific energy and the known ionization potential of the used gas mixture n can be calculated and in our case it is found to be $n \sim 290$.

3.3.3 Beam Test Experimental Set-up

The experimental set-up consists of three plastic organic scintillators, three trackers and a GE1/1 prototype, being flushed with an Ar/CO₂ (70:30) gas mixture. The trackers are triple-GEM detectors with an active area of 10 cm × 10 cm having 256 strips in both horizontal (y-coordinate) and vertical (x-coordinate) directions with respect to the beam and a pitch of 0.4 mm. The three trackers constitute a muon tracking telescope which is used to reconstruct the beam trajectories and reduces background events. Figure 3.16 shows the experimental set-up used to perform beam test studies. The GE1/1 prototypes are installed on a movable table to scan different sectors. At a time only one (η, ϕ) sector of GEM detector is irradiated with the beam. The CMS GE1/1 prototype test chamber was placed, close to the tracking hodoscope, on a vertically movable support to allow scanning. The scanned sectors of the GE1/1 detector are shown in Fig. 3.18.

The tracking telescope is equipped with the digital chips VFAT2 [84], which provides a binary output with a variable latency for the position information and a fixed latency output for the timing information.

On detector electronics connects the output from the front-end ASIC (VFAT2) to the GEM readout board. The VFAT2 chip is connected to the hybrids which are plugged into the connectors on the readout board. The analog pulses from the three scintillators, named S1, S2 and S3 are fed into discriminator for analog to digital conversion. The discriminator output was provided into the logic and coincidence (to generate event trigger) before being sent to the other DAQ systems (Figure. 3.17).

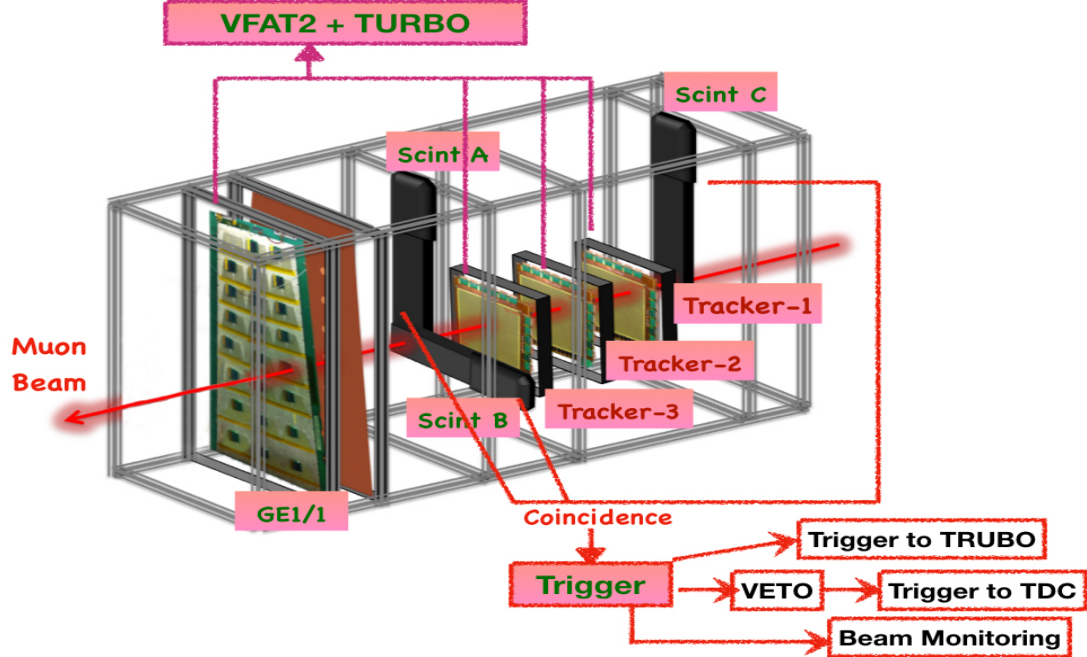


Figure 3.16: Schematic view of the beam test set-up with the three tracking GEM detectors and a GE1/1 prototype.

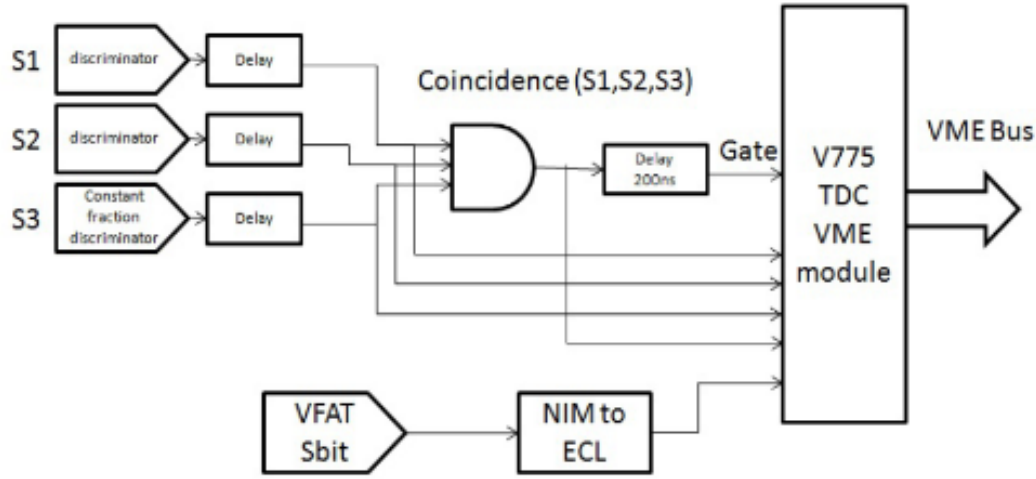


Figure 3.17: Perspective view of the experimental set-up used for performance measurement in the beam test studies. The trigger system is generated using the signal collected from three scintillators connected in coincidence unit.

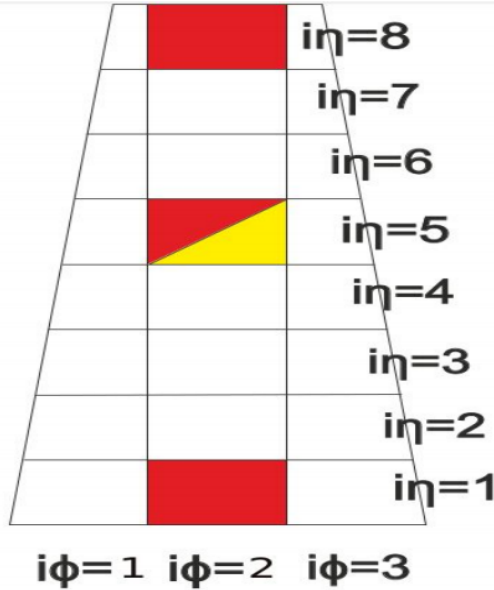


Figure 3.18: Different $(i\eta, i\phi)$ sectors of a full-size GE1/1 detector prototype. The red and yellow colour shows which sector of GE1/1 is exposed to the beam. Red sectors are collected with $Ar/CO_2/CF_4$ (45/15/40) gas mixture while the yellow sectors are taken with Ar/CO_2 (70/30) gas mixture.

3.3.4 Data Analysis

The raw data collected during these beam test campaigns were in the binary format. First, the raw data (binary information) are converted into the standard ROOT data format, which are analyzed using the “**TURBO-SOFTWARE**” [85] package. The output from the TURBO-SOFTWARE data analysis consists of hit informations for every strip from the detector, which are further used to reconstruct the particle tracks and clusters. A valid **hit** is defined when one or more strip of the VFAT chips surpass the threshold set on the readout chip. A **cluster** is defined as the number of adjacent fired strips along x or y-axis. The hit profile and beam profile recorded in the tracker for one of the runs are shown in Fig. 3.19 and 3.20.

From both hit profile and beam profile, one can see that the beam is point beam like a beam having a Gaussian spread, centred around (50,50), i.e., at the centre of the tracker.

The first step towards the track and cluster reconstruction is to discriminate the background tracks coming from detector noise (fake tracks) from the signal (muon) tracks. Once the fake tracks are removed from the collection, valid hits are used to

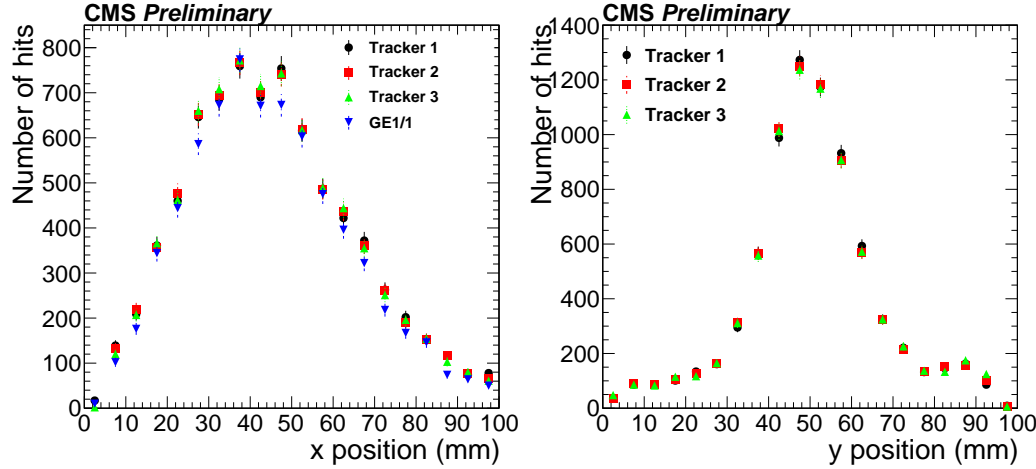


Figure 3.19: Tracker hit distribution along x and y axis and GE1/1 hit distribution along y. This is plotted from one of the runs taken during test-beam.

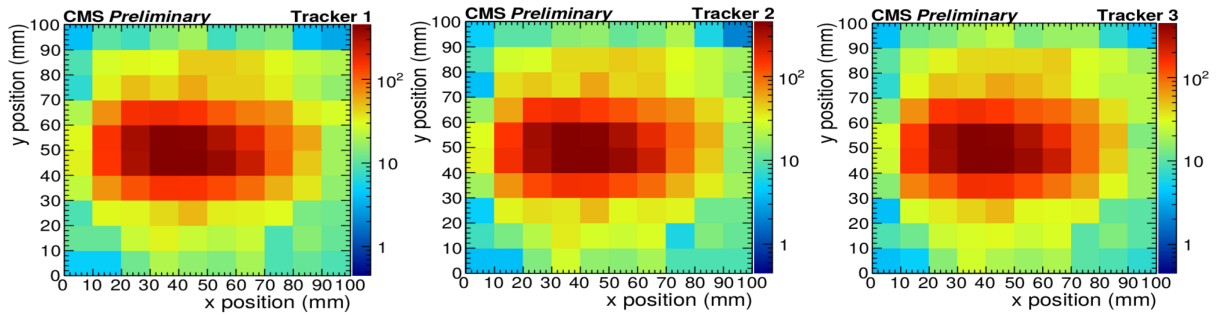


Figure 3.20: 2D- beam profile plot for the first, second and third tracker. The X and Y axis of the plots correspond to the distance (in mm) measured from the central position of the trackers in X and Y direction respectively. The different colours in the colour palette correspond to the number of hits registered in the detector at a particular (x,y) position.

generate tracks.

This sorting is done by selecting events having only one cluster in each tracker. The cluster positions are fitted using a polynomial fit of order one and χ^2 of the fit is recorded. The event is discarded if the χ^2 of the fit is greater than 10.

Detector alignment studies

Detector alignment is one of the core parts of the data analysis. For the efficient track reconstruction and for good tracking efficiency, it is necessary to align the detectors. In general, the detector is aligned manually, however, for precise alignment is achieved by incorporating the software method.

The technique used for this purpose consists of the interposition along the trajectory of several detector planes where the particles pass through; from the interpolation of all these points can be reconstructed the trajectories followed by the particles. In these environments one of the most important figures of merit of the detectors is the spatial resolution, that is the capability to reconstruct the crossing point of the particle. The goal is to reduce the χ^2 of the track fits in order to improve track and quality eliminating or reducing bias in the detector data.

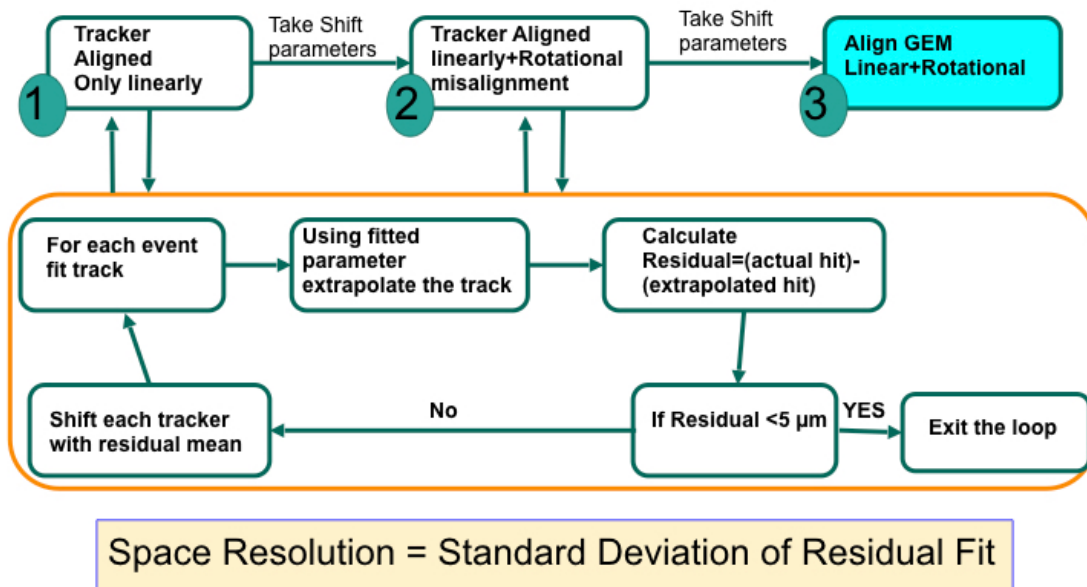


Figure 3.21: Flowchart illustrating the workflow of detector alignment algorithm.

Linear and Rotational Alignment

To measure the spatial resolution of GE1/1 detectors, these detectors aligned with respect to the tracker system. This starts with the need to be mutual alignment of the three tracking detectors that have 2D readout in the Cartesian coordinate system. The first alignment step is to shift each of the three tracking detectors iteratively in the xy-plane to make their origins coincide in the same line of sight. The initial shift parameters are the mean values from the position distributions of x and y axis. During each iteration, a linear fit is performed to the hits position along x and y direction from each tracker. Residuals are histogrammed for every detector and their distributions are fitted with a double-Gaussian function. Ten percent of the residual mean value of each detector is taken as the shift parameter in the next iteration to avoid overcorrection. This step is repeated until the resulting residual mean value converge towards zero. This method provides a first coarse alignment. In the second alignment step, we correct also for relative rotations of the tracking detectors around the beam axis in the xy-plane. We again fit straight lines to the hits in x and y direction and iterate through a succession of offsets and rotations around the beam axis relative to the first tracking detector. Again this process is repeated until the residual means from the trackers are very close to zero and χ^2 of the track fits is also observed at each iteration. In each iteration, the detectors are first shifted and then rotated; then new residuals and rotation angles are calculated. This process is repeated iteratively until the residual means from the track fits become less than 0.005 mm. Fig. 3.21 shows the flow chart of the alignment algorithm. Figure. 3.22 shows the variation of track residuals for three trackers as a function of iteration number, with residual shifting to lower values progressively through iterations.

Alignment of GEM detectors w.r.t reference Tracker

Once the tracker alignment is complete, the next step is to align trapezoidal GEM detectors with respect to the centre of the aligned tracker system. A two-fold iteration loop is used, for this purpose, wherein the x-offset is kept fixed the y-offset is iterated over a set of values with a small iteration step. The x-offset is also iterated over and corresponding to every single value of x-offset, the y-offset are iterated. For each value of (X offset, Y offset) pair, tracks are linearly fitted in the ϕ co-ordinate and the corresponding residuals are noted and used to align the detectors.

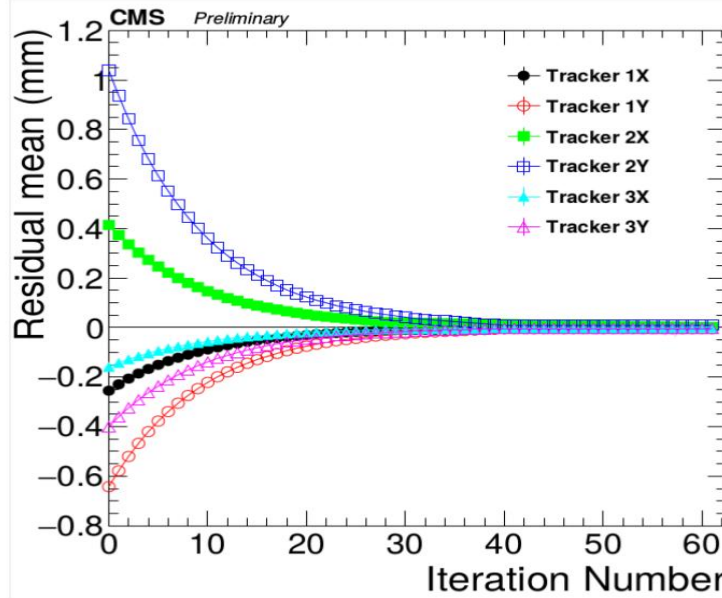


Figure 3.22: Variation of track residuals for three trackers with respect to the iteration number along different directions

Fiducial Area Selection

To have an efficient efficiency we should also define a fiducial area in which we are going to calculate the efficiency. We define the fiducial area as:

- Only valid tracks are considered during this procedure, which are defined as the tracks having hits registered in all the three trackers.
- These valid tracks are then extrapolated to GE1/1's. Only those tracks are finally selected for which the corresponding hit position in the GE1/1 has a residual value less than 5mm.
- The selected events are used to fill 2D histogram for different cases. The first histogram contains all those events that have a valid hit in the trackers only, as shown in Fig. 3.23 (left). Another 2D histogram is filled with all those events where there are valid hits in all three trackers as well as in the GE1/1, as shown in Fig. 3.23 (right). The ratio of the two histograms defined above is computed and is shown in Fig. 3.23 (bottom)
- Finally, the region (0,80) in the ratio histogram where efficiency is maximum is considered as the fiducial region. This fiducial region is used for the efficiency

calculation for GE1/1 detector.

Here, the calculated fiducial region is (0,80), which can be observed from Fig. 3.23(bottom).

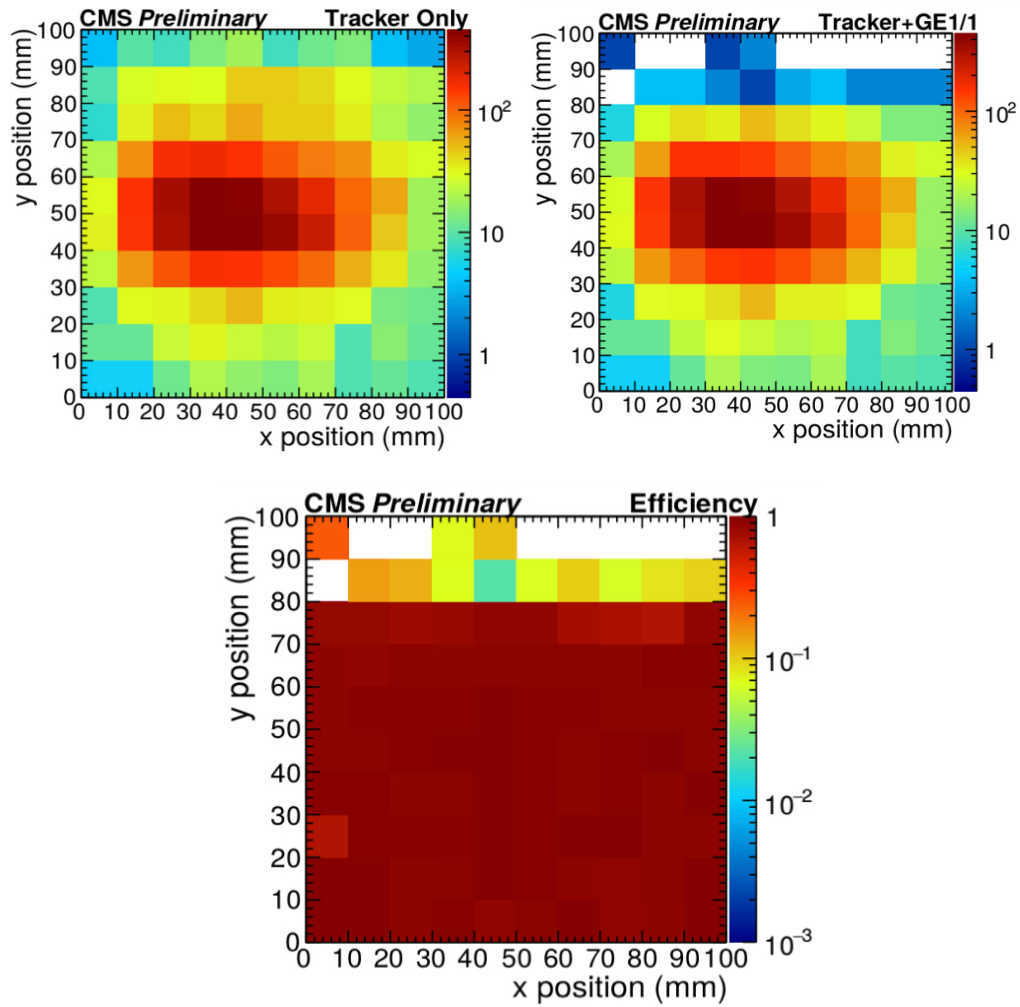


Figure 3.23: 2D distributions showing events with hits registered in the trackers (top left), events registered in three trackers and GE1/1's (top right) and the division of the two histograms used to define the fiducial region for GE1/1 efficiency measurements (bottom).

Efficiency Measurement

Efficiency, ϵ , for a GE1/1 detector for the current beam test set-up is defined as:

$$\epsilon = \frac{N_{GE1/1+Trk}}{N_{Trk}}, \quad (3.4)$$

where N_{Trk} is the number of reconstructed events with hits reconstructed in the three trackers and $N_{GE1/1+Trk}$ is the number of reconstructed events for which an actual hit is also found in the GE1/1 detector. Detector efficiency is calculated as a function of current supplied to the high-voltage divider as well as E_{gain} is shown in Fig. 3.24 where E_{gain} is defined as

$$E_{gain} = \frac{I \times R_{avg}^{gap}}{D}, \quad (3.5)$$

where I is current supplied to the HV divider, R_{avg}^{gap} is the average gap resistance of GE1/1, and D is thickness of the GEM foil. The efficiency is fitted with the function defined as:

$$\epsilon = \frac{\epsilon_{max}}{1 + e^{s(HV - HV_{50\%})}}, \quad (3.6)$$

Where, ϵ_{max} is the maximum obtained efficiency, $HV_{50\%}$ is the applied HV (or current or E_{gain}) at which the efficiency is 50% and s is just a scale factor left floating for fit to determine. Let us define four different function, based on equation 3.6, F1 for $(i\eta, i\phi)$ sector (5,2) with gas $Ar/CO_2/CF_4$, F2 for $(i\eta, i\phi)$ sector (1,2) with gas $Ar/CO_2/CF_4$, F3 for $(i\eta, i\phi)$ sector (8,2) with gas $Ar/CO_2/CF_4$ and F4 for $(i\eta, i\phi)$ sector (5,2) with gas Ar/CO_2 .

After fit F1 is given as

$$F1 = [0] + \frac{0.989}{[1] + \exp(-[2] \times (x - 697.3))}, \quad (3.7)$$

where,

$$[0] = -1.44526e - 02 \pm 4.28771e - 02,$$

$$[1] = 9.84833e - 01 \pm 4.19715e - 02, \text{ and}$$

$$[2] = 9.97591e - 01 \pm 8.53940e - 02$$

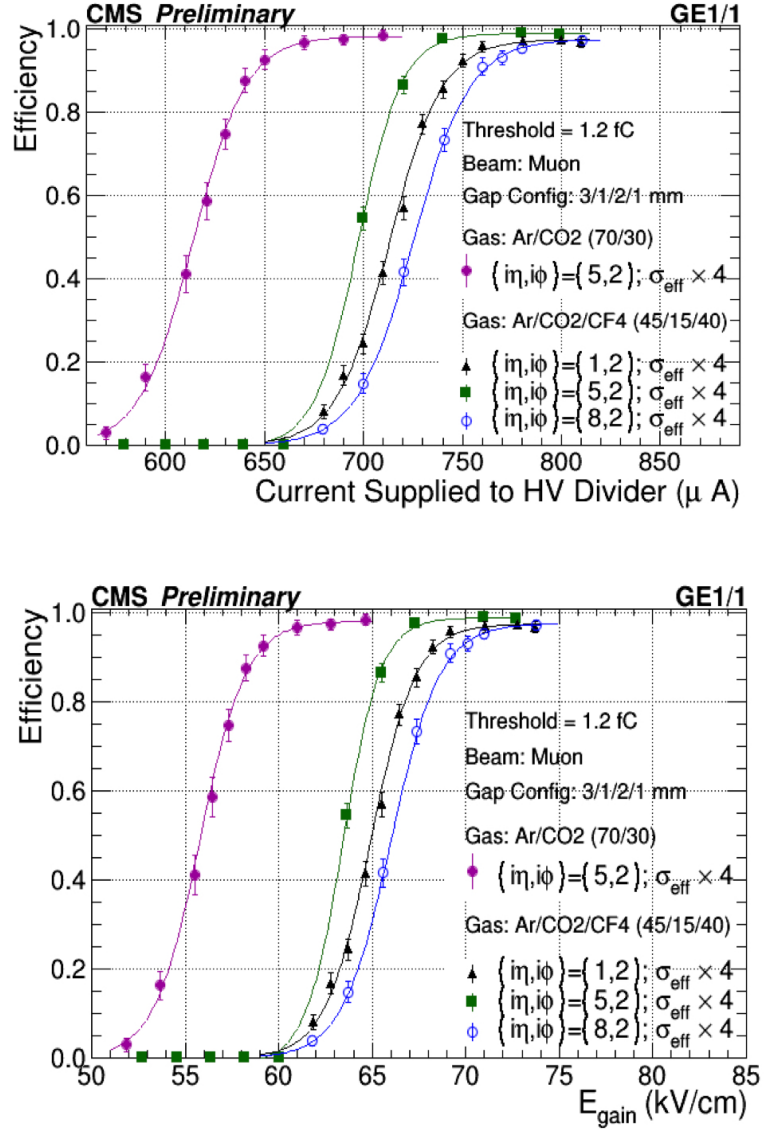


Figure 3.24: Efficiency with respect to E_{gain} for two different gases and three different $(i\eta, i\phi)$ sectors.

After fit F2 is given as

$$F2 = \frac{0.968}{[0] + \exp(-[1] \times (x - 64.9))} , \quad (3.8)$$

where,

$$\begin{aligned}[0] &= 9.92180e - 01 \pm 5.56034e - 03, \\ [1] &= 8.25180e - 01 \pm 3.62098e - 02\end{aligned}$$

After fit F3 is given as

$$F3 = \frac{0.973}{[0] + \exp(-[1] \times (x - 66))} , \quad (3.9)$$

where,

$$\begin{aligned}[0] &= 9.96407e - 01 \pm 9.00503e - 03, \\ [1] &= 7.67029e - 01 \pm 4.59276e - 02\end{aligned}$$

After fit F4 is given as

$$F4 = \frac{0.985}{[0] + \exp(-[1] \times (x - 55.8))} , \quad (3.10)$$

where,

$$\begin{aligned}[0] &= 1.00305e + 00 \pm 7.91473e - 03, \\ [1] &= 8.15287e - 01 \pm 5.46309e - 02\end{aligned}$$

Fig. 3.24 shows the GE1/1 detection efficiency with two different gas mixtures Ar/CO_2 (70/30) calculated for sector $(i\eta, i\phi) = (5, 2)$ and $Ar/CO_2/CF_4$ (45/15/40) for three different sectors $(i\eta, i\phi) = \{(1, 2), (5, 2), (8, 2)\}$. We achieved a very good efficiency of $\sim 98\%$ in all cases. It should be noted that the efficiency curves for different gas mixture do not coincide because for a given high voltage operating point, the effective gain of detector with Ar/CO_2 mixture is approximately one order of magnitude higher than that for the $Ar/CO_2/CF_4$ mixture. This implies that we can operate our detector without using CF_4 gas, which is non-eco friendly, without

compromising with the efficiency.

Time Resolution

The time resolution for a detector is defined as the time taken by detector to generate a signal on the readout electrode after the passage of particle through it. Experimentally, the time resolution is the root-mean-square of the Gaussian distribution of the time taken by the particle to reach detector from the scintillator. The detector time response is modelled as the Gaussian function, $f(t)$, convoluted with a square wave, $g(t)$, having a pulse length $f_{clk} = 25\text{ns}$ (LHC clock frequency) to represent discrete sampling. The functions $f(t)$ is given as:

$$f(t) = A e^{-\frac{1}{2}(\frac{t-t_0}{\sigma})^2}, \quad (3.11)$$

where A is amplitude of Gaussian function, t_0 is the mean value of Gaussian distribution, and σ is the standard deviation. And, $g(t)$ is given by

$$g(t) = \begin{cases} 0, & \text{else} \\ 1, & -\frac{f_{clk}}{2} < t < \frac{f_{clk}}{2} \end{cases}, \quad (3.12)$$

where f_{clk} is the length of created 40 MHz window. The convolution of the two functions is given as

$$(f * g)(t) = A \cdot \sigma \sqrt{\frac{\pi}{2}} \left(\operatorname{erf}\left(\frac{u_+}{\sigma\sqrt{2}}\right) - \operatorname{erf}\left(\frac{u_-}{\sigma\sqrt{2}}\right) \right), \quad (3.13)$$

where $u_{\pm} = t - t_0 \pm \frac{f_{clk}}{2}$. The experimental data are fitted with this convoluted function. The extracted time resolution as a function of E_{drift} and current supplied to high voltage divider are shown in Fig. 3.25.

Here, the time resolution for the detector operated using Ar/CO_2 gas mixture is fitted using a polynomial of degree 2, say $f(x) = a + bx + cx^2$. The parameter values for the time resolution as a function of the current supplied to high voltage divider are given below:

$$a = 297.06 \pm 2.94,$$

$$b = -0.75 \pm 0.006,$$

$$c = 0.0004 \pm 0.000006$$

The time resolution for the detector operated with $Ar/CO_2/CF_4$ gax mixture is fitted using a polynomial of order 6, say $g(x) = P_0 + P_1x + P_2x^2 + P_3x^3 + P_4x^4 + P_5x^5 + P_6x^6$. These parameters for the time resolution as a function of the current supplied to high voltage divider are given below:

$$P_0 = -386.42 \pm 1.86,$$

$$P_1 = 0.64 \pm 0.002,$$

$$P_2 = 0.0007 \pm 0.000004,$$

$$P_3 = -1.85e - 7 \pm 5.20e - 9,$$

$$P_4 = -1.48e - 9 \pm 6.64e - 12,$$

$$P_5 = -1.64e - 12 \pm 8.15e - 15,$$

$$P_6 = 2.53e - 15 \pm 9.50e - 18,$$

The time resolution with Ar/CO_2 (70/30) gas mixture is higher even for lower values of E_{drift} . This means that we are able to reach faster timing at lower gains with addition of CF_4 . This is important from the detector safety view point because this will allow us to operate the detector at lower gains, there by reducing the discharge probability.

Cluster Size Measurement

To measure the cluster size of GE1/1, clusterization algorithm is used. The basis of this algorithm is that we consider clusters if one or more continuous strips in GE1/1 are fired. Three golden run ranges, with different pseudo-rapidity sectors, viz 2014H4A, 2014H4C and 2014H4D are studied. The description of these runs is given in Table 3.1.

To fit the cluster size distribution, a Poisson distribution function is used. Figure 3.26 shows the cluster size distribution for different (η, ϕ) sector fitted using the Poisson distribution function.

The distribution is studied for different values of fiducial regions and it is observed that the cluster size is independent of the dimensions of the fiducial region (Fig. 3.27).

Cluster size study distributions for the GE1/1-IV and GE1/1-IV-GIF are plot-

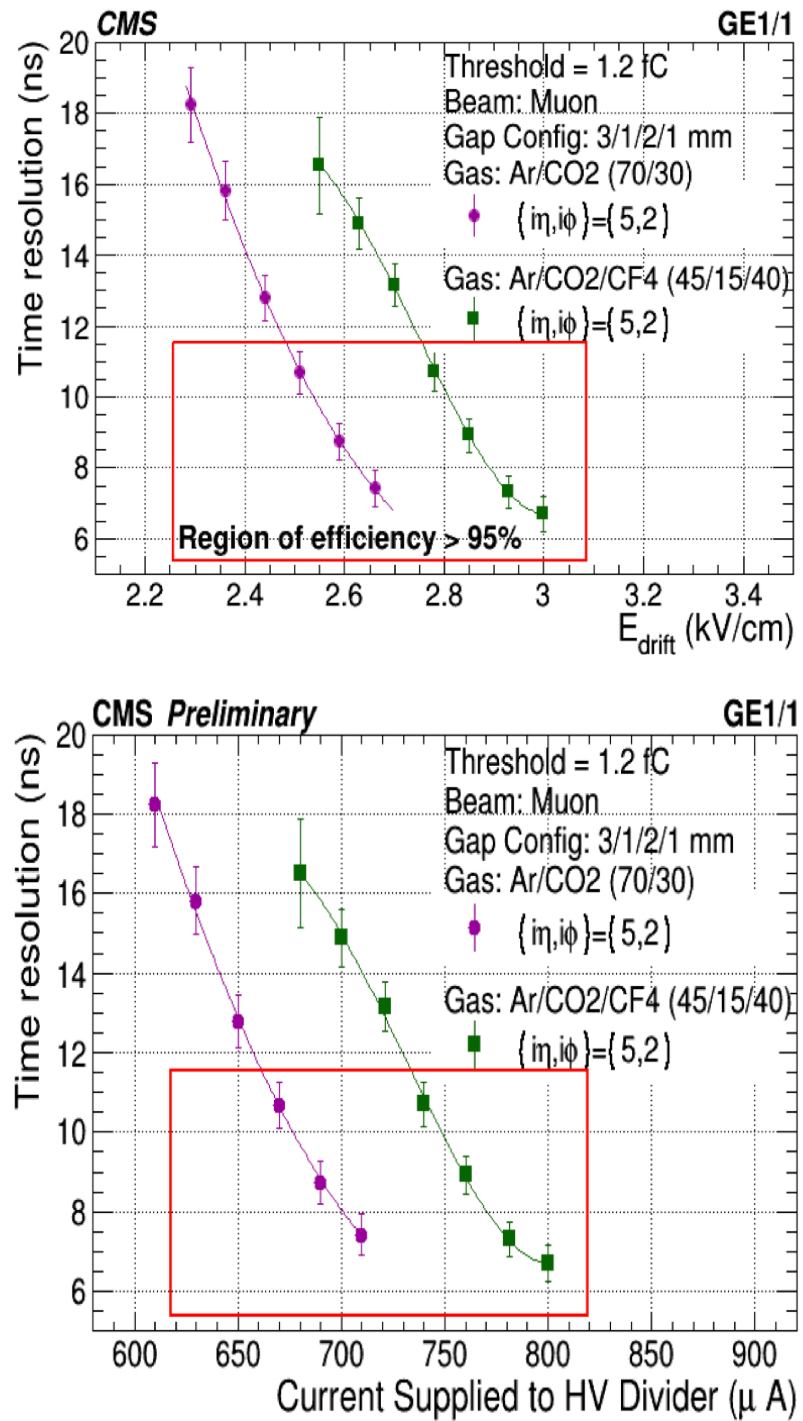


Figure 3.25: Time-resolution with respect to E_{drift} (top) and current supplied to high voltage divider (bottom) for two different gas mixture.

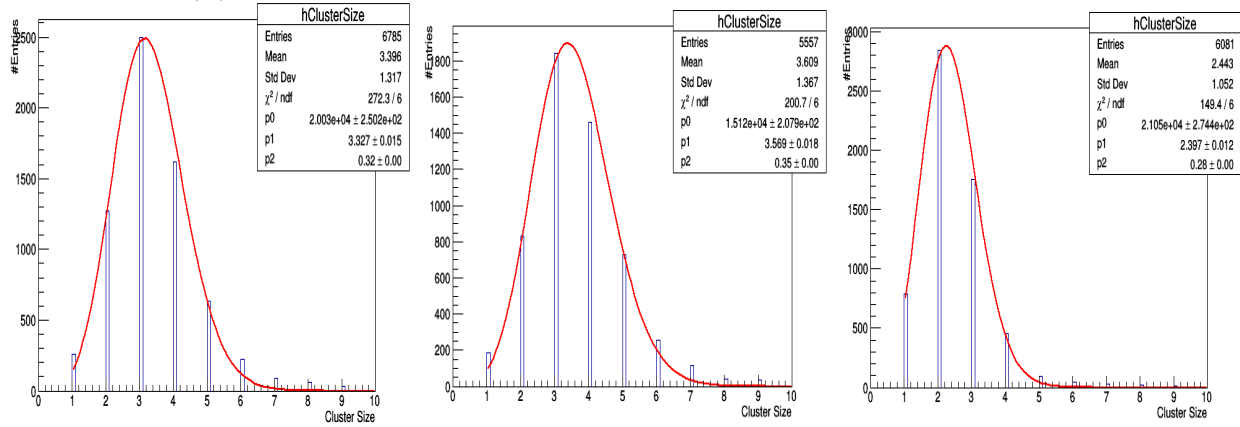


Figure 3.26: Cluster size distribution for GE1/1 detectors obtained during the beam test campaign: for run number 1644 in region $(\eta, \phi) = (5,2)$ (left), for the Run number 1869 in region $(\eta, \phi) = (8,2)$ (middle) and for Run number 2066 in region $(\eta, \phi) = (1,2)$ (right).

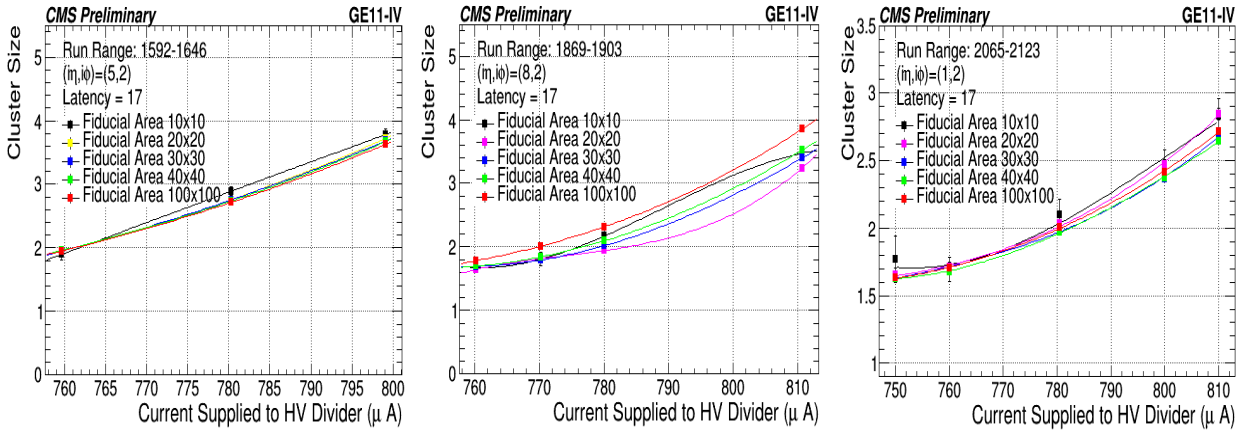


Figure 3.27: Mean value of cluster size distribution at different current supplied to high voltage divider obtained during the beam test campaign: for 2014H4A which was taken for region $(\eta, \phi) = (5,2)$ (left), for 2014H4C taken for region $(\eta, \phi) = (8,2)$ (middle) and for 2014H4D taken for region $(\eta, \phi) = (1,2)$.

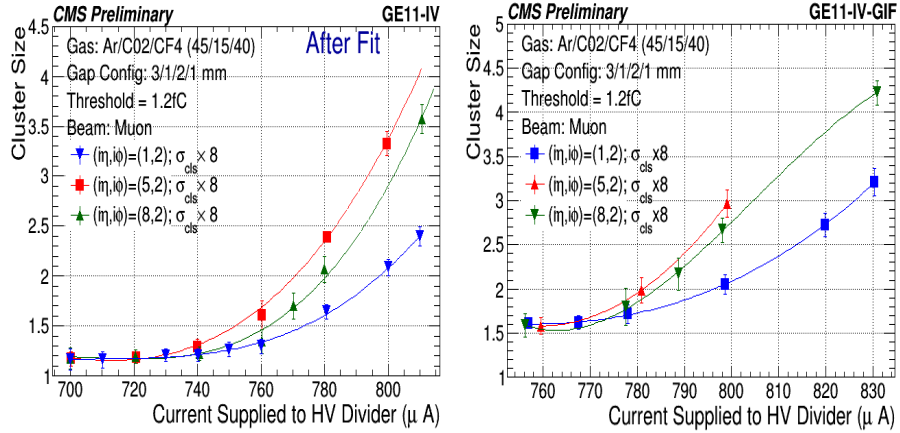


Figure 3.28: Cluster size distribution: Left - GE1/1-IV, Right - GE1/1-IV-GIF

ted as a function of current supplied to the high voltage divider and are shown in Figure 3.28. The cluster size is greater in $(\eta, \phi) = (5,2)$ region for both the detectors due to the uniformity in readouts channels. The GE1/1 4th generation prototype used suffered from the significant bending in the readout and drift PCB. This affects GE1/1 properties like primary charge created, uniformity, transparency of bottom of third GEM foil, charge collection by the readout, etc. Thus, it is expected that non-uniformity in the cluster size distribution in (η, ϕ) sector (1,2), (5,2), and (8,2) is a consequence of this. This issue is improved in the next version of GE1/1 prototype known as GE1/1-V.

To conclude, these beam test campaign ensured the good detection efficiency and fine spatial and latency resolution of GE1/1 detector. In the following section, the characterization studies performed during the development phase of GEM foils in India are reported.

3.4 Characterization and Production of GEM Foil

Through the Transfer of Technology (TOT) agreement with CERN and Micropack Pvt. Ltd. (a Bangalore based company), the process of the development of GEM foil in India in association with the Indian institutions begin. Micropack started producing the $10\text{ cm} \times 10\text{ cm}$ GEM foils using the single mask technique, as being used to produce GEM foils for GE1/1 detectors. Soon it was realized that the production

of GEM foil using the single mask technique is quite challenging and thus switched to the double mask production technique. Same production technique were adopted for the foil production as being done at the CERN PCB workshop [27].

Micropack used the Kapton foil having a thickness of $50 \mu m$ with $5 \mu m$ of copper coating on its either sides. Fig. 4.11a shows the $10 cm \times 10 cm$ GEM foil produced by Micropack and the cross-sectional view of its double conical hole is shown in Fig. 3.29b.

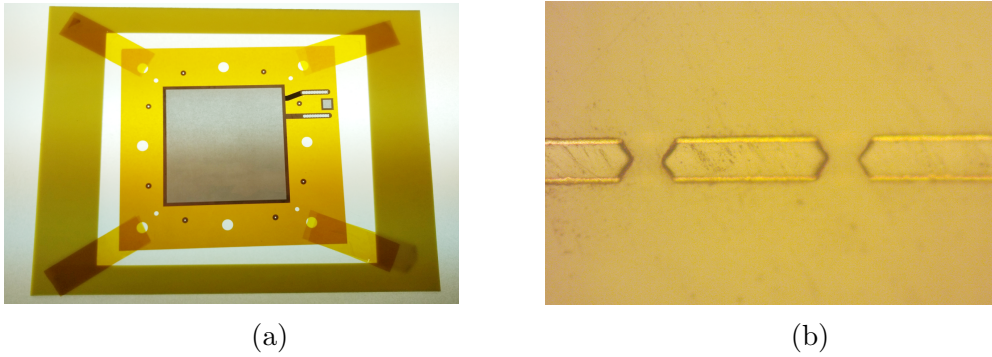


Figure 3.29: (a) $10 cm \times 10 cm$ GEM foil encapsulated in a frame and (b) Cross-sectional view of the foil showing the double cone structure of the engraved holes, developed by Micropack.

Before being used for the detector fabrication, the GEM foils required to pass certain quality control tests, which are listed below:

1. Visual inspection of foils,
2. Optical test, and
3. Electrical test

All these tests are required to be performed in the clean room⁵ of at least class 1000 or better. This is done to avoid the filling up of GEM foils with dust particles. Even a small amount of dust inside the GEM holes could lead to a destructive discharge thereby destroys the whole foil. At Delhi University, all the tests and characterisation

⁵Clean room is a specially designed room, maintained at extremely low level of particles per cubic meters, for a specialized industrial production or scientific research. For example, a “*Class-100*” clean room is designed to never allow more than 100 particles (0.5 microns or larger) per cubic foot of air. “*Class-1000*” and “*Class-10000*” clean rooms are designed to limit particles to 1000 and 10,000 respectively.

of foils was done in a class 100 clean-room. The clean room schematic representation is shown in Fig. 3.30. The dimension of the clean room is $14 \text{ ft} \times 12 \text{ ft} \times 8 \text{ ft}$, which allows 2-3 people to work comfortably wearing the clean-room dressing. It is equipped with the humidity and temperature control systems to have a controlled environment. Along with this it is also continuously monitored with a dust particle counter, in real time, with KANOMAX dust particle counter model 3887 [86].

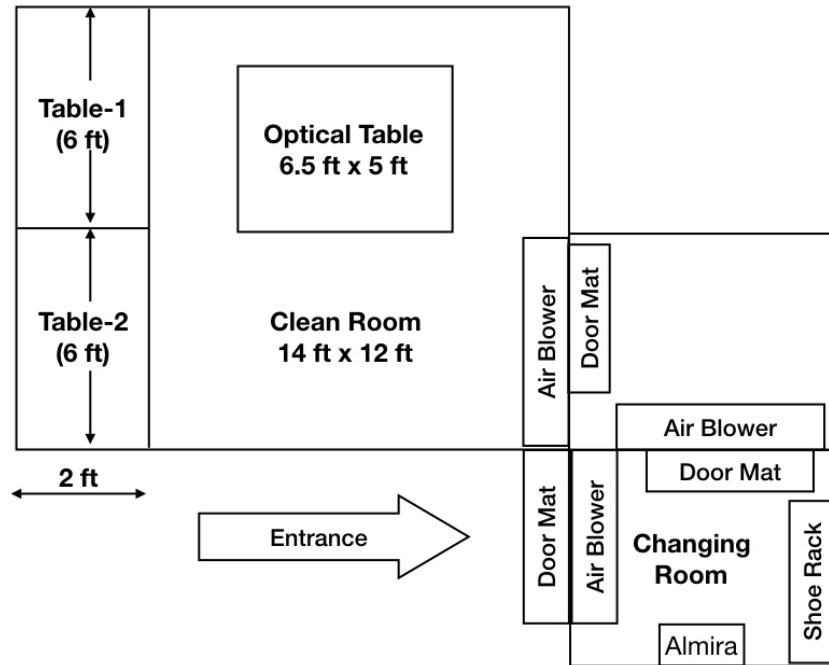


Figure 3.30: A schematic representation of the clean room of class 100 at University of Delhi, where the characterisation of foils was performed.

3.4.1 Visual Inspection of Foils

At first one has to inspect visually the GEM foil for any dust or defects visible to the naked eye. GEM foils are cleaned using the adhesive rolled as shown in Fig. 3.31 to remove dust particles.

3.4.2 Optical Test

Optical test is carried out to check the GEM foil for any:

- microscopic defects, not visible to the eyes and



Figure 3.31: Adhesive roller used for the cleaning of GEM foil.

- to measure the inner and outer hole diameter and the pitch size.

The motivation to perform the optical test is following:

- The foil defects such as the over-size hole, missing hole, excess etching, etc could degrade the performance of foil and thus the overall detector efficiency.
- As the gain of the detector depends on the diameter of the hole and thickness of the foil (as shown in Fig. 3.32). Thus, it is necessary to check their dimensions.

To check any defects and to measure the hole-size and pitch for a GEM foil several methods have been developed using an automated 2D-CCD scanner [88, 89]. However, we used a different technique. We divided the GEM foil into several sectors and captured a high-resolution picture using the AF-S Micro Nikon 40 mm 1:2.8G lens. We used a softbox ($1\text{ m} \times 1\text{ m}$) light source for uniformly illuminating the GEM foil. A sketch of the set-up is shown in Fig. 3.33. Fig 3.34 shows the found defects in the considered GEM foil. Also, the observed number of defects are shown in Fig. 3.35. Out of 600,000 holes in the GEM foil, defects were found in 785 holes, i.e., 0.13% of total holes are defected. Also, similar number of defects were observed in other two GEM foils. The resulting local effects in the GEM foil due to these small fractions of defected holes are not expected to deteriorate the overall performance of the GEM detector.

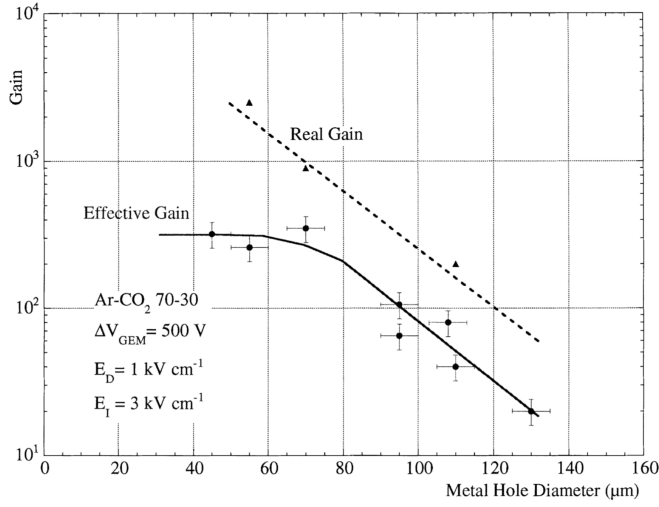


Figure 3.32: Real gain and effective gain variation with GEM hole diameter [87] having a foil thickness of $60 \mu\text{m}$ ($= 50 \mu\text{m} + 5\mu\text{m} + 5 \mu\text{m}$). As the hole diameter decreases, the effective gain increases till $70 \mu\text{m}$ and after that it reaches saturation. This is due to loss of generated electrons in the avalanche to the bottom of the GEM electrode when hole diameter is reduced below the foil thickness.

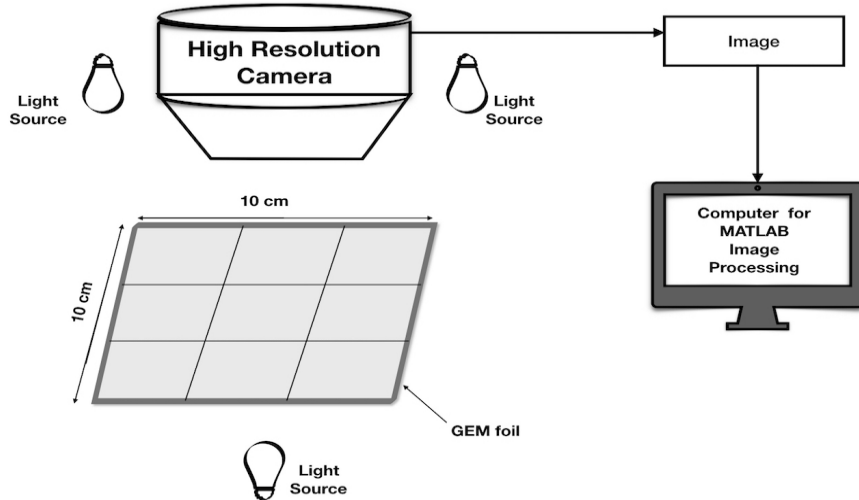


Figure 3.33: Sketch of the set-up used for optical measurements of the GEM foil.

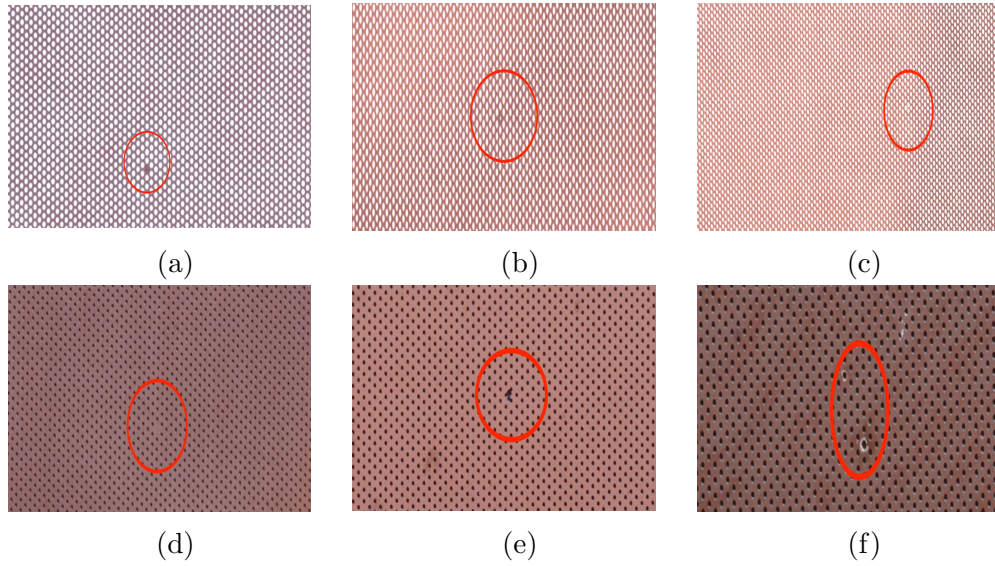


Figure 3.34: Observed imperfections in the GEM foils: (a) Un-etched area, (b) under-size hole, (c) over-size hole (d) missing hole, (e) excess etching and (f) burnt area.

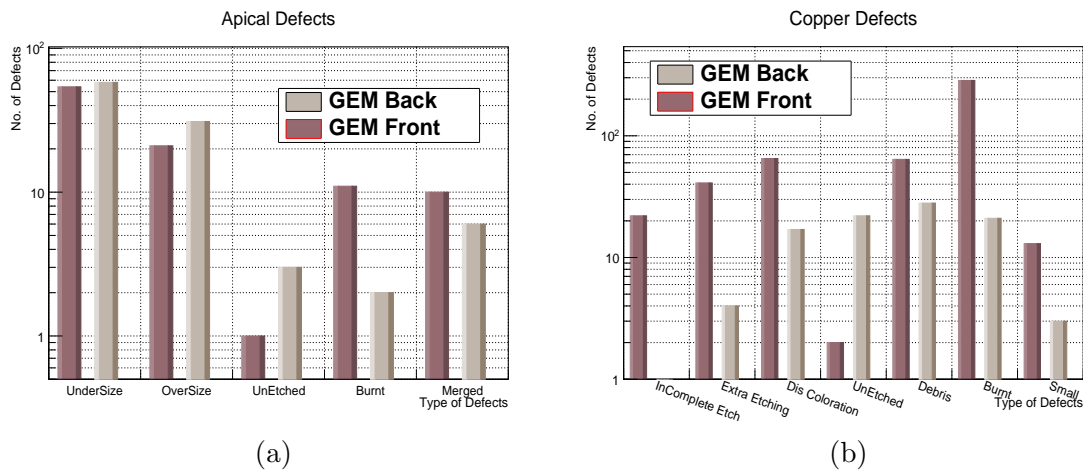


Figure 3.35: Number of defects seen in (a) Insulator (Apical Type NP) and (b) Copper, for one of the 10 cm x 10 cm foil.

3.4.3 Electrical Test

This is one of the most important tests for the GEM foil, which deals with the measurement of leakage or dark current. Dark current exceeding the prescribed limits could lead to a short circuit in the foil thereby damaging the foil permanently. A spark can also be produced due to presence of dust particle on the GEM foil, hence, the cleanliness of GEM foils is also ensured during this test. But, if a huge number of frequent sparks happen then we should quickly stop the electricity and clean the foil properly. The electricity test are carried out for foils in two steps as per the CERN standards [90]:

1. Quality control fast or QC-fast and
2. Quality control for long or QC-long.

QC-long and QC-short tests differ in terms of the duration for which high voltage is applied to the detector to monitor its leakage current. Other difference is that QC-fast gives us a quick result about the leakage current or electrical connectivity of the foils while QC long provides the behaviour of foil at high voltages and gives us the actual leakage current and the number of discharges if present.

QC-fast

This test is performed using the insulation tester MIT Megger 420 [91]. This test confirms that the foil have good electrical connectivity. As 550 V potential is applied across the GEM foil for about a minute, current does not exceed 10 nA and the resistivity in the air between the two foils exceeds $2 \text{ G}\Omega$.

QC-long

For this, the measurement the electronics set-up is shown in Fig. 3.36. It consists of a GEM foil enclosed in a Plexiglass enclosure in which nitrogen gas is continuously floated. The foil was connected to a the Keithley 6517B picoammeter [92] interfaced with a computer via a GPIB interface and the LabView program is used to record the measurements. The leakage current is measured as a function of applied voltage as shown in Fig. 3.37a. Also, for the sake of comparison same measurement was made with $10 \text{ cm} \times 10 \text{ cm}$ GEM foil produced at CERN. The results using the CERN foil are shown in Fig. 3.37b. It is observed that the two foils - one produced by Micropack

3. GAS ELECTRON MULTIPLIER

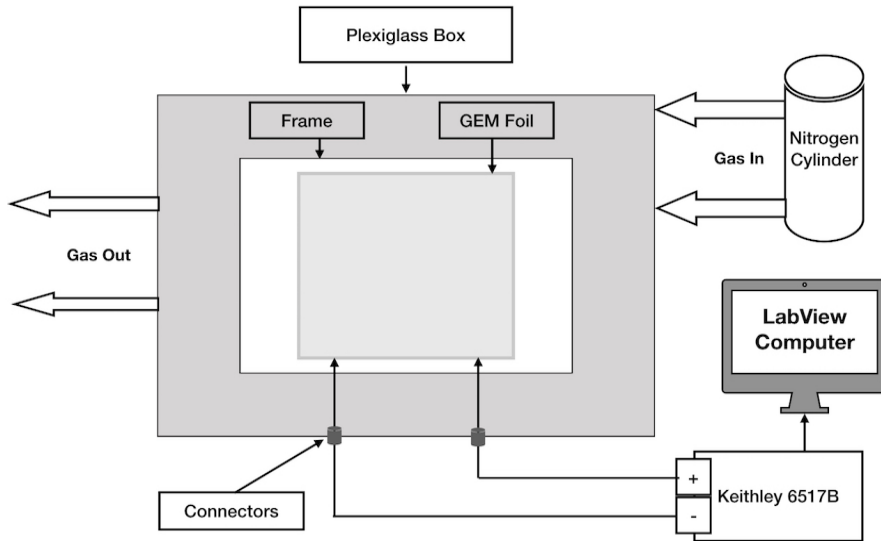


Figure 3.36: Sketch of the set-up used for the measurement of leakage current.

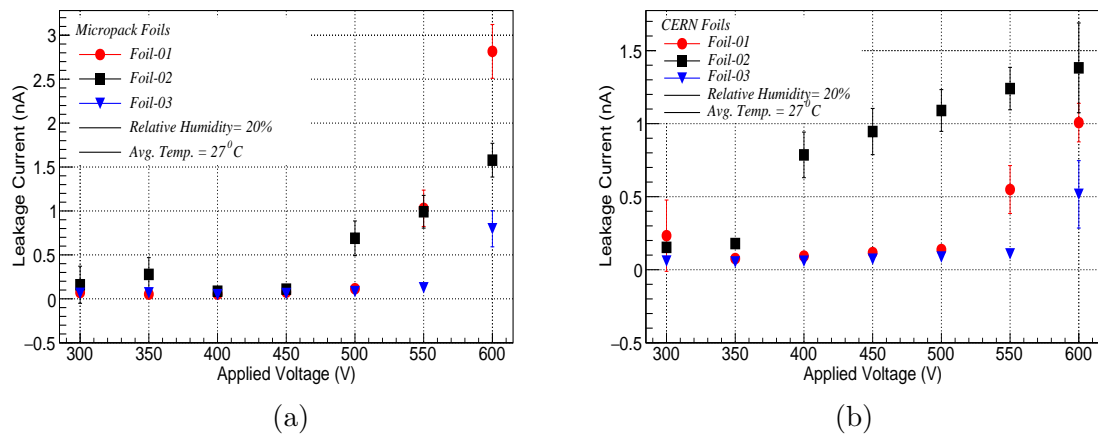


Figure 3.37: Leakage Current for (a) Micropack Foils and (b) CERN Foils, at an average temperature of $T=27^\circ\text{C}$ and 20% relative humidity.

and another produced at CERN - show similar behaviour and the leakage currents are well within the limit (10 nA), set by CERN QC criteria.

4

Anomalous Quartic Gauge Coupling Measurement

At the LHC, VBS is characterized by presence of two gauge bosons in association with two forward jets with large rapidity separation and a large dijet mass. The VBS topology is produced via the EW interaction with increased sensitivity to quartic gauge couplings. Figure 4.1 shows the Feynman diagrams involving quartic vertices. An excess of events with respect to SM predictions could indicate the presence of anomalous Quartic Gauge Couplings (aQGCs) [93] or the existence of new resonances.

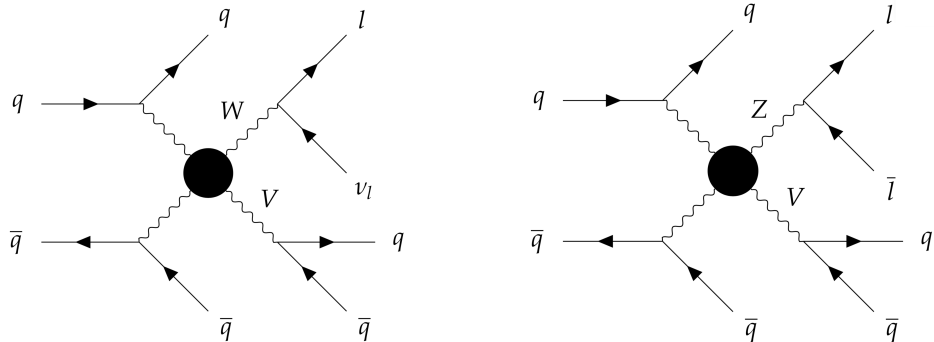


Figure 4.1: VBS Feynman diagrams contributing to the EW induced production of events containing a hadronically decaying gauge boson (V), a W (left) or Z (right) boson decaying to leptons (electrons or muons), and two forward jets. New physics in the EW sector can modify the quartic gauge coupling.

The main goal of this analysis is to search for the presence of aQGCs in candidate events containing a hadronically decaying gauge boson (V) produced with large

transverse momentum P_T , a W or Z boson decaying to leptons (electrons or muons), and two forward jets. This final state benefits from a higher branching ratio of the V decay compared to previous searches at the LHC for aQGCs in VBS involving only leptonic boson decays [94, 95, 96, 97, 98, 99, 100, 101, 102, 103]. The ATLAS collaboration reported limits on aQGCs in VBS using the WW final state, where W decays to leptons, in proton-proton (pp) collisions at $\sqrt{s} = 8\text{TeV}$ [104].

Extended Higgs sectors with additional SU(2) isotriplet scalar give rise to charged Higgs bosons with couplings to W and Z bosons at the tree level [**CE1**, 105]. In particular, the Georgi-Machacek (GM) [19] model, with both real and complex triplets, preserves the tree level custodial symmetry. In this model, singly and doubly charged Higgs bosons are produced via vector boson fusion (VBF) and decay to W and Z bosons, and same-sign W boson pairs, respectively. The ATLAS and CMS Collaborations performed searches for charged Higgs bosons in these topologies and set constraints on the GM model [94, 106, 107].

This chapter presents a study of VBS in WW, WZ, and ZZ final states using pp collisions at $\sqrt{s} = 13\text{TeV}$. The data sample corresponds to an integrated luminosity of $35.9 \pm 0.9\text{fb}^{-1}$ collected with the CMS detector [108] at the CERN LHC in 2016.

4.1 Sample Used

Several Monte Carlo (MC) event generators are used to simulate the signal and background processes. For all processes, the detector response is simulated using a detailed description of the CMS detector, based on the GEANT4 package [109], and event reconstruction is performed with the same algorithms as used for data. Proton-proton interactions occurring in the same beam crossing bin as the event of interest (pileup) are included in the simulation samples. The simulated events are weighted so that the pileup distribution matches the data, with an average pileup of about 27 interactions per beam crossing.

4.1.1 Data samples

This analysis uses a sample of proton-proton collisions collected in 2016 with the CMS experiment at the LHC at $\sqrt{s} = 13\text{ TeV}$. Only data that passed the quality

certification by all detector subsystems is used in the analysis using the golden JSON¹ in order to select good data. *SingleMuon* and *SingleElectron* primary datasets are used, which corresponds to the trigger that demands that there should be at least one muon and electrons, respectively in the collected data. The names of data samples used in the analysis are listed in Table 4.1

Data stream	Run and reconstruction version
SingleMuon	Run2016B-03Feb2017-v2
SingleElectron	Run2016C-03Feb2017
	Run2016D-03Feb2017
	Run2016E-03Feb2017
	Run2016F-03Feb2017
	Run2016G-03Feb2017
	Run2016H-03Feb2017-v1
	Run2016H-03Feb2017-v2
	Run2016H-03Feb2017-v3

Table 4.1: List of data samples used in the analysis. Here different run names corresponds to the different time stamp during which data was collected, and the date in the data sample name corresponds to the time stamp at which it was converted to the physics objects, i.e, electrons, muons, jets, etc from the hit and energy deposit information.

4.1.2 Simulated Samples

The EW processes with two final state quarks are simulated using `MADGRAPH5_aMC@NLO` 2.3.3 [110] at leading-order (LO) with six electroweak (EWK) and zero quantum chromodynamics (QCD) vertices. The $W^\pm W^\pm$, $W^\pm W^\mp$, $W^\pm Z$, and ZZ processes are produced separately. The complete list of the SM background samples can be found in Table 4.3 and Table 4.2. The QCD initiated production of two gauge bosons with two final state quarks (which we refer to as diboson process) and at least one QCD vertex is considered as background. `MADGRAPH5_aMC@NLO` at LO is used to simulate this sample. The interference between the EWK and QCD diagrams

¹In CMS, the information for the proton-proton collision runs which are considered as good and should be processed are kept in a file in JSON format (JSON stands for Java Script Object Notation.) using the information of luminosity sections. The JSON file that was used for 2016 run is

Cert_271036-284044_13TeV_23Sep2016ReReco_Collisions16_JSON.txt

This corresponding to an integrated luminosity of $35.9 \pm 0.9 \text{ fb}^{-1}$

Process	Sample name	Total events	Cross section[pb]
$pp \rightarrow W^+W^-JJ \rightarrow l^+\nu JJJJ$	WplusToLNuWminusTo2JJJ_EWK_LO_aQGC	1,981,940	17.940
$pp \rightarrow W^+W^-JJ \rightarrow l^-\nu JJJJ$	WplusTo2JWminusToLNuJJ_EWK_LO_aQGC	1,994,595	17.920
$pp \rightarrow W^+W^+JJ \rightarrow l^+\nu JJJJ$	WplusToLNuWplusTo2JJJ_EWK_LO_aQGC	200,000	3.451
$pp \rightarrow W^-W^-JJ \rightarrow l^-\nu JJJJ$	WminusToLNuWminusTo2JJJ_EWK_LO_aQGC	200,000	0.507
$pp \rightarrow W^+ZJJ \rightarrow l^+\nu JJJJ$	WplusToLNuZTo2JJJ_EWK_LO_aQGC	399,232	1.895
$pp \rightarrow W^+ZJJ \rightarrow l^+l^-JJJJ$	WplusTo2JZTo2LJJ_EWK_LO_aQGC	199,238	0.569
$pp \rightarrow W^-ZJJ \rightarrow l^-\nu JJJJ$	WminusToLNuZTo2JJJ_EWK_LO_aQGC	200,000	0.741
$pp \rightarrow W^-ZJJ \rightarrow l^+l^-JJJJ$	WminusTo2JZTo2LJJ_EWK_LO_aQGC	198,620	0.222
$pp \rightarrow ZZJJ \rightarrow l^+l^-JJJJ$	ZTo2LZTo2JJJ_EWK_LO_aQGC	99,532	3.361

Table 4.2: aQGC signal sample names and cross sections of simulated samples used in the analysis

Process	Sample name	Total events	Cross section[pb]
$pp \rightarrow W^+W^-JJ \rightarrow l^+\nu JJJJ$	WplusToLNuWminusTo2JJJ_EWK_LO_aQGC	1,991,279	0.9114
$pp \rightarrow W^+W^-JJ \rightarrow l^-\nu JJJJ$	WplusTo2JWminusToLNuJJ_EWK_LO_aQGC	1,994,040	0.9107
$pp \rightarrow W^+W^+JJ \rightarrow l^+\nu JJJJ$	WplusToLNuWplusTo2JJJ_EWK_LO_aQGC	198,858	0.0879
$pp \rightarrow W^-W^-JJ \rightarrow l^-\nu JJJJ$	WminusToLNuWminusTo2JJJ_EWK_LO_aQGC	199,535	0.0326
$pp \rightarrow W^+ZJJ \rightarrow l^+\nu JJJJ$	WplusToLNuZTo2JJJ_EWK_LO_aQGC	393,190	0.1825
$pp \rightarrow W^+ZJJ \rightarrow l^+l^-JJJJ$	WplusTo2JZTo2LJJ_EWK_LO_aQGC	198,932	0.0540
$pp \rightarrow W^-ZJJ \rightarrow l^-\nu JJJJ$	WminusToLNuZTo2JJJ_EWK_LO_aQGC	199,547	0.1000
$pp \rightarrow W^-ZJJ \rightarrow l^+l^-JJJJ$	WminusTo2JZTo2LJJ_EWK_LO_aQGC	198,910	0.0298
$pp \rightarrow ZZJJ \rightarrow l^+l^-JJJJ$	ZTo2LZTo2JJJ_EWK_LO_aQGC	100,000	0.0159

Table 4.3: SM EWK signal sample names and cross sections of simulated samples used in the analysis

is evaluated using dedicated samples produced with the PHANTOM 1.2.8 [111] generator and is found to be negligible compared to the theoretical uncertainties. Figure 4.2 shows the level of the interference contribution.

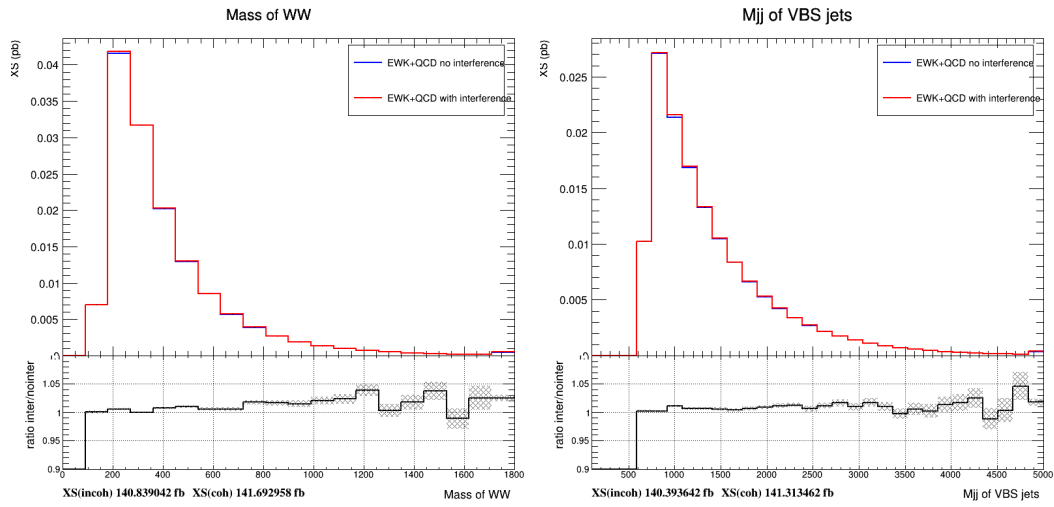


Figure 4.2: Distributions of m_{WW} (left) and m_{jj} (right) in the signal region with interference contribution (red) and without interference contribution (blue).

The aQGC signal samples are produced using MADGRAPH5_aMC@NLO at LO accu-

racy. The default coupling for the event generation is set to $f_{T0}/\Lambda^4 = -12.5[\text{TeV}]^{-4}$. Other coupling strengths are obtained by means of the reweighting method in MADGRAPH5_aMC@NLO [112, 113]. Figure 4.3 shows the mass distributions of the WW system for few aQGC parameters for the operators $S0$ (left) and $T2$ (right). The expected enhancement of the production cross section at large masses for nonzero aQGC is clearly seen.

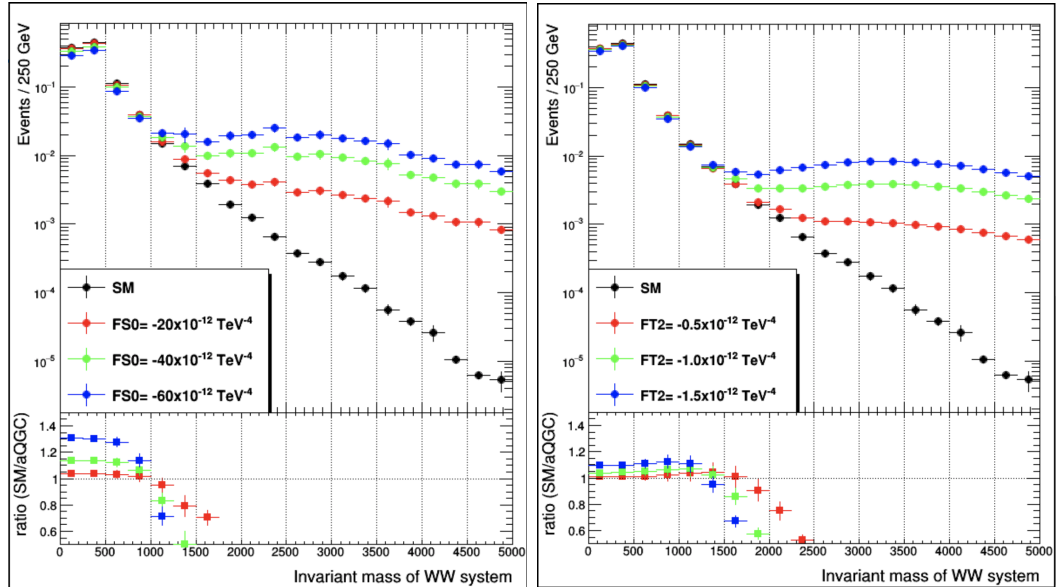


Figure 4.3: Mass distributions of the WW system for the SM EW and few aQGC parameters for the operators $S0$ (left) and $T2$ (right).

The Drell–Yan process is simulated with one, two, three, and four outgoing partons at Born level at LO using MADGRAPH5_aMC@NLO. The W+jets process is simulated at LO in H_T^2 bins using MADGRAPH5_aMC@NLO. $t\bar{t}$, $t\bar{t}W$, $t\bar{t}Z$, and single top processes are generated at next-to-leading order (NLO) using POWHEG2.0 [114, 115, 116, 117]. The simulated samples of background processes are normalized to the best theoretical prediction. The complete list of background samples can be found in Table 4.4.

The PYTHIYA 8.205 [118] package is used for parton showering, hadronization, and the underlying event simulation, with tune CUETP8M1 [119, 120]. The NNPDF 3.0 [121] set is used as the default set of parton distribution functions (PDFs). The PDFs are calculated to the same order in QCD as the hard process.

² H_T is defined as the sum of transverser momentum of all jets in an event.

Sample name	Cross section[pb]
WJetsToLNu HT bins 100 to 200 GeV	1345*1.21
WJetsToLNu HT bins 200 to 400 GeV	359.7*1.21
WJetsToLNu HT bins 400 to 600 GeV	48.91*1.21
WJetsToLNu HT bins 600 to 800 GeV	12.05*1.21
WJetsToLNu HT bins 800 to 1200 GeV	5.501*1.21
WJetsToLNu HT bins 1200 to 2500 GeV	1.329*1.21
WJetsToLNu HT bins 2500 GeV to Inf	0.03216*1.21
TTbar	831.76
Single Top production s-channel	3.68
Single Top production t-channel	136.02
Single Anti-Top production t-channel	80.95
Single Anti-Top production tW-channel	35.6
Single Top production tW-channel	35.6
Drell-Yan + 1 jet	1012
Drell-Yan + 2 jet	335
Drell-Yan + 3 jet	102
Drell-Yan + 4 jet	54

Table 4.4: Background sample names and cross sections of simulated samples used in the analysis. The naming

4.2 Object Selection

A set of standard objects used in this analysis is summarized in Table 4.5. More details are given below.

Objects	Selections
Triggers	Single lepton triggers
Primary vertex	Nominal selection
jets	PF jets, anti- k_T , $\Delta R = 0.4$
V jets	Puppi+SD, anti- k_T , $\Delta R = 0.8$
E_T^{miss}	Type-1 PF E_T^{miss}
B-tagging	CSVv2 “Loose”
Electrons	tight POG identification criteria
Muons	tight POG identification criteria

Table 4.5: Summary of object selection.

4.2.1 Trigger

The data samples used in the analysis were taken with the following triggers:

- HLT_Ele27_WPTight_Gsf_v* (electron channel)
- HLT_IsoTkMu24_v* or HLT_IsoMu24_v* (muon channel)

The explanation of these triggers are given in Table 2.3. The trigger efficiencies in data and simulation are measured using tag-and-probe [122]. In tag-and-probe method the correction factors for the values extracted from the simulation are determined using $Z \rightarrow l^+l^-$ sample in both data and simulation. This removes any systematic uncertainty coming from imperfections in the simulation. For the measurement for a given efficiency contains events selected with two lepton candidates. The first lepton, known as “tag”, was chosen based on the tight identification and isolation requirements. The other leptons, known as “probe”, is selected based on the criteria which depends on the efficiency being measured. The invariant mass of the chosen tag and probe lepton candidate should fall in the range of 60-120 GeV. The signal yields are obtained for two exclusive subsamples of events in which the probe lepton passes or fails the selection criteria considered. Fits are performed to the invariant-mass distribution of the pass and fail subsamples, including a term that accounts for the background. The measured efficiency is deduced from the relative level of signal in the pass and fail subsamples; its uncertainty includes a systematic contribution from the fitting procedure. The correction factors are obtained as ratios of tag-and-probe efficiencies for the data and for the simulation. The ratio of data and simulation efficiencies is found to be consistent with unity within 1%.

4.2.2 Electron selection

Electron selection variables are categorized into three groups: identification (ID) variables, isolation variables and conversion rejection variables [123, 124].

The most powerful ID variables for the electron identification are:

1. the energy-momentum match between the seed cluster and the track, E_{seed}/p_{in} ,
2. the variables measuring spatial matching between the track and the supercluster, $\Delta\eta_{in}$ and $\Delta\phi_{in}$,
3. the supercluster η width, $\sigma_{i\eta i\eta}$, taken from the covariance matrix using the logarithmic weights, and
4. the hadronic leakage variable H/E .

The isolation of the electron candidates is computed from the flux of PF candidates found within a cone of $\Delta R = 0.4$ built around the lepton direction. The flux of particles is computed independently for the charged hadrons, neutral hadrons and photon

Variables	Veto	Loose	Medium	Tight
$\sigma_{in\eta} <$	0.0115	0.011	0.00998	0.00998
$ \Delta\eta_{in} <$	0.00749	0.00477	0.00311	0.00308
$\Delta\phi_{in} <$	0.228	0.222	0.103	0.0816
$H/E <$	0.356	0.298	0.253	0.0414
$I_{rel}^e <$	0.175	0.0994	0.0695	0.0588
$ 1/E - 1/p <$	0.299	0.241	0.134	0.0129
expected missing inner hits $<=$	2	1	1	1
pass conversion veto	yes	yes	yes	yes

Table 4.6: The cut based electron identification working points for $|\eta_{\text{supercluster}}| \leq 1.479$.

candidates. When dealing with electron candidates, the neutral flux is corrected by using the average energy density due to pileup and underlying event in the central region of the detector (ρ) and an effective area (A_{eff}) correction which normalizes this estimator in such a way that the isolation is independent of the number of pileup interactions. The electron isolation is therefore defined as:

$$I_{\text{rel}}^e = \frac{1}{p_T} [I_{\text{ch}} + \max(I_{\text{nh}} + I_g - A_{\text{eff}} \cdot \rho, 0)] \quad (4.1)$$

Now for the conversion rejection three sets of variables are used. The transverse impact parameter is used to discriminate electrons from conversion as they will have, on average, a greater distance to the beam position. We also expect an electron from a conversion to have missing hits in the innermost tracker layer.

Finally based on the above explanation the electrons identification variables are divided into the three categories based on the cuts with increasing background rejection power and decreasing signal efficiency: tight, medium, loose, veto and also in the endcap and barrel. All these parameters are summarized in Table 4.6 and Table 4.7.

For this analysis the electrons are selected using the “Tight” ID. In addition, an electron veto is applied with the “Loose” ID, to reject events with more than two genuine leptons.

Furthermore, the scale factors are used to correct for differences in the reconstruction, identification and isolation efficiencies between data and simulation. They are evaluated using the tag and probe technique, considering the scale factors and their uncertainty both.

Variables	Veto	Loose	Medium	Tight
$\sigma_{in\eta} <$	0.037	0.0314	0.0298	0.0292
$ \Delta\eta_{in} <$	0.00895	0.00868	0.00609	0.00609
$\Delta\phi_{in} <$	0.213	0.213	0.045	0.0394
$H/E <$	0.211	0.101	0.0878	0.0641
$I_{rel}^e <$	0.159	0.107	0.0821	0.0571
$ 1/E - 1/p <$	0.15	0.14	0.13	0.0129
expected missing inner hits \leq	3	1	1	1
pass conversion veto	yes	yes	yes	yes

Table 4.7: The cut based electron identification working points for $|\eta$ supercluster| > 1.479 .

4.2.3 Muon selection

For muons reconstruction two approaches are used:

1. **the global muon reconstruction (outside-in):** In this case, a tracker-track is found for each standalone-muon track and a combined fit of the tracker and muon-detector hits is performed, using the Kalman-filter technique [56, 125].
2. **the tracker muon reconstruction (inside-out):** Here, the tracker-track is extrapolated and matched to segments reconstructed in the muon detector and it is said to be matched if the distance between them is less than 3 cm or if the value of the pull is less than 4, where the pull is defined as the difference between the position of the matched segment and the position of the extrapolated track, divided by their combined uncertainties.

At low momenta, $p \leq 5 \text{ GeV}$, the tracker muon reconstruction is more efficient than the global muon reconstruction, as it requires only a single muon segment in the muon system, whereas the global muon reconstruction is designed to have high efficiency for muons penetrating through more than one muon station and typically requires segments in at least two muon stations.

For muon identification there are six different algorithms are commonly used in CMS. They are Loose Muons, Medium Muons, Tight Muons, Soft Muons, High p_T Muons, and High p_T Tracker Muons. Here only Loose and Tight muon selections are described which are used in the analysis [126].

1. **Loose muon selection:** This requires a candidate to be reconstructed by the particle-flow algorithm [127] and a global or a tracker-muon.

2. **Tight muon selection:** This requires the particle to be identified as muons by the particle flow event reconstruction and as global as well as the tracker muon with requirements on the hits, global track χ^2 , and the impact parameters.

The muons are selected using the “*Tight*” muon identification mentioned above. Additionally, like in the electron case, a third muon veto is also applied to reject events with more than two genuine leptons using the “*Loose*” identification. For the muon isolation, in the same manner as for electrons, a cone of $\Delta R = 0.4$ is built to compute the flux of particle flow candidates, the “delta-beta” correction is applied to correct for pileup contamination. This correction is achieved by subtracting half the sum of the P_T of the charged particles in the cone of interest but with particles not originating from the primary vertex.

The muon isolation is therefore defined as:

$$I_{\text{rel}}^\mu = \frac{1}{p_T} [I_{\text{ch}} + \max(I_{\text{nh}} + I_g - 0.5 \cdot I_{\text{chPU}}, 0)] \quad (4.2)$$

Scale factors are used to correct for differences in the reconstruction, identification and isolation efficiencies between data and simulation. They are evaluated using the tag and probe technique, using both the scale factors and their uncertainty.

4.2.4 Jets

Jets are reconstructed using the anti- k_T clustering algorithm [128] with a distance parameter $R = 0.4$, as implemented in the FASTJET package [129, 130]. The energy of the reconstructed jets is corrected in 3 steps: L1FastJet (for pileup/underlying event subtraction), L2 (for relative corrections) and L3 for absolute scale corrections. For data an extra residual correction is included in the absolute scale correction.

Jets with $P_T > 30$ GeV and $|\eta| < 5$ and passing the so called PF-loose requirements are selected. PF-loose requirements are sets of certain conditions that are listed in Table 4.8. Jets that are within $\Delta R < 0.3$ of one of the identified leptons are excluded from the jet sample.

4.2.5 V-tag jets

Hadronically decaying gauge boson candidates are reconstructed using the anti- k_T clustering algorithm [128] with a distance parameter $R = 0.8$ using the Puppi algo-

Variables	$ \eta < 2.7$	$ \eta < 2.4$	$2.7 < \eta \leq 3.0$	$ \eta > 3.0$
Neutral Hadron Fraction	< 0.99	-	-	-
Neutral EM Fraction	< 0.99	-	< 0.90	< 0.90
Number of Constituents	> 1	-	-	-
Number of Neutral Particles	-	-	> 2	> 10
Charged Hadron Fraction	-	> 0	-	-
Charged Multiplicity	-	> 0	-	-
Charged EM Fraction	-	< 0.99	-	-

Table 4.8: PF-loose Jet ID requirements based on the content of jets.

rithm [131]. The V -jets that are within $\Delta R < 1.0$ of one of the identified leptons are excluded. The V -tag jet mass is computed after employing the modified mass drop tagger algorithm to remove soft, wide-angle radiation from the jets [132, 133]. The N -subjettiness variable τ_N [134] is also employed to further isolate jets arising from hadronic decays of W or Z bosons.

The signal region is defined by requiring $\tau_{21} < 0.55$ and $65 \text{ GeV} < m_V < 105 \text{ GeV}$.

4.2.6 B-tagging

The selected jets are expected to be mostly coming from gluons or light-quarks due to initial state radiation. Thus, in order to suppress backgrounds coming from top quarks, events are vetoed if a b -tagged jet is found. Jets with P_T greater than 30 GeV and lying within the tracker fiducial region ($|\eta| < 2.4$) are considered as b -taggable. A jet is tagged as a b -jet candidate if its Combined Secondary Vertex (CSV) discriminator is greater than 0.5426. To define the top control region, the tight working point (CSV > 0.9535) is used.

4.2.7 Missing transverse energy

Missing transverse energy is estimated from the imbalance of the transverse momentum of all the reconstructed PF candidates. The standard PF P_T^{miss} using the Type-1 corrections [135] is used.

4.3 Event Selection

The event selection aims to identify events with one or two leptons and a Lorentz-boosted V boson produced with VBS topology. Candidate events with a tightly identified lepton with $P_T > 30\text{GeV}$ target the $\text{WV} \rightarrow \ell\nu V$ decays, characterized by a significant amount of missing transverse energy (P_T^{miss}) associated to the undetected neutrino. The Drell-Yan and QCD multi-jet background processes are reduced by requiring $P_T^{\text{miss}} > 50\text{GeV}$ ($P_T^{\text{miss}} > 80\text{GeV}$) in the muon (electron) final state.

Candidate events with two same flavor leptons of opposite charges with $P_T > 30\text{GeV}$ target the $\text{ZV} \rightarrow \ell\ell V$ decays. The candidate Z boson invariant mass is required to lie within 15GeV of the nominal Z boson mass.

Events are required to have at least one V -tagged jet with $P_T > 200\text{GeV}$, $|\eta| < 2.4$, and $65\text{ GeV} < m_V < 105\text{ GeV}$. In the case of multiple V candidates, the one with mass closest to the nominal W boson mass is selected. The events are required to contain at least two jets with $P_T > 30\text{GeV}$ and $|\eta| < 5.0$, and $\Delta R(j, V) > 0.8$. In the case of more than two jet candidates, the pair with the largest dijet mass is selected. The VBS topology is targeted by requiring a large dijet mass $m_{jj} > 800\text{GeV}$, and a large pseudorapidity separation $|\Delta\eta_{jj}| > 4.0$.

Events with three or more loosely identified leptons with $P_T > 20\text{GeV}$ and $|\eta| < 2.5$ (2.4) for electrons (muons) are rejected. Identification of b-quark jets with P_T greater than 30 GeV and lying within the tracker fiducial region ($|\eta| < 2.4$) is used to further reject top quark background events.

The longitudinal component of the neutrino momentum in $\text{WV} \rightarrow \ell\nu V$ events is estimated by constraining the mass of the lepton and neutrino system to be the nominal W boson mass [136]. The resulting quadratic equation is solved using \vec{p}_T^{miss} as an estimate of the neutrino \vec{p}_T .

Additional selection criteria are then used to enhance the sensitivity to aQGCs. Candidate events are required to have $z_V^* < 0.3$ and $z_W^* < 0.3$, where $z_V^* = |\eta_V - (\eta_{j1} + \eta_{j2})/2|/|\Delta\eta_{jj}|$ is the Zeppenfeld variable [137], η_V is the pseudorapidity of a gauge boson, and η_{j1} and η_{j2} are the pseudorapidities of the leading and sub-leading jet, respectively. In addition, events are required to have $\vartheta > 1.0$ where $\vartheta = \min(\min(\eta_W, \eta_V) - \min(\eta_{j1}, \eta_{j2}), \min(\eta_{j1}, \eta_{j2}) - \min(\eta_W, \eta_V))$ is the so called boson centrality.

Statistical analysis of the event yields is performed with a fit to the mass distribu-

tion of the WV or ZV system. The mass distributions are binned as follows: $m_{WV} = [600, 700, 800, 900, 1000, 1200, 1500, 2000, \infty]$. The distributions of m_{WV} and m_{ZV} in the signal region are shown in Figure 4.4. The data yield together with the SM expectation for the different processes is given in Table 4.9. The expected yields of the background processes are obtained from the fit to the Asimov dataset for the SM only hypothesis.

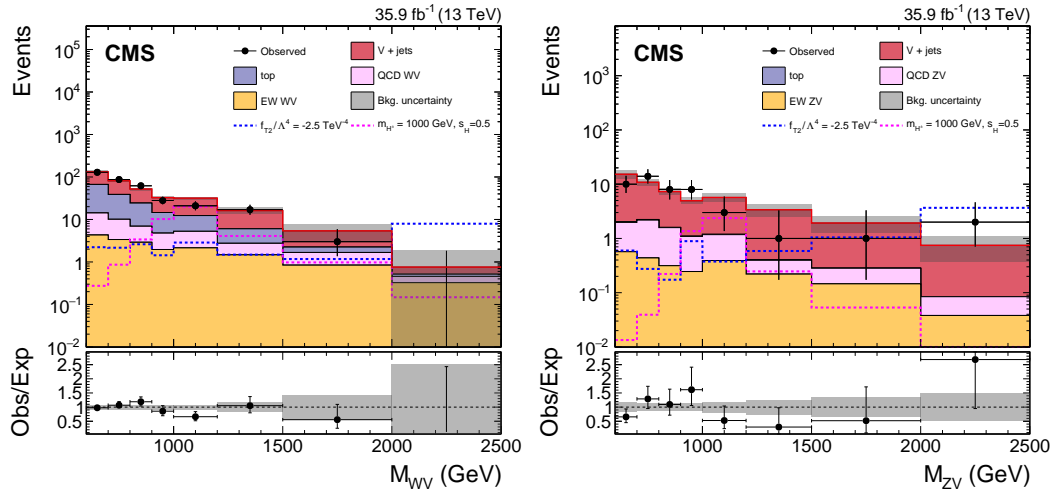


Figure 4.4: Distributions of m_{WV} (left) and m_{ZV} (right) in the signal region. The gray bands include uncertainties from the predicted yields. The histograms for other backgrounds include the contributions from QCD initiated dibosons, top, W+jets, and Drell–Yan processes. The overflow is included in the last bin. The bottom inset in each figure shows the ratio of the number of events observed in data to that of the total background prediction.

4.4 Background Estimation

A combination of data-driven methods and detailed simulated studies to estimate background contributions is used. In all cases where simulation is used, events are reweighted to correct for the pileup, lepton and trigger efficiencies to agree with the data distribution. The following background processes are considered: QCD initiated di-boson, top, W+jets, and Drell–Yan processes.

Final state	WV	ZV
Data	347 ± 16	47 ± 7
$V + \text{jets}$	187 ± 21	41.2 ± 6.1
top	120 ± 18	0.16 ± 0.04
SM QCD VV	28 ± 10	6.4 ± 2.2
SM EW VV	17 ± 2	2.4 ± 0.4
Total bkg.	352 ± 21	50.1 ± 5.9
$f_{T2}/\Lambda^4 = -0.5, -2.5 \text{ TeV}^{-4}$	22 ± 1	7.6 ± 0.6
$m_H = 500 \text{ GeV}, s_h = 0.5$	40 ± 1	4.3 ± 0.1

Table 4.9: Expected yields from various background processes in WV and ZV final states. The statistical and systematic uncertainties are shown. The aQGC and charged higgs signal yields are also shown.

4.4.1 Diboson

Simulation is used for estimating this process, as described in Section 4.1. The expected contribution of this process in the signal region is small. The theoretical uncertainties in the prediction from variation of the renormalization and factorization scales are 35%. The uncertainty from the PDFs is 7%.

4.4.2 Top

Simulation is used for estimating this process, as described in Section 4.1. The top background prediction is verified in a top enriched control region where the full signal selection is applied, except the b-tagging requirements are reverted. Figure 4.5 shows the distributions of few kinematic variables in this control region. Normalization uncertainty of 10% is assigned to the top background as good agreement between data and predictions is observed.

4.4.3 W+jets

The W+jet background contribution is estimated from data using a W+jets enriched control region defined by selecting events with $40 \text{ GeV} < m_V < 65 \text{ GeV}$ or $105 \text{ GeV} < m_V < 150 \text{ GeV}$, where the full signal selection is applied. Figure 4.6 shows the distributions of jet kinematic variables in this sideband region where W+jets predictions are taken from the simulation. Similarly, Figure 4.7 shows the distributions of

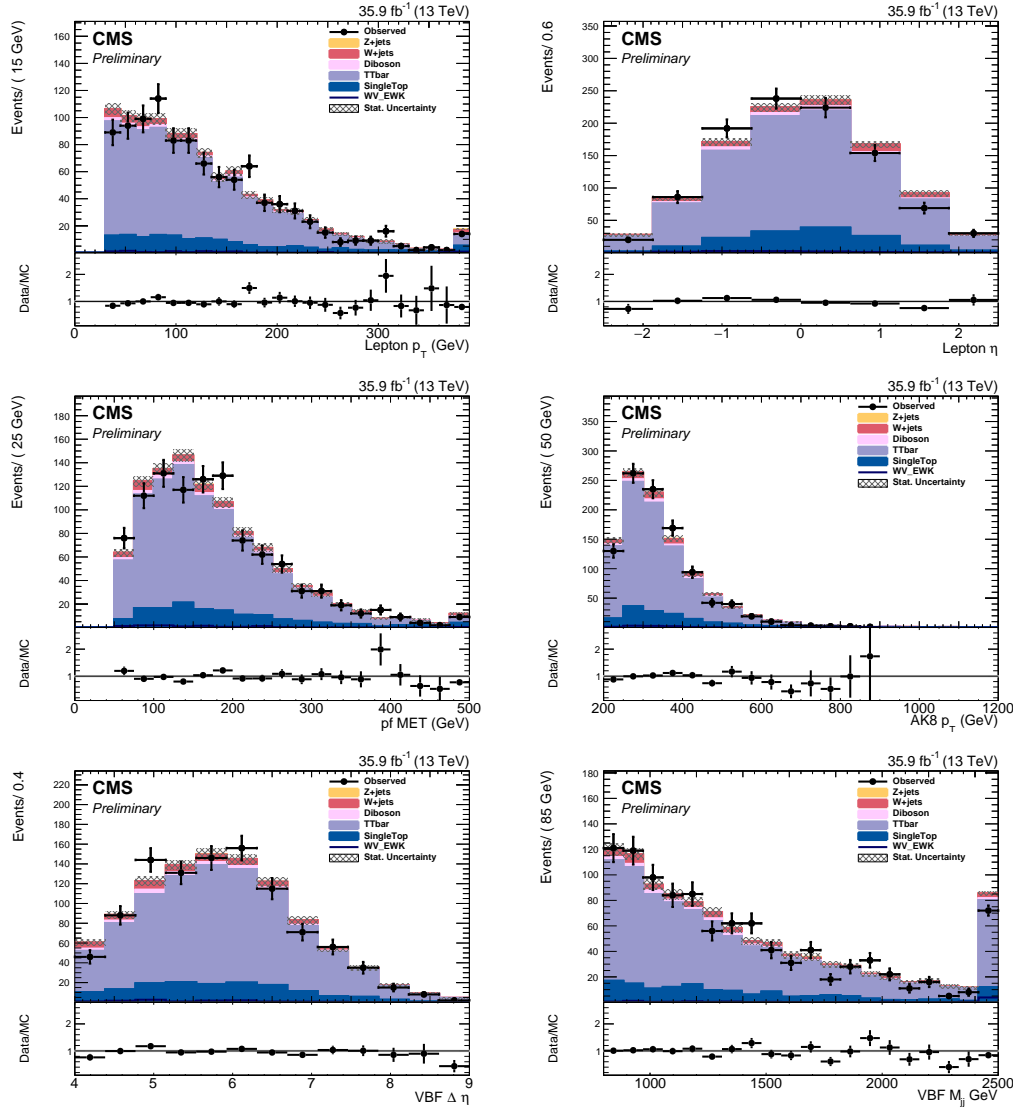


Figure 4.5: Kinematic distributions in the top background control region. The hatched bands include statistical uncertainties from the predicted yields.

the lepton, P_T^{miss} , and V jet kinematic distributions. Generally good data-simulation agreement is seen. However, the W+jets MC sample is generated in H_T bins at LO accuracy (see Table 4.4). The number of available simulated events are not large enough for some H_T bins resulting in large statistical uncertainties in the MC predictions. Therefore, the W+jets predictions from the simulation are not used in the statistical analysis of the event yields.

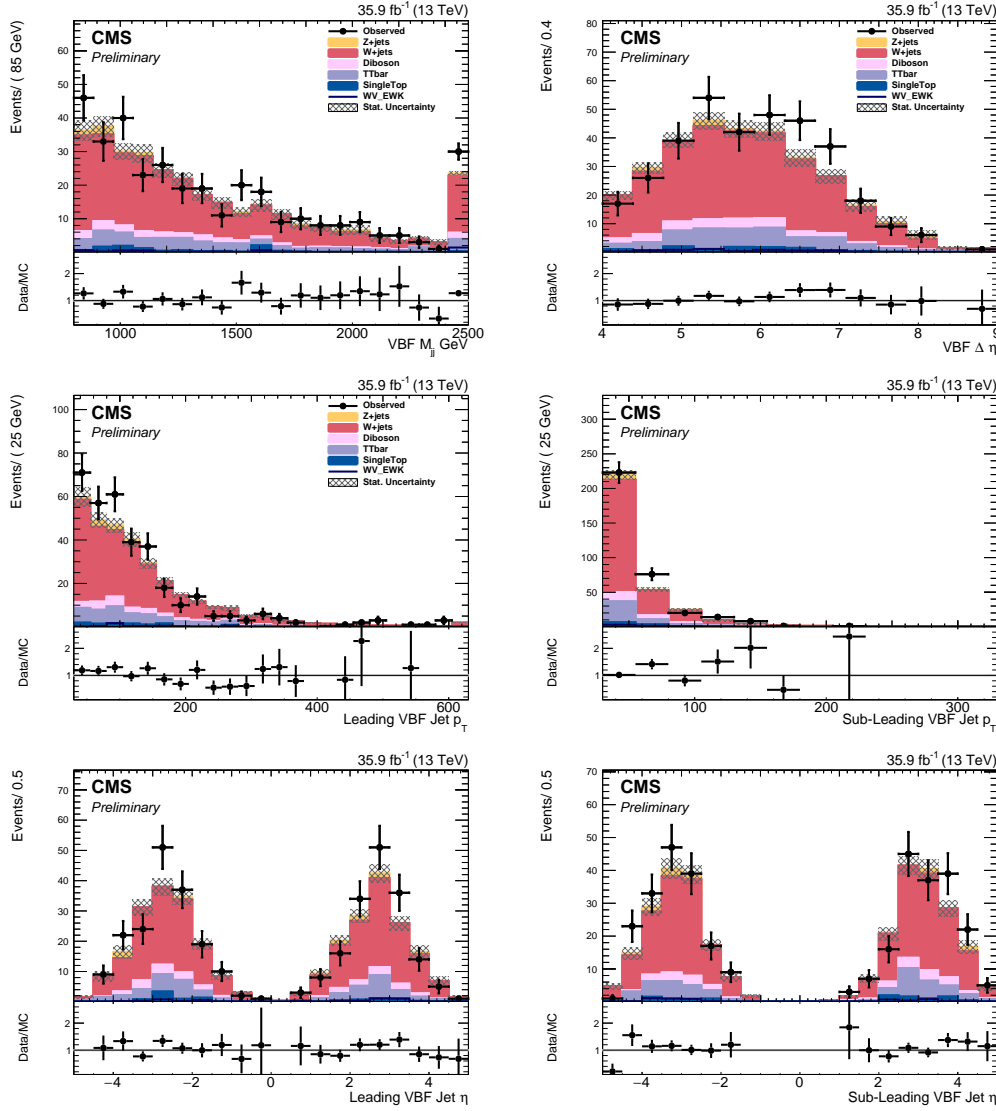


Figure 4.6: Kinematic distributions in the W+jets background sideband region. W+jets predictions are taken from the simulation. The hatched bands include statistical uncertainties from the predicted yields.

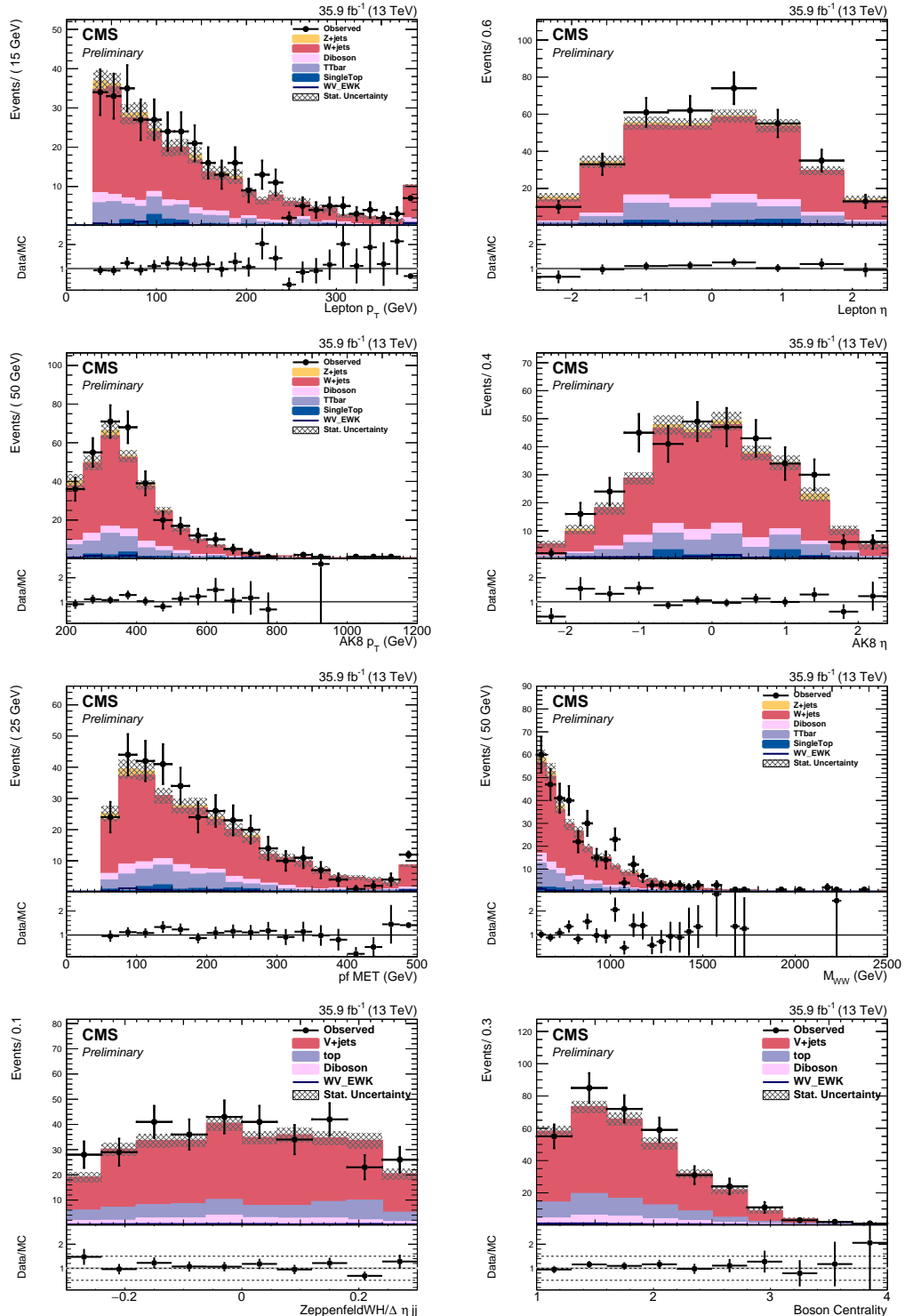


Figure 4.7: Kinematic distributions in the $W+jets$ background sideband region. $W+jets$ predictions are taken from the simulation. The hatched bands include statistical uncertainties from the predicted yields.

The background estimation described below closely follows the method used in previous inclusive searches in WV final state [138, 139]. More detailed description of the method can be found in the references. The shape and normalization of the W+jets background prediction are estimated from data in the sideband region defined above. The aQGC and charged Higgs limits are extracted from a fit (using the CMS Higgs combination tools) to the m_{WV} distribution in the WV final state as shown in Figure 4.4. The prediction of the W+jets background used in the signal extraction is obtained by performing a separate fit to the m_{WV} distribution in the sideband region. The extrapolation factors (denoted as alpha-ratio values) to the signal region are obtained from the W+jets simulation as a function of the m_{WV} variable as described below. The shapes of the $t\bar{t}$, single top, diboson, and W+jets processes are represented by parametric shapes extracted from simulation. The following parametric functions are used:

$$\text{Main function } f_{ExpTail} = \exp\left(\frac{-x}{a+bx}\right)$$

$$\text{Alternate Function } f_{Exp} = \exp(cx)$$

The fits to the corresponding MC predictions are shown in Figure 4.8. The shown error band is determined by evaluating the fitted functions many times for several points along the x axis with the fitted parameters randomized according to their resulting uncertainties. The extracted fit parameters are summarized in Table 4.10. These parametric templates are then used to fit the m_{WV} distribution in the sideband region. The normalization and shape of the W+jets process is floated in this fit. The other background processes are fixed to the SM predictions. The resulting fit is shown in Figure 4.9.

The contribution of the W+jets process in the signal region is obtained using the alpha-ratio-method [138, 139]. The alpha-ratio values extrapolate the W+jets contribution from the sideband region to the signal region as a function of m_{WV} using simulation. The resulting distribution is shown in Figure 4.10. The statistical uncertainties are propagated to the result. The final W+jets prediction in the signal region is shown in Figure 4.11.

The statistical uncertainties from the fits in the sideband region are propagated to the final prediction. The statistical uncertainty in the alpha-ratio values due to limited number of simulated events are also propagated to the result. The W+jets

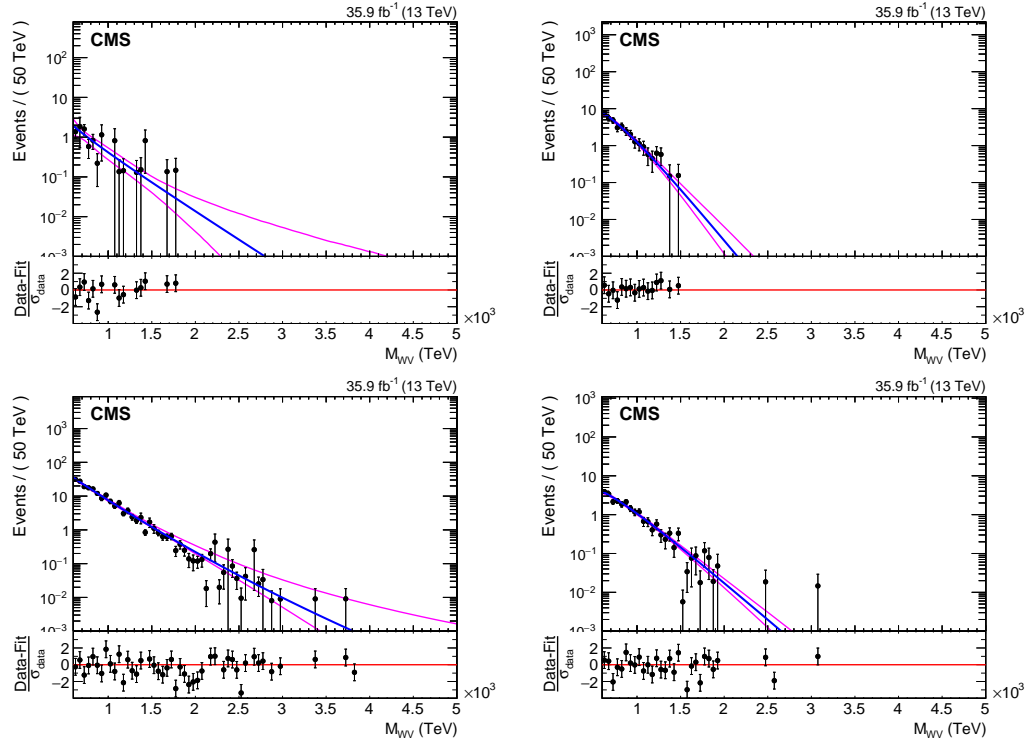


Figure 4.8: MC-data and fit shape m_{WV} distributions in the sideband region. From top to bottom: single top, $t\bar{t}$, W+jets and dibosons.

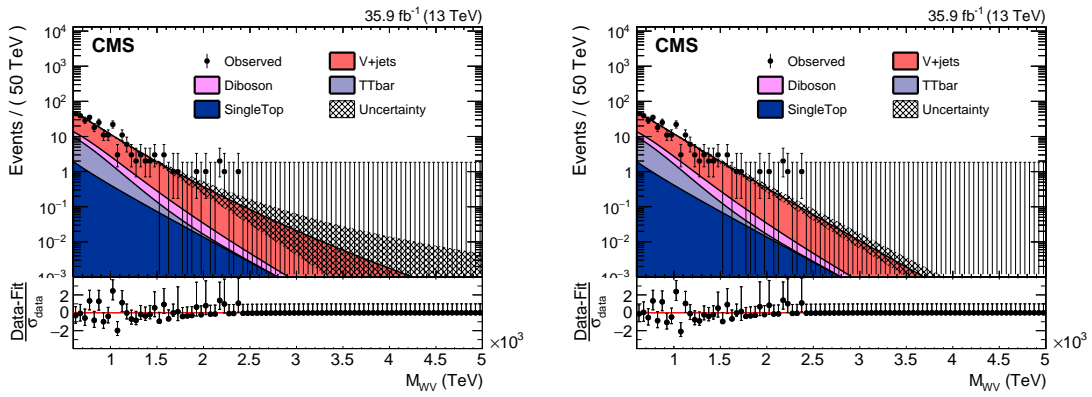


Figure 4.9: The data distribution and the corresponding fit of the m_{WV} distribution in the sideband region for the nominal parametric function (left) and a modified parametric function (right).

parameter	Values
W+jets, $f_{ExpTail}$	
a	0.0360242 ± 0.0259207
b	196.282 ± 69.6708
N	240.834 ± 17.9165
W+jets (alternate function), f_{Exp}	
c	$-0.00349426 \pm 0.000258006$
N	240.69 ± 17.9176
Diboson, f_{ExpN}	
c	$-0.00415878 \pm 0.000478786$
n	-203.63 ± 424.762
N	27.4306 ± 1.10149
TTbar, f_{ExpN}	
c	$-0.00671012 \pm 0.00124636$
n	-983.791 ± 914.875
N	42.0095 ± 2.51186
Single Top, f_{ExpN}	
c	$-0.0026518 \pm 0.00234551$
n	1045.48 ± 2235.03
N	10.5114 ± 2.11656

Table 4.10: Extracted fit parameters for the functions describing the m_{WV} distributions.

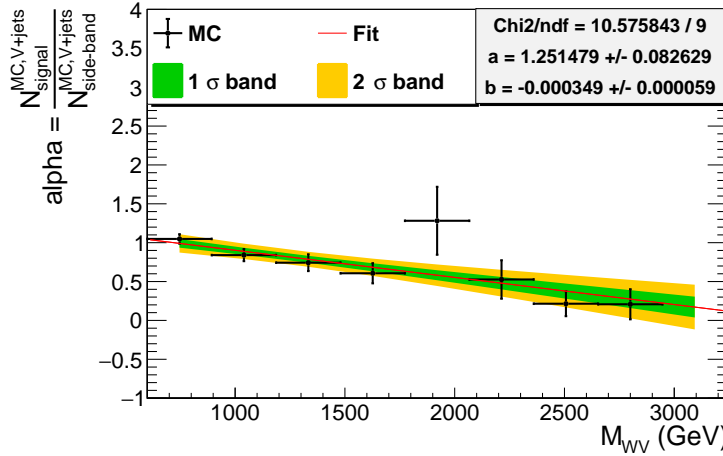


Figure 4.10: Alpha-ratio value (ratios of the W+jets MC contribution in the signal region to the sideband region) distribution. Red line is the fitted function used in the result.

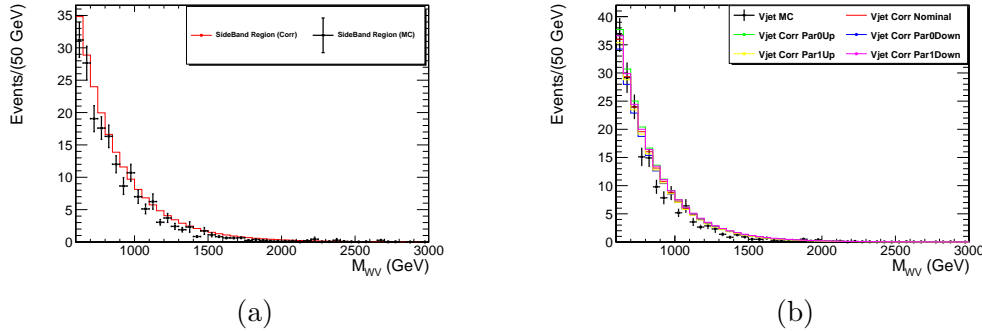


Figure 4.11: Comparison of the W+jets predictions using simulation (red) and the data-driven estimation in the sideband (left) and signal regions (right). The uncertainty band shows the fit uncertainty.

prediction is also performed with an alternative function as shown above (Figure 4.9) and the difference from the nominal prediction is taken as a systematic uncertainty.

The normalization of the W+jets background in the sideband region is cross-checked by performing a fit to the m_V distribution, excluding the signal region. The following parametric functions are used:

$$\mathbf{V+jets} \quad f_{User1} = \left(1 - \frac{x}{500}\right)_0^p / \left(\frac{x}{500}\right)_1^p$$

$$\mathbf{V+jets (alternative function)} \quad f_{ErfExp} = e^{(cx)} \cdot \frac{1}{2} \cdot \left(1 + Erf\left(\frac{x-offset}{width}\right)\right)$$

$$\mathbf{TTbar} \quad f_{2Gaus-ErfExp} = f_1 \times \left[e^{(cx)} \cdot \frac{1}{2} \cdot \left(1 + Erf\left(\frac{x-offset}{width}\right)\right) \right] + f_2 \times Gaus(x, \mu_1, \sigma_1) + f_3 \times Gaus(x, \mu_2, \sigma_2)$$

$$\mathbf{Single Top, Diboson} \quad f_{ExpGaus} = f_1 \times e^{(cx)} + Gaus(x, \mu, \sigma)$$

The resulting shapes are shown in Figure 4.12. The shown error band is determined by evaluating the fitted functions many times for several points along the x axis with the fitted parameters randomized according to their resulting uncertainties. The extracted fit parameters are summarized in Table 4.11. These templates are then used to fit the m_V distribution, excluding the signal region. The normalization and shape of the W+jets process is floated in the fit. The other background processes are fixed to the SM predictions. The resulting fit is shown in Figure 4.13. The resulting normalization of the W+jets distribution agrees with the normalization obtained from the m_{WV} fit.

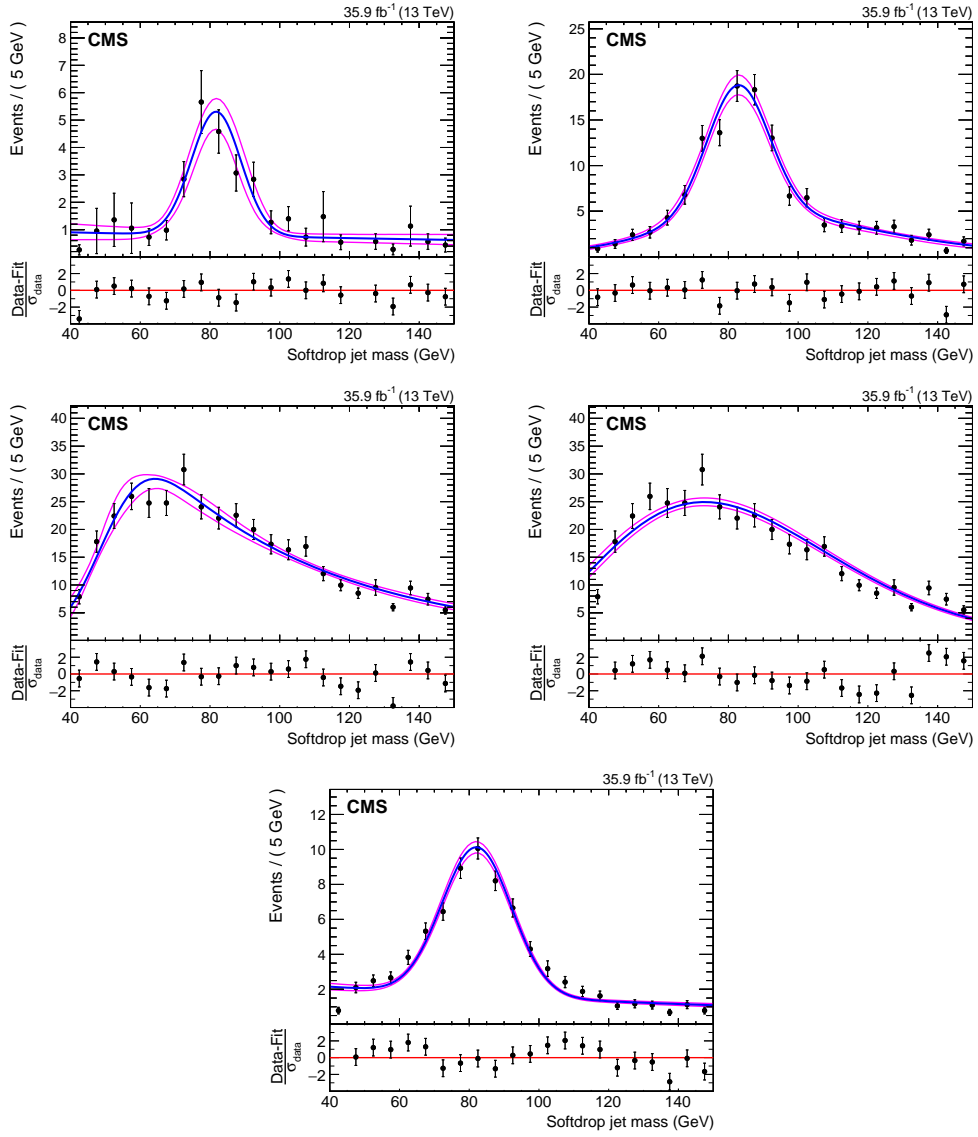


Figure 4.12: MC fit distribution for m_V . Top Left: Single top, Top right: TTbar, Middle left: Wjets with f_{ErfExp} , Middle right: Wjets with f_{User1} , Bottom: Diboson distribution

parameter	Values
W+jets (f_{User1})	
p_0	25.0479 ± 0.885452
p_1	-4.03783 ± 0.328605
N	478.191 ± 35.4216
W+jets (alternate function, f_{ErfExp})	
c	$-0.0228734 \pm 0.00217427$
offset	50.9183 ± 2.56036
width	13.7415 ± 3.89626
N	460.073 ± 34.2282
Diboson, $f_{ExpGaus}$	
f_1	0.452621 ± 0.0175585
c	$-0.00625601 \pm 0.00115951$
μ	82.3131 ± 0.39325
σ	$10 \pm 9.41247e-07$
N	87.2154 ± 1.89749
TTbar, $f_{2Gaus,ErfExp}$	
f_1	0.320894 ± 0.0891809
c	$-0.0254783 \pm 0.00692614$
offset	79.35 (constant)
width	30.1227 ± 5.73131
f_2	0.67125 (constant)
μ_1	82.7893 ± 0.609335
σ_1	8.51989 ± 0.780058
f_3	1.0 (constant)
μ_2	$\mu_1 + 6.9129$
σ_2	$\sigma_1 + 3.6819$
N	152.598 ± 4.8036
Single-Top, $f_{ExpGaus}$	
f_1	0.471434 ± 0.080531
c	$-0.00367233 \pm 0.00476394$
μ	82.6023 ± 1.16547
σ	8.25865 ± 1.01946
N	35.5749 ± 2.98679

Table 4.11: Extracted fit parameters for the functions describing the m_V distributions.

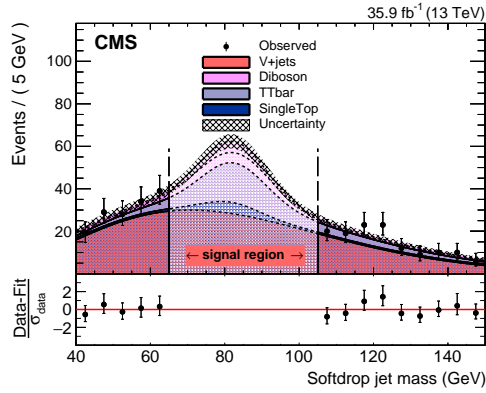


Figure 4.13: Result of the normalization fit in the m_V spectrum.

The background estimation is validated using a reduced sideband region and then checking the data-prediction agreement in the $105 \text{ GeV} < m_{WV} < 125 \text{ GeV}$ sideband region. The contribution of the $W+jets$ process is estimated in $105 \text{ GeV} < m_{WV} < 125 \text{ GeV}$ sideband region by repeating the background estimation above using a reduced sideband region given by requiring $40 \text{ GeV} < m_V < 65 \text{ GeV}$ or $125 \text{ GeV} < m_V < 150 \text{ GeV}$. Figure 4.14 shows (left) that the prediction of the background processes in $105 \text{ GeV} < m_{WV} < 125 \text{ GeV}$ sideband region is in good agreement with the data. For comparison, the predictions taken from simulation are also shown (right).

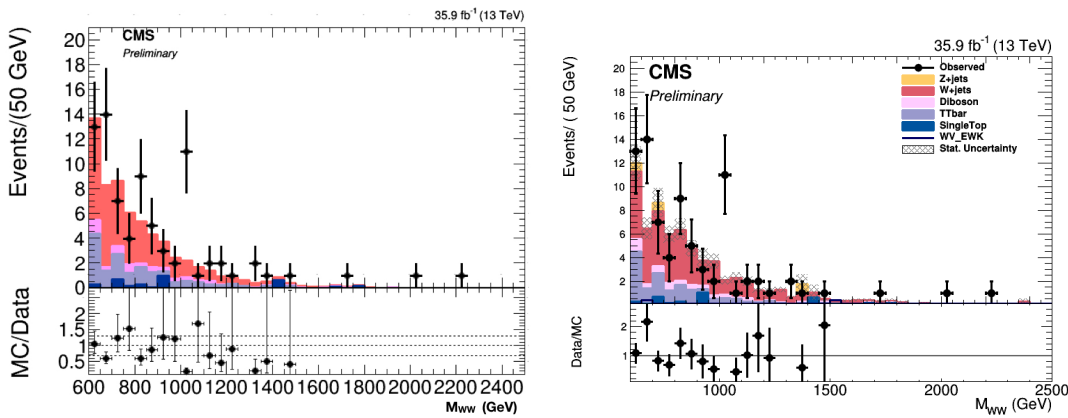


Figure 4.14: The data and predicted m_{WV} distribution obtained from the alpha-ratio method (left) and simulation (right).

4.4.4 Z+jets

The Z+jets background process prediction in the ZV final state is performed using the alpha-ratio method described above. The methods to obtain the prediction and the corresponding systematic uncertainties are identical to what was done for the W+jets prediction in the WV final state. Figure 4.15 shows the corresponding fit of the m_{ZV} distribution in the sideband region in the ZV final state.

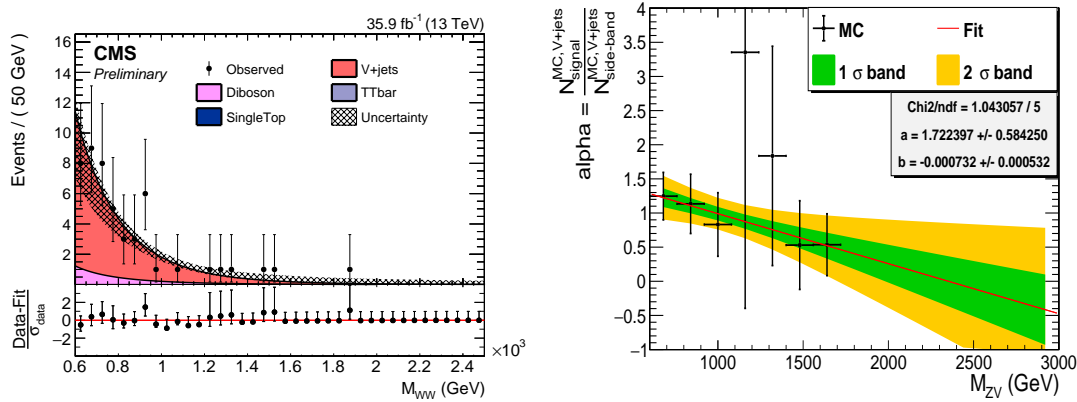


Figure 4.15: The data distribution and the corresponding fit of the m_{ZV} distribution in the sideband region (left) and alpha-ratio value distribution (right).

4.5 Systematic Uncertainty

In the following the systematic uncertainties which are taken into account in the fit to the m_{WV} and m_{ZV} shapes are listed. Uncertainties which do not only influence the overall normalization (e.g. the uncertainty in the luminosity measurement), but also the distribution of relevant kinematic observables (e.g. the uncertainty in the jet energy scale), are treated as shape uncertainties. The shape variation is included in the combine tool by providing the histogram templates shifted up and down by one standard deviation. For each source of uncertainty, the impact in different bins of the final distribution is thus considered fully correlated, while independent sources of uncertainty are treated as uncorrelated.

4.5.1 Luminosity

The assigned uncertainty to the integrated luminosity measurement for the data set used in this analysis is 2.5%.

4.5.2 Trigger, lepton reconstruction and identification efficiencies

Discrepancies in the lepton reconstruction and identification efficiencies between data and simulation are corrected by applying to all MC samples data-to-simulation scale factors measured using $Z/\gamma^* \rightarrow \ell^+ \ell^-$ events in the Z peak region [122] that are recorded with unbiased triggers. These factors depend on the lepton P_T and η and are within 1-2% for electrons and muons. The uncertainty in the determination of the trigger efficiency leads to an uncertainty smaller than 1% in the expected signal yield.

4.5.3 Jet energy scale and resolution

The uncertainty in the calibration of the jet energy scale (JES) and resolution (JER) [140] directly affects the acceptance of the requirement < 2 jets, the E_T^{miss} computation, and all the cuts related to jets. The estimate of the jet energy scale uncertainty is performed varying the jet energy scale up and down by 1σ [141]. The variation corresponds to a simple re-scaling of the jet four-momentum as follows: $P \rightarrow P \cdot (1 \pm \delta P_T^{\text{JES}} / P_T)$, where δP_T^{JES} is the absolute uncertainty on the jet energy scale which is parametrized as function of the P_T and η of the jet.

A similar strategy is performed to evaluate the systematic related to the jet energy resolution. In order to reproduce in MC the jet resolution measured in data the momentum of jets used in this analysis is smeared as

$$p_T \rightarrow \max [0, p_T^{\text{gen}} + c_{\pm 1\sigma} \cdot (p_T - p_T^{\text{gen}})] \quad (4.3)$$

in which $c_{\pm 1\sigma}$ are the data-to-MC scale factors shifting the central value by $\pm 1\sigma$ [141].

4.5.4 V tagging efficiency

For the processes estimated from simulation, the uncertainty in the efficiency of the V tagging requirements is estimated to be 8% in the signal region [142]. The signal region is defined by requiring $\tau_{21} < 0.55$ and $65 \text{ GeV} < m_V < 105 \text{ GeV}$.

4.5.5 Pileup

MC samples are re-weighted with 69.2 mb as MinBias cross section to reproduce the pileup conditions observed in data. To compute the uncertainty related to this re-weighting procedure, we shift the mean of the distribution of real interaction in MC by the suggested value [143] of 5%. The variation of the final yields induced by this procedure is about 5% in MC estimated processes.

4.5.6 MC statistics

For the processes estimated from simulation, the available statistics of the MC sample limits the precision of the modeling, and is therefore taken as a systematic uncertainty. Similarly, the backgrounds estimated from data are limited by the available statistics in the corresponding control samples. Therefore, for these uncertainties, the same treatment is used as in the case of MC-driven backgrounds.

4.5.7 Theoretical uncertainties

The predictions of the SM EW and QCD diboson background, and aQGC/Higgs signal processes are taken from simulation. The theoretical Uncertainties in the normalization are derived from variations of the QCD scale, α_s and parton distribution functions (PDFs) variations [144, 145, 146, 49, 147]. The PDF and α_s uncertainties for signal and background processes are estimated from the standard deviation of weights from the replicas provided in the NNPDF3.0 parton distribution set [121]. The procedure for estimating uncertainties arising from Parton Distribution Functions (PDF uncertainties) follows the recommendations as described in paper “*PDF4LHC recommendations for LHC Run II*” [148].

Figure 4.16 shows the nominal and the up/down one standard deviation predictions for the QCD scale (left) and PDF uncertainties (right) for the SM EW (top) and SM QCD (bottom) diboson background predictions. The QCD scale uncertainties are up

to 20% for the signal normalization (depending on the kinematic region) and 40% for the QCD initiated diboson background normalization. The uncertainty in the PDF results in up to 10% variation for the signal and background normalization.

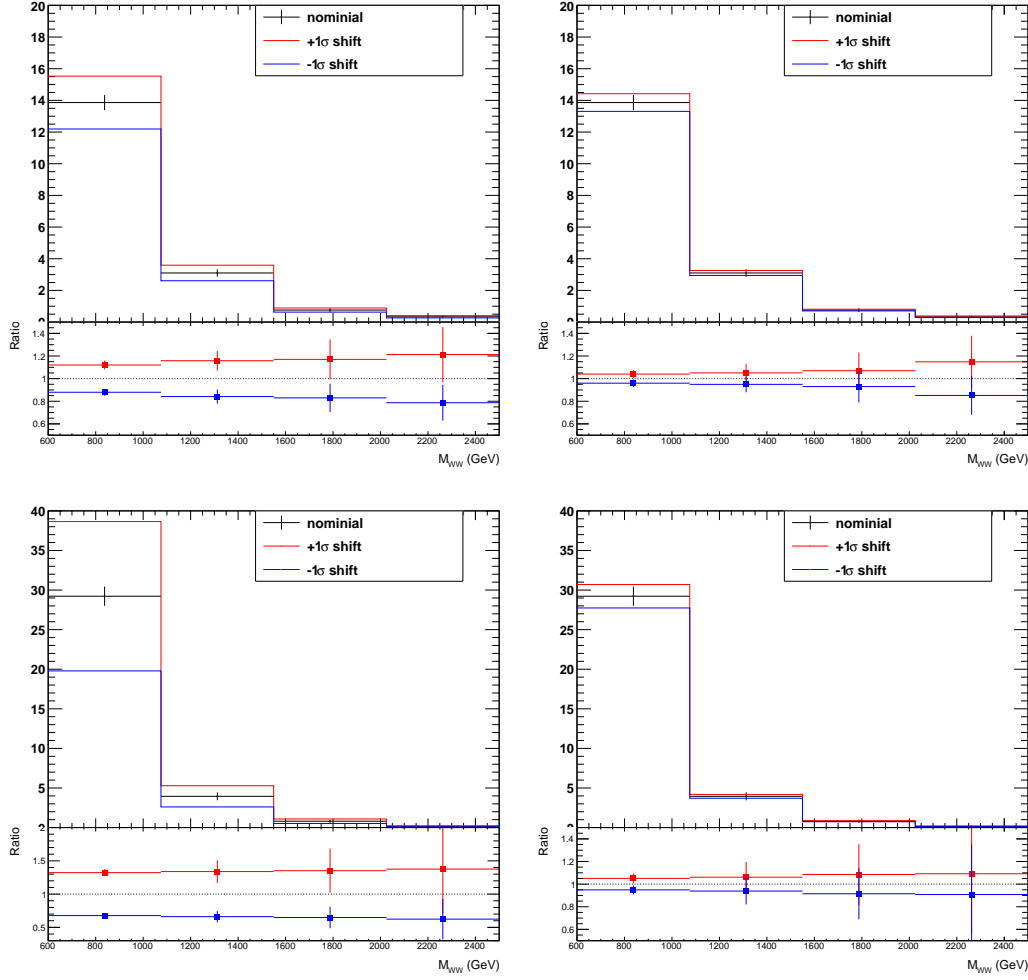


Figure 4.16: Nominal and up/down one standard deviation predictions for the SM EW (top) and SM QCD (bottom) background processes showing the effects of the QCD scale (left) and PDF (right) uncertainties.

4.5.8 $V+jets$

The statistical uncertainties from the fit in the sideband region are propagated to the final prediction. The fit normalization uncertainty is 15%. The fit function is

modeled using a functional shape of form $f = \exp[-m/(c_0 + c_1 \cdot m)]$ in the control region fit. The uncertainties in the fit parameters - c_0 and c_1 - are treated as nuisance parameters in the combine fit and affect the shape of the background prediction. Figure 4.17 shows the nominal and the up/down one standard deviation predictions. The statistical uncertainty in the alpha-ratio values due to limited number of simulated events are also propagated to the result.

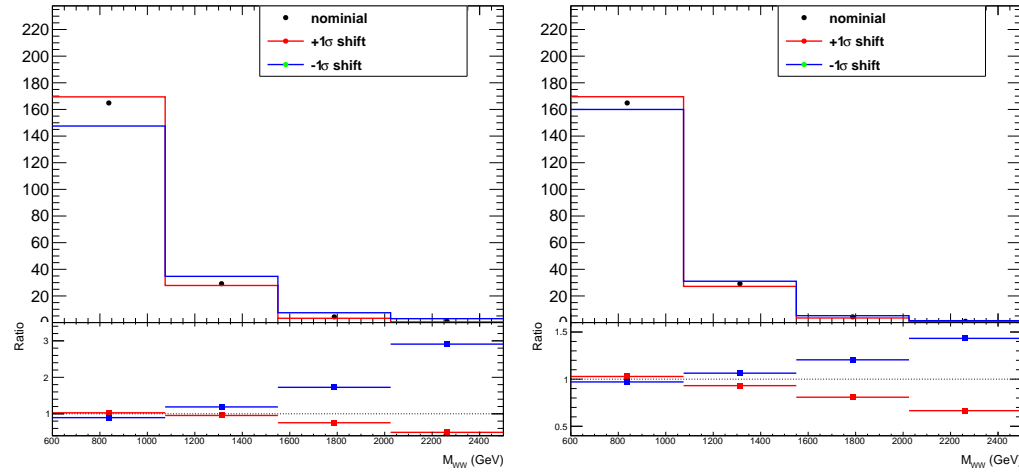


Figure 4.17: Nominal and up/down one standard deviation predictions of the $V + \text{jets}$ processes for the c_1 (left) and c_0 (right) fit parameters.

The $V + \text{jets}$ prediction is also performed with an alternative function ($f = \exp[-m/c_0]$). The prediction obtained with this function is well within the uncertainties of the nominal prediction as shown in Figure 4.18. For completeness, the difference from the nominal prediction is symmetrized and taken as a systematic uncertainty. The impact of this uncertainty is negligible (see Figure 4.19 where this uncertainty ranks 18).

4.5.9 Top

Simulation is used for estimating this process, as described in Section 4.1. The top background prediction is verified in a top enriched control region where the full signal selection is applied, except the b-tagging requirements are reverted. Normalization uncertainty of 10% is assigned to the top background based on the agreement between data and prediction in the control region.

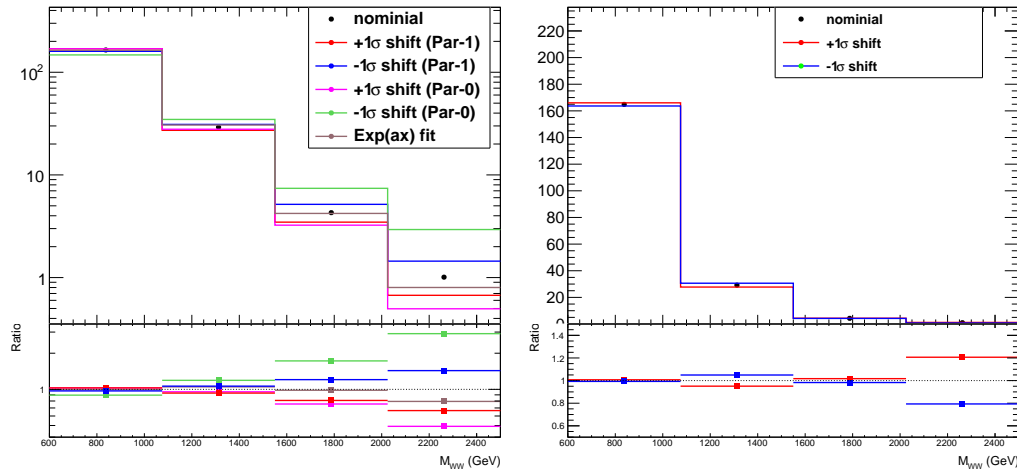


Figure 4.18: Predictions of the $V + \text{jets}$ processes for the $f = \exp[-m/c_0]$ functions compared to the nominal prediction (left). The fit uncertainties with this functions are also shown (right).

4.5.10 Summary

All of the systematic uncertainties on normalizations are given a log-normal distribution. A summary of the relative systematic uncertainties in the estimated signal and background yields is shown in Table 4.12. The pulls and impacts of the systematic

Source	Signal	$V + \text{jets}$	SM EW	QCD VV	top
Integrated luminosity	2.5	—	2.5	2.5	—
Lepton efficiency	1.0-2.0	—	1.0-2.0	1.0-2.0	—
Jet momentum scale	shape	—	shape	shape	shape
Lepton momentum scale	shape	—	shape	shape	shape
b tagging	2.0	—	2.0	2.0	3.0
V tagging	8.0	—	8.0	8.0	—
QCD scale	20	—	20	40	—
PDF unc.	15	—	10	10	—
bkg. normalization	—	10	—	—	10
$V + \text{jets}$ shape	—	shape	—	—	—
Jet/MET resolution	4.0	—	3.0	2.0	—
Pileup modeling	5.0	—	4.0	4.0	—
Limited MC stat.	shape	—	shape	shape	shape

Table 4.12: Relative systematic uncertainties in the estimated signal and background yields in units of percent.

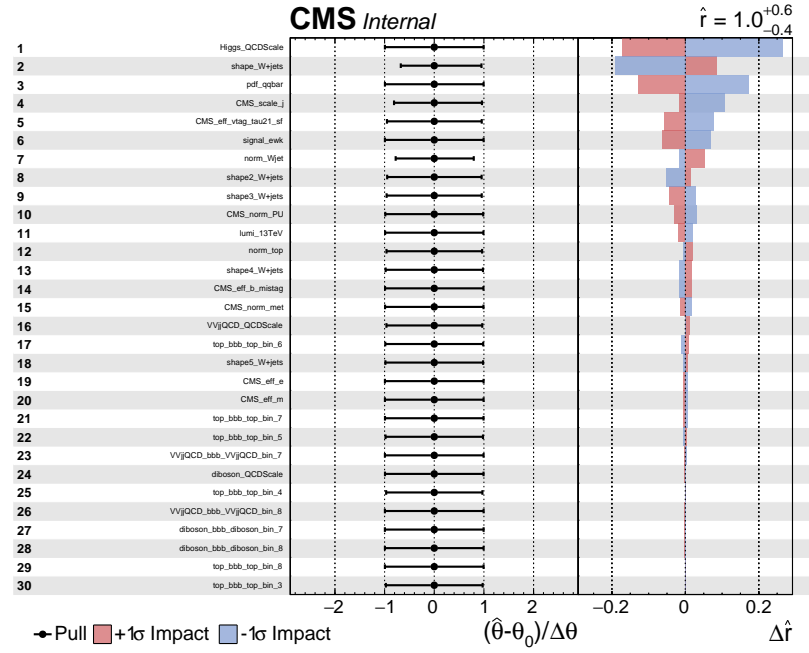


Figure 4.19: Impacts and pulls of the systematic uncertainties for the Asimov dataset in the WV final state. The impacts are shown for a doubly charged Higgs with a mass of 2000GeV.

uncertainties for the Asimov dataset are shown in Figure 4.19 in the WV final state. The signal used in the fit is a doubly charged Higgs with a mass of 2000GeV. The main experimental systematic uncertainties are related to the uncertainties in the W+jets background estimation, uncertainties in the jet energy scale and resolution, and the uncertainty in the efficiency of the V tagging requirements.

4.6 Results

The events in the signal region are used to constrain aQGCs in the effective field theory framework. Nine independent charge conjugate and parity-conserving dimension-8 effective operators are considered [93]. The dimension-8 operators are the following:

$$\begin{aligned} L_{S,0} &= \left[(D_\mu \Phi)^\dagger D_\nu \Phi \right] \times \left[(D_\mu \Phi)^\dagger D_\nu \Phi \right] \\ L_{S,1} &= \left[(D_\mu \Phi)^\dagger D^\mu \Phi \right] \times \left[(D_\nu \Phi)^\dagger D_\nu \Phi \right] \\ L_{M,0} &= Tr[\hat{W}_{\mu\nu} \hat{W}^{\mu\nu}] \times \left[(D_\beta \Phi)^\dagger D^\beta \Phi \right] \end{aligned}$$

$$\begin{aligned}
L_{M,1} &= \text{Tr}[\hat{W}_{\mu\nu}\hat{W}^{\nu\beta}] \times [(D_\beta\Phi)^\dagger D^\mu\Phi] \\
L_{M,6} &= [(D_\mu\Phi)^\dagger \hat{W}_{\beta\nu}\hat{W}^{\beta\nu}D^\mu\Phi] \\
L_{M,7} &= [(D_\mu\Phi)^\dagger \hat{W}_{\beta\nu}\hat{W}^{\beta\mu}D^\nu\Phi] \\
L_{T,0} &= \text{Tr}[W_{\mu\nu}W^{\mu\nu}] \times \text{Tr}[W_{\alpha\beta}W^{\alpha\beta}] \\
L_{T,1} &= \text{Tr}[W_{\alpha\nu}W^{\mu\beta}] \times \text{Tr}[W_{\mu\beta}W^{\alpha\nu}] \\
L_{T,2} &= \text{Tr}[W_{\alpha\mu}W^{\mu\beta}] \times \text{Tr}[W_{\beta\nu}W^{\nu\alpha}]
\end{aligned}$$

Each operator is scaled by the corresponding Wilson coefficient. A non-zero aQGC enhances the production cross section at large masses of the system of the gauge boson pair as can be seen in Figure 4.4. Statistical analysis of the event yields is performed with a fit to the mass distribution of the WV or ZV system. The SM EW production is treated as a background in the statistical analysis. The observed and expected 95% confidence level (C.L.) limits on the aQGC parameters are obtained using a profile likelihood test statistic [149, 150, 151].

The expected yields for different values of the aQGC parameters are obtained using the reweighting feature of the MadGraph package. The expected ratio of the aQGC and MS EW yields as a function of the aQGC parameter is fitted with a parabolic function. This is done for each bin of the mass distribution of the WV or ZV system as shown in Figure 4.20. The increase of the yield as a function of the anomalous coupling exhibits a quadratic behaviour and the fitted parabolic function is used to interpolate amongst the discrete coupling parameters of the simulated signals.

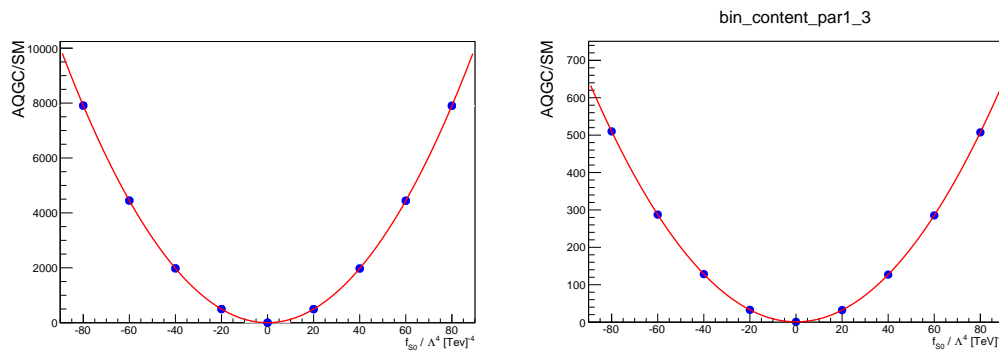


Figure 4.20: Yield ratios of the operator S_0 and the fitted quadratic interpolation for the most relevant bins used in the statistical analysis. The yields for the mass bins $m_{\text{WV}} = [2025, \infty]$ (left) and $m_{\text{WV}} = [1550, 2025]$ (right) are shown.

Table 4.13 shows the individual lower and upper limits obtained by setting all other aQGCs to zero using the WV final state. The reported values are the most stringent limits reported by the CMS Collaboration previously. The corresponding limits using the ZV final state are shown in Table 4.14. The combined limits are shown in Table 4.15.

	Observed limits (TeV ⁻⁴)	Expected limits (TeV ⁻⁴)
f_{S0}/Λ^4	[-2.6, 2.7]	[-4.0, 4.0]
f_{S1}/Λ^4	[-3.2, 3.3]	[-4.9, 4.9]
f_{M0}/Λ^4	[-0.66, 0.66]	[-0.95, 0.95]
f_{M1}/Λ^4	[-1.9, 2.0]	[-2.8, 2.8]
f_{M6}/Λ^4	[-1.3, 1.3]	[-1.9, 1.9]
f_{M7}/Λ^4	[-3.3, 3.2]	[-4.8, 4.8]
f_{T0}/Λ^4	[-0.11, 0.10]	[-0.16, 0.15]
f_{T1}/Λ^4	[-0.11, 0.12]	[-0.17, 0.17]
f_{T2}/Λ^4	[-0.27, 0.27]	[-0.38, 0.38]

Table 4.13: Observed and expected 95% C.L. limits on the coefficients for higher-order (dimension-8) operators in the effective field theory Lagrangian in WV final state.

	Observed limits (TeV ⁻⁴)	Expected limits (TeV ⁻⁴)
f_{S0}/Λ^4	[-37, 37]	[-29, 29]
f_{S1}/Λ^4	[-30, 30]	[-23, 23]
f_{M0}/Λ^4	[-6.9, 6.9]	[-5.1, 5.1]
f_{M1}/Λ^4	[-21, 21]	[-15, 15]
f_{M6}/Λ^4	[-14, 14]	[-10, 10]
f_{M7}/Λ^4	[-33, 33]	[-24, 24]
f_{T0}/Λ^4	[-1.3, 1.3]	[-0.95, 0.95]
f_{T1}/Λ^4	[-1.4, 1.4]	[-0.98, 0.99]
f_{T2}/Λ^4	[-3.1, 3.2]	[-2.3, 2.3]

Table 4.14: Observed and expected 95% C.L. limits on the coefficients for higher-order (dimension-8) operators in the effective field theory Lagrangian in ZV final state.

The exclusion limits on the charged Higgs bosons $\sigma_{\text{VBF}}(H^{\pm\pm}) \mathcal{B}(H^{\pm\pm} \rightarrow WW)$ and $\sigma_{\text{VBF}}(H^\pm) \mathcal{B}(H^\pm \rightarrow WZ)$ at 95% confidence level as functions of $m(H^\pm)$ and $m(H^{\pm\pm})$, respectively, for the WV final state are shown in Fig. 4.21 (top left and right). A

	Observed limits (TeV ⁻⁴)	Expected limits (TeV ⁻⁴)
f_{S0}/Λ^4	[−2.6, 2.7]	[−4.0, 4.0]
f_{S1}/Λ^4	[−3.2, 3.3]	[−4.9, 4.9]
f_{M0}/Λ^4	[−0.66, 0.66]	[−0.95, 0.95]
f_{M1}/Λ^4	[−1.9, 2.0]	[−2.8, 2.8]
f_{M6}/Λ^4	[−1.3, 1.3]	[−1.9, 1.9]
f_{M7}/Λ^4	[−3.3, 3.2]	[−4.8, 4.8]
f_{T0}/Λ^4	[−0.11, 0.10]	[−0.16, 0.15]
f_{T1}/Λ^4	[−0.11, 0.12]	[−0.17, 0.17]
f_{T2}/Λ^4	[−0.27, 0.27]	[−0.38, 0.38]

Table 4.15: Observed and expected 95% C.L. combined limits on the coefficients for higher-order (dimension-8) operators in the effective field theory Lagrangian in WV and ZV final states.

small intrinsic width for $H^{\pm\pm}$ and H^\pm is assumed. The exclusion limit on the charged Higgs $\sigma_{\text{VBF}}(H^\pm) \mathcal{B}(H^\pm \rightarrow WZ)$ at 95% confidence level as a function $m(H^\pm)$ for the ZV final state is shown in bottom left panel in Fig. 4.21. The Higgs bosons H^\pm and $H^{\pm\pm}$ are degenerate in mass (denoted as $m(5)$) at tree level and transform as a five-plet under the custodial symmetry in the GM model. The coupling depends on $m(5)$ and the parameter s_H , where s_H^2 denotes the fraction of the W boson mass squared generated by the vacuum expectation value of the triplets. The combination of the model-independent exclusion limits can be used to constrain the s_H - $m(5)$ plane by using the predicted cross sections at NNLO accuracy in the GM model [152]. The excluded s_H values as a function of $m(5)$ are shown in Fig. 4.21 (bottom right).

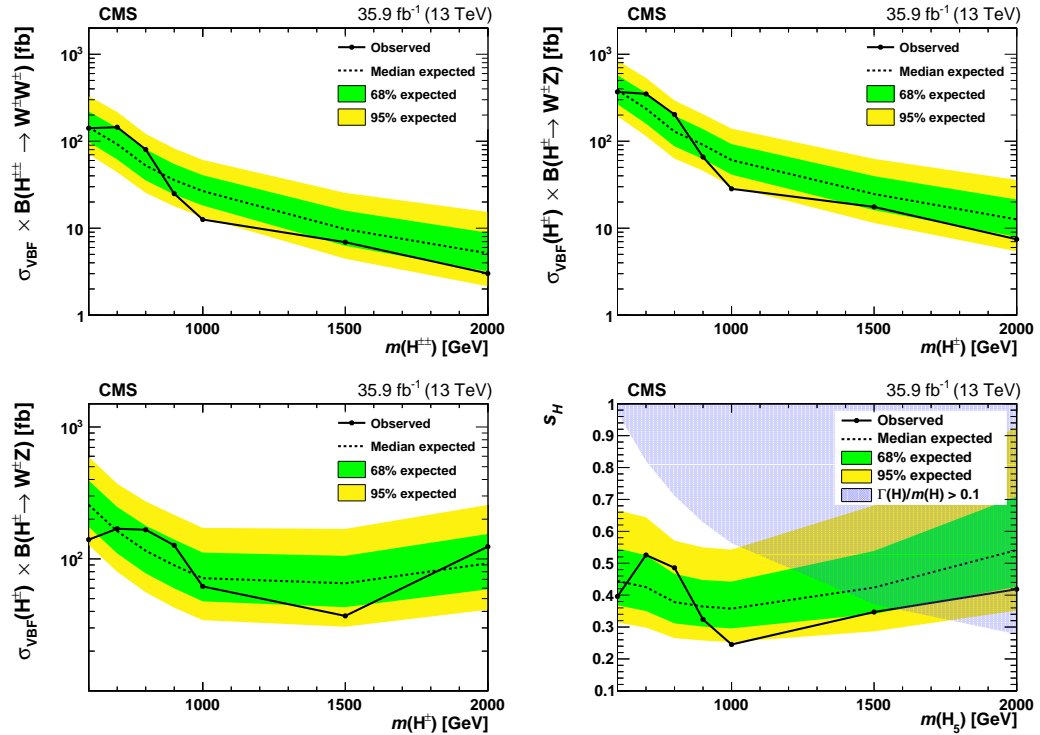


Figure 4.21: Expected and observed exclusion limits at 95% confidence level as functions of $m(H^{\pm\pm})$ and $m(H^\pm)$ for $\sigma_{\text{VBF}}(H^{\pm\pm}) \mathcal{B}(H^{\pm\pm} \rightarrow WW)$ (top left) and $\sigma_{\text{VBF}}(H^\pm) \mathcal{B}(H^\pm \rightarrow WZ)$ in the WV (top right) and ZV (bottom left) final states, and on the ratio of vacuum expectation values in the GM model (bottom right). The blue shaded area covers the theoretically not allowed parameter space [152].

5

Summary and Outlook

This thesis covers two broad topics, one based upon the hardware activities and another one based upon the physics analysis. On the hardware front, this thesis includes the studies carried out for the characterization of Gas Electron Multiplier (GEM) detectors for the CMS GE1/1 detector system upgrade, which is followed by the characterisation study of “*Indian origin*” GEM foils for the future CMS muon detector system upgrades foreseen during the period 2024-2026. The physics analysis described in this thesis is aimed to measure anomalous Quartic-Gauge Coupling (aQGC) phenomenon using the proton-proton collision data collected using the CMS detector at a center-of-mass energy of 13 TeV. A brief summary of both these topics task is given below.

For the CMS muon endcap detector system upgrade, triple-layer GEM detectors are proposed to be installed during the Long-Shutdown-2 (2019-2020) period because of their excellent performance capabilities even in the harsh radiation environment conditions at the LHC. This upgrade project is named as CMS GE1/1 upgrade, where the letter “G” stands for GEM, “E” stands for End-cap, the first “1” corresponds to the first muon station and the second “1” corresponds to the first ring of the station. To test the functionality of these GE1/1 detectors, multiple beam tests were carried out in the year 2014 to measure their properties and evaluate their performance in terms of spatial and timing resolution, cluster size and detection efficiency. Results from these beam test campaigns carried out at CERN are documented in this thesis. The detection efficiency of CMS GE1/1 prototype detector, completely instrumented with the proposed readout electronics, is measured using a scintillator and GEM detector based test set-up.

It is observed that the GE1/1 prototype detector has a detection efficiency greater than 98% and timing resolution is 5-7 ns.

Furthermore, the performance of GE1/1 detectors is scrutinized for two different gas mixtures viz. $Ar : CO_2$ (70:30) and $Ar : CO_2 : CF_4$ (40:15:45). It is found that one can operate GEM detectors without CF_4 , which is a non-eco friendly gas, without compromising the detection efficiency and timing resolution of the detector. To confirm the radiation hardness capabilities of GE1/1 detectors same set of tests were performed on GE1/1 detector, which has been irradiated with gamma rays for long durations. The obtained results were compatible with other GE1/1 detectors thus ensuring their performance in high background rate environments.

Along with the GE1/1 upgrade studies, the characterisation studies of the GEM foil indigenously developed in India were also performed in the Detector laboratory at the University of Delhi. An Indian company, Micropack Pvt. Ltd., developed the technology to develop GEM foils with the help of experts from CERN under the Transfer-of-Technology (TOT) agreement between CERN and India.

GEM foils with dimensions $10\text{ cm} \times 10\text{ cm}$ were successfully produced using the double mask technique. These GEM foils are then characterized using optical and electrical methods to check for any defects and abnormalities, which could affect the detector performance. Minimal defects were found in the GEM foils ($< 0.13\%$ of total GEM holes) and a very small value of leakage current ($< 10\text{ nA}$) was measured, which is well within the standards of CERN quality control criteria.

For the physics analysis, a search for anomalous ElectroWeak (EW) production of WW, WZ and ZZ boson pairs in association with two jets are reported using a model independent way. This is done by probing the vector boson scattering (VBS) process which could shed light on the non-Abelian gauge structure of the EW interactions of the Standard Model (SM) of particle physics. Several theoretical models beyond the SM predict enhancement in production cross-section for VBS processes through modifications of the Higgs boson couplings to gauge bosons. The VBS processes are produced via the EW interactions and are very sensitive to quartic gauge couplings. An observed excess in number of events with respect to the SM predictions could indicate the presence of anomalous Quartic Gauge Couplings (aQGC) or the existence of new resonances. With this motivation, a search for the presence of aQGC is carried out in events containing a hadronically decaying gauge boson (V), another gauge boson (W or Z) decaying leptonically either into electrons or muons, and two

Parameters	WWWW	WWZZ	ZZZZ	WWAZ	WWAA	ZZZA	ZZAA	ZAAA	AAAA
$f_{S,0}, f_{S,1}$	×	×	×						
$f_{M,0}, f_{M,1}, f_{M,6}, f_{M,7}$	×	×	×	×	×	×	×		
$f_{M,2}, f_{M,3}, f_{M,4}, f_{M,5}$		×	×	×	×	×	×		
$f_{T,0}, f_{T,1}, f_{T,2}$	×	×	×	×	×	×	×	×	×
$f_{T,5}, f_{T,6}, f_{T,7}$		×	×	×	×	×	×	×	×
$f_{T,8}, f_{T,9}$			×			×	×	×	×

Table 5.1: Quartic vertices modified by the different operators are marked with \times . In the first row W, Z and A refer to the W-boson, Z-boson and photon respectively. In the first column, the bold parameters are measured and the limits are reported.

jets present in high pseudo-rapidity regions of the CMS detector. The hadronically decaying gauge boson is highly boosted thus produces two jets which are merged into a single jet of larger radii (0.8). This final state benefits from the higher branching ratio of the V decay compared to previous searches carried out at the LHC for aQGC involving only leptonic decays of the vector bosons.

These studies are carried out based on the Effective Field Theory (EFT), by parametrizing the effects of higher energies on the energy scale available to us. The new effective Lagrangian based upon the EFT is given as:

$$\mathcal{L}_{eff} = \mathcal{L}_{SM} + \sum_{i=www,w,B,\phi W,\phi B} \frac{c_i}{\Lambda^2} \mathcal{O}_i + \sum_{j=0,1} \frac{f_{S,j}}{\Lambda^4} \mathcal{O}_{S,j} + \sum_{j=0,...,9} \frac{f_{T,j}}{\Lambda^4} \mathcal{O}_{T,j} + \sum_{j=0,...,7} \frac{f_{M,j}}{\Lambda^4} \mathcal{O}_{M,j} \quad (5.1)$$

where, Λ is the scale of new physics, the parameters c_i , $f_{S,j}$, $f_{T,j}$ and $f_{M,j}$ are the dimensionless coupling-strength coefficients typically of $\mathcal{O}(1)$. In the above equation, the dimension eight operators have only quartic couplings. There are a total of 18 independent parameters that are shown in Table 5.1. Out of them, we measure 9 parameters which are: $f_{S,0}$, $f_{S,1}$, $f_{M,0}$, $f_{M,1}$, $f_{M,6}$, $f_{M,7}$, $f_{T,0}$, $f_{T,1}$ and $f_{T,2}$.

The analysed data sample corresponds to an integrated luminosity of 35.9 fb^{-1} collected using the CMS detector in proton-proton collisions at a center-of-mass energy of 13 TeV. The EW signal processes with two final state quarks are simulated at leading-order with six EW and zero quantum chromodynamics (QCD) vertices. The QCD-initiated production of two gauge bosons with two final state quarks and at least one QCD vertex, which is referred to as diboson production, is considered as a background. First step towards the measurement involves the estimation of interference between the EW and QCD-initiated production of the signal process i.e. $pp \rightarrow VVjj$. This interference was found to be less than 1% and hence ignored the interference effect in the subsequent analysis steps. The major background contrib-

bution arise from the associated production of a W-boson and jets. A data-driven method was adopted to estimate the contribution from this background process.

Events are selected as per the VBS topology, i.e., by requiring two jets at large rapidity separation having large invariant mass of the di-jet system, one or two leptons (electrons or muons), a merged jet with large radii and large missing transverse momentum.

The statistical analysis is performed using the four-body invariant mass (i.e. mass of di-boson system) based on the frequentist approach in the asymptotic approximation.

Limits on the aforementioned dimension-eight operators are extracted at 95% Confidence-Level (CL). The limits for WV and ZV channels are summarized in Table-5.2 and Table-5.3. Also, the combined limits for the WV and ZV channels are shown in Table-5.4.

	Observed limits (TeV ⁻⁴)	Expected limits (TeV ⁻⁴)
f_{S0}/Λ^4	[−2.6, 2.7]	[−4.0, 4.0]
f_{S1}/Λ^4	[−3.2, 3.3]	[−4.9, 4.9]
f_{M0}/Λ^4	[−0.66, 0.66]	[−0.95, 0.95]
f_{M1}/Λ^4	[−1.9, 2.0]	[−2.8, 2.8]
f_{M6}/Λ^4	[−1.3, 1.3]	[−1.9, 1.9]
f_{M7}/Λ^4	[−3.3, 3.2]	[−4.8, 4.8]
f_{T0}/Λ^4	[−0.11, 0.10]	[−0.16, 0.15]
f_{T1}/Λ^4	[−0.11, 0.12]	[−0.17, 0.17]
f_{T2}/Λ^4	[−0.27, 0.27]	[−0.38, 0.38]

Table 5.2: Observed and expected 95% CL limits on the coefficients for higher-order (dimension-8) operators in the effective field theory Lagrangian in WV final state.

The WV and ZV (specially, the $W^\pm W^\pm$ and $W^\pm Z$) fusion channels are of special interest because they involves the production and decay of a heavy, singly or doubly charged Higgs boson. Thus these channels can also provide us the means to study the couplings of type $W^\pm ZH^\pm$ and $H^{\pm\pm}W^\pm W^\pm$ [18]. In this thesis the singly and doubly charged Higgs are considered in the framework of a specific model suggested by Georgi and Machacek [19]. This model predicts the existence of doubly and singly charged Higgs bosons using the Higgs triplets. The main feature of this model is that it preserves the custodial symmetry and provides neutrinos with a Majorana mass. In this model the strength of couplings of charged Higgs with the vector

	Observed limits (TeV ⁻⁴)	Expected limits (TeV ⁻⁴)
f_{S0}/Λ^4	[−37, 37]	[−29, 29]
f_{S1}/Λ^4	[−30, 30]	[−23, 23]
f_{M0}/Λ^4	[−6.9, 6.9]	[−5.1, 5.1]
f_{M1}/Λ^4	[−21, 21]	[−15, 15]
f_{M6}/Λ^4	[−14, 14]	[−10, 10]
f_{M7}/Λ^4	[−33, 33]	[−24, 24]
f_{T0}/Λ^4	[−1.3, 1.3]	[−0.95, 0.95]
f_{T1}/Λ^4	[−1.4, 1.4]	[−0.98, 0.99]
f_{T2}/Λ^4	[−3.1, 3.2]	[−2.3, 2.3]

Table 5.3: Observed and expected 95% CL limits on the coefficients for higher-order (dimension-8) operators in the effective field theory Lagrangian in ZV final state.

	Observed limits (TeV ⁻⁴)	Expected limits (TeV ⁻⁴)
f_{S0}/Λ^4	[−2.6, 2.7]	[−4.0, 4.0]
f_{S1}/Λ^4	[−3.2, 3.3]	[−4.9, 4.9]
f_{M0}/Λ^4	[−0.66, 0.66]	[−0.95, 0.95]
f_{M1}/Λ^4	[−1.9, 2.0]	[−2.8, 2.8]
f_{M6}/Λ^4	[−1.3, 1.3]	[−1.9, 1.9]
f_{M7}/Λ^4	[−3.3, 3.2]	[−4.8, 4.8]
f_{T0}/Λ^4	[−0.11, 0.10]	[−0.16, 0.15]
f_{T1}/Λ^4	[−0.11, 0.12]	[−0.17, 0.17]
f_{T2}/Λ^4	[−0.27, 0.27]	[−0.38, 0.38]

Table 5.4: Observed and expected 95% CL combined limits on the coefficients for higher-order (dimension-8) operators in the effective field theory Lagrangian in WV and ZV final states.

bosons are parametrized using $\sin(\theta_H)$ (s_H), where $s_H = 0$ will correspond to the SM scenario. The measurement of s_H will reflect the extent to which triplet scalar representation participates in the EWSB. The exclusion limits on the charged Higgs bosons $\sigma_{\text{VBF}}(H^{\pm\pm}) \mathcal{B}(H^{\pm\pm} \rightarrow WW)$ and $\sigma_{\text{VBF}}(H^\pm) \mathcal{B}(H^\pm \rightarrow WZ)$ at 95% confidence level as functions of $m(H^\pm)$ and $m(H^{\pm\pm})$, respectively, for the WV final state are shown in Fig. 5.1 (top left and right). The exclusion limit on the charged Higgs $\sigma_{\text{VBF}}(H^\pm) \mathcal{B}(H^\pm \rightarrow WZ)$ at 95% confidence level as a function of $m(H^\pm)$ for the ZV final state is shown in bottom left panel in Fig. 5.1. The coupling depends on $m(5)$ and the parameter s_H , where s_H^2 denotes the fraction of the W boson mass square generated by the vacuum expectation value of the triplets. The combination of the model-independent exclusion limits can be used to constrain the s_H - $m(5)$ plane by using the predicted cross sections at NNLO accuracy in the GM model. The excluded s_H values as a function of $m(5)$ are shown in Fig. 5.1 (bottom right).

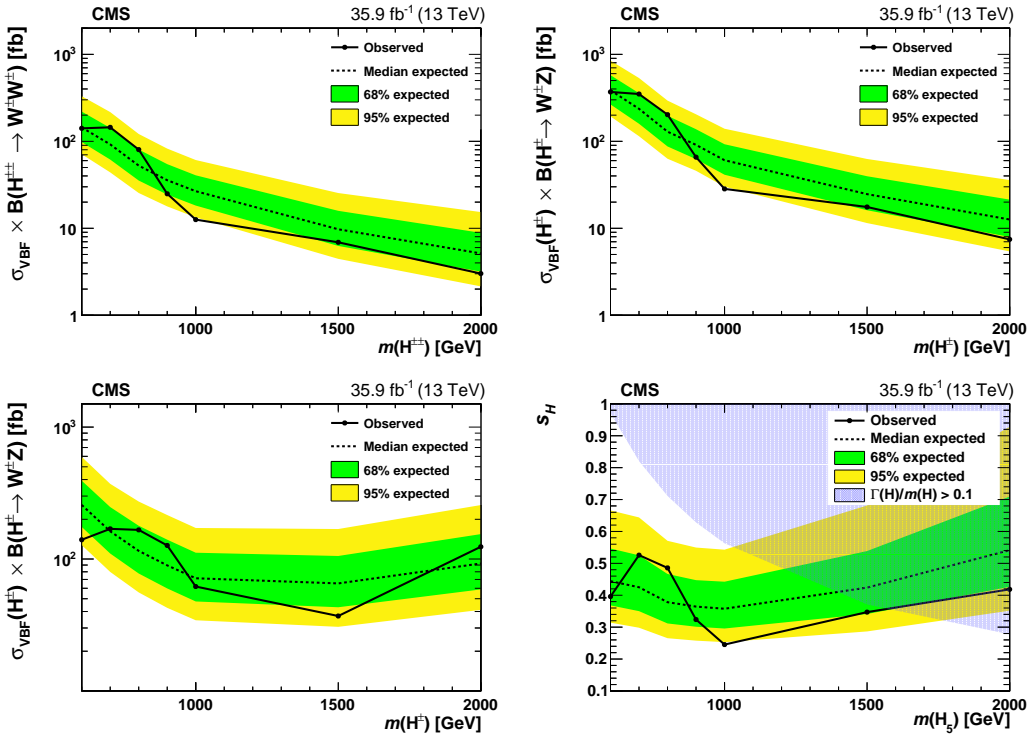


Figure 5.1: Expected and observed exclusion limits at 95% confidence level as functions of $m(H^{\pm\pm})$ and $m(H^\pm)$ for $\sigma_{\text{VBF}}(H^{\pm\pm}) \mathcal{B}(H^{\pm\pm} \rightarrow WW)$ (top left) and $\sigma_{\text{VBF}}(H^\pm) \mathcal{B}(H^\pm \rightarrow WZ)$ in the WV (top right) and ZV (bottom left) final states, and on the ratio of vacuum expectation values in the GM model (bottom right). The blue shaded area covers the theoretically not allowed parameter space [152].

5.1 Future Outlook

For future upgrades of the CMS detector to cope-up with the high luminosity runs of the LHC includes the upgrade of muon system. The CMS GEM community started R&D of the GEM detectors for the CMS phase-II upgrade which includes a second GEM detector station (GE2/1) in the muon endcaps. This CMS GE2/1 upgrade will result in increased average number of muon hits registered in the muon detectors in the forward regions. The forwards regions of the CMS detector experience high particle rates and a low magnetic bending power and the addition of GEM detectors in these regions will, thus, improve the forward tracking. The CMS GEM collaboration is also working on the proposal for a MEO muon detector station for pseudo-rapidity regions lying between 2.2 to 2.8, for which the R&D is also going on. The GEM foils produced in India, after passing the standard quality control criteria, will be used for these upgrades. The beam test studies performed during the course of this PhD thesis will be helpful to finalize the detector designs for these upgrades. The analysis framework developed could be employed during the data analysis of future beam test campaigns. Besides, the GEM detectors could also be used for the detection of ultra-violet and visible photons and studies are ongoing for their use in the medical industry [153, 154, 155] and for tomographic reconstruction [156].

The physics analysis presented in this thesis marks the starting phase of quartic-gauge coupling studies and the VBS at the LHC. Due to low values of production cross-section for the VBS processes, it has yet not been observed. In future, with refined analysis techniques and larger amount of data, it could be possible to improve the aQGC limits by several factors. The first step towards this goal would be to analyze complete LHC Run-II (2016-2018) data which correspond to an integrated luminosity of $\sim 150 \text{ fb}^{-1}$. With this one might also be able to investigate the SM production of the electroweak process W^+W^-jj , which could be observed at least significance of 2σ . The Run-3 (2021-2023) of the LHC will be much more exciting for these kind of studies and should definitely provide yet more exciting information about the EWSB mechanism.

Bibliography

- [1] Sheldon L. Glashow. “Partial-symmetries of weak interactions”. In: *Nucl. Phys.* 22.4 (1961), pp. 579–588. DOI: [10.1016/0029-5582\(61\)90469-2](https://doi.org/10.1016/0029-5582(61)90469-2).
- [2] Steven Weinberg. “A Model of Leptons”. In: *Phys. Rev. Lett.* 19 (1967), p. 1264. DOI: [10.1103/PhysRevLett.19.1264](https://doi.org/10.1103/PhysRevLett.19.1264).
- [3] Abdus Salam. “Weak and electromagnetic interactions”. In: *Elementary particle physics: relativistic groups and analyticity*. Ed. by Nils Svartholm. Proceedings of the eighth Nobel symposium. Almqvist & Wiksell, 1968, p. 367.
- [4] F. Englert and R. Brout. “Broken Symmetry and the Mass of Gauge Vector Mesons”. In: *Physical Review Letters* 13.9 (1964), pp. 321–323. DOI: [10.1103/physrevlett.13.321](https://doi.org/10.1103/physrevlett.13.321).
- [5] P.W. Higgs. “Broken symmetries, massless particles and gauge fields”. In: *Physics Letters* 12.2 (1964), pp. 132–133. DOI: [10.1016/0031-9163\(64\)91136-9](https://doi.org/10.1016/0031-9163(64)91136-9).
- [6] Peter W. Higgs. “Broken Symmetries and the Masses of Gauge Bosons”. In: *Physical Review Letters* 13.16 (1964), pp. 508–509. DOI: [10.1103/physrevlett.13.508](https://doi.org/10.1103/physrevlett.13.508).
- [7] G. S. Guralnik, C. R. Hagen, and T. W. B. Kibble. “Global Conservation Laws and Massless Particles”. In: *Physical Review Letters* 13.20 (1964), pp. 585–587. DOI: [10.1103/physrevlett.13.585](https://doi.org/10.1103/physrevlett.13.585).
- [8] Peter W. Higgs. “Spontaneous Symmetry Breakdown without Massless Bosons”. In: *Physical Review* 145.4 (1966), pp. 1156–1163. DOI: [10.1103/physrev.145.1156](https://doi.org/10.1103/physrev.145.1156).

- [9] T. W. B. Kibble. “Symmetry Breaking in Non-Abelian Gauge Theories”. In: *Physical Review* 155.5 (1967), pp. 1554–1561. DOI: 10.1103/physrev.155.1554.
- [10] S. Chatrchyan et al. “Observation of a new boson at a mass of 125 GeV with the CMS experiment at the LHC”. In: *Physics Letters B* 716.1 (2012), pp. 30–61. DOI: 10.1016/j.physletb.2012.08.021.
- [11] Georges Aad et al. “Observation of a new particle in the search for the Standard Model Higgs boson with the ATLAS detector at the LHC”. In: *Phys. Lett. B* 716 (2012), p. 1. DOI: 10.1016/j.physletb.2012.08.020. arXiv: 1207.7214 [hep-ex].
- [12] M. Baak et al. “Study of Electroweak Interactions at the Energy Frontier”. In: (Oct. 24, 2013). arXiv: <http://arxiv.org/abs/1310.6708v1> [hep-ph].
- [13] *The Standard Model and beyond*. URL: <https://uslhc.web.cern.ch/physics/standard-model-and-beyond>.
- [14] M. Tanabashi et al. “Review of Particle Physics”. In: *Physical Review D* 98.3 (Aug. 2018). DOI: 10.1103/physrevd.98.030001. URL: <http://pdg.lbl.gov>.
- [15] Guy D Coughlan, James Edmund Dodd, and Ben M Gripaios. *The Ideas of Particle Physics : an Introduction for Scientists*. Cambridge: Cambridge university press, 2006.
- [16] J Ellis. *Higgs Physics*. eng. 2015. DOI: 10.5170/cern-2015-004.117.
- [17] Céline Degrande et al. “Effective field theory: A modern approach to anomalous couplings”. In: *Annals of Physics* 335 (2013), pp. 21–32. DOI: 10.1016/j.aop.2013.04.016.
- [18] Roberto Vega. “Vector Boson Scattering at Future Colliders”. In: *Higgs Particle(s)*. Springer US, 1990, pp. 359–367. DOI: 10.1007/978-1-4757-0908-7_18.
- [19] Howard Georgi and Marie Machacek. “Doubly charged Higgs bosons”. In: *Nucl. Phys. B* 262 (1985), p. 463. DOI: 10.1016/0550-3213(85)90325-6.
- [20] Ranko Ostojic et al. *LHC Design Report Vol.2: The LHC Infrastructure and General Services*. eng. Cern document server. 2004. DOI: 10.5170/cern-2004-003-v-2. URL: <http://cds.cern.ch/record/815187>.

- [21] Karlheinz Schindl et al. *LHC Design Report Vol.3: The LHC Injector Chain*. eng. 2004. DOI: 10.5170/cern-2004-003-v-3. URL: <http://cds.cern.ch/record/823808>.
- [22] Oliver S. Bruning et al. *LHC Design Report Vol.1: The LHC Main Ring*. Tech. rep. CERN-2004-003-V1, CERN-2004-003, CERN-2004-003-V-1. CERN, 2004. URL: <https://cds.cern.ch/record/782076>.
- [23] The CMS Collaboration et al. “The CMS experiment at the CERN LHC”. In: *Journal of Instrumentation* 3.08 (Aug. 2008), S08004–S08004. DOI: 10.1088/1748-0221/3/08/s08004.
- [24] CMS collaboration. *CMS Luminosity - Public results*. CMS. URL: <https://twiki.cern.ch/twiki/bin/view/CMSPublic/LumiPublicResults>.
- [25] B Muratori and Werner Herr. *Concept of luminosity*. eng. 2006. DOI: 10.5170/cern-2006-002.361. URL: <https://cds.cern.ch/record/941318/?ln=en>.
- [26] A Colaleo et al. *CMS Technical Design Report for the Muon Endcap GEM Upgrade*. Tech. rep. CERN-LHCC-2015-012. CMS-TDR-013. June 2015. URL: <https://cds.cern.ch/record/2021453>.
- [27] Rui DE OLIVEIRA and Serge DUARTE PINTO. “A METHOD OF MANUFACTURING A GAS ELECTRON MULTIPLIER”. English. Pat. WO/2009/127220. Oct. 2009. URL: <https://patentscope.wipo.int/search/en/detail.jsf?docId=W02009127220&recNum=&maxRec=1000&office=&prevFilter=&sortOption=&queryString=&tab=PCTBiblio>.
- [28] John Hauptman. *Particle Physics Experiments at High Energy Colliders*. Wiley VCH Verlag GmbH, 2010. ISBN: 3527408258. URL: https://www.ebook.de/de/product/11435469/john_hauptman_particle_physics_experiments_at_high_energy_colliders.html.
- [29] M. Demarteau et al. “Particle and nuclear physics instrumentation and its broad connections”. In: *Reviews of Modern Physics* 88.4 (2016). DOI: 10.1103/revmodphys.88.045007.
- [30] Corinne Pralavorio. *Accelerating particles - but not just for the LHC*. July 2017. URL: <https://home.cern/about/updates/2017/07/accelerating-particles-not-just-lhc>.

- [31] Esma Anais Mobs. *The CERN accelerator complex*. Oct. 2016. URL: <https://cds.cern.ch/record/2225847>.
- [32] Xabier Cid Vidal and Ramon Cid Manzano. *Taking a closer look at LHC: Magnetic multipoles*. URL: http://www.lhc-closer.es/taking_a_closer_look_at_lhc/0.magnetic_multipoles.
- [33] *LHC magnet types*. CERN. URL: http://lhc-machine-outreach.web.cern.ch/lhc-machine-outreach/components/magnets/types_of_magnets.htm.
- [34] Roderik Bruce et al. “LHC Run 2: Results and Challenges”. en-us. In: *Proceedings of the 57th ICFA Advanced Beam Dynamics Workshop on High-Intensity and High-Brightness Hadron Beams, HB2016, Malmö, Sweden* (2016). DOI: 10.18429/jacow-hb2016-moam5p50.
- [35] Thomas Schörner-Sadenius, ed. *The Large Hadron Collider*. Springer International Publishing, 2015. DOI: 10.1007/978-3-319-15001-7.
- [36] Mike Lamont. *LHC Performance 2016*. CERN. July 2016. URL: <https://lhc-commissioning.web.cern.ch/lhc-commissioning/performance/2016-performance.htm>.
- [37] W Herr and T Pieloni. *Beam-Beam Effects*. eng. 2014. DOI: 10.5170/cern-2014-009.431. URL: <https://cds.cern.ch/record/1982430>.
- [38] G. Papotti et al. “Observations of beam-beam effects at the LHC”. In: *CERN-2014-004* (Sept. 18, 2014), pp. 1–5. arXiv: <http://arxiv.org/abs/1409.5208v1> [physics.acc-ph]. URL: <https://arxiv.org/abs/1409.5208>.
- [39] Frédéric Dubouchet. “Betatron tune measurement with the LHC damper using a GPU”. CERN-THESIS-2013-035. MA thesis. 2013. URL: <https://cds.cern.ch/record/1545785?ln=en>.
- [40] Adrian Oeftiger. “Space Charge Effects and Advanced Modelling for CERN Low Energy Machines”. CERN-THESIS-2016-170. PhD thesis. 2016. URL: <https://cds.cern.ch/record/2233212?ln=en>.
- [41] Corinne Pralavorio and Corinne Pralavorio. “2016: an exceptional year for the LHC”. In: (Dec. 2016). URL: <https://cds.cern.ch/record/2240055>.
- [42] CERN. *LHC Images*. URL: https://lhc-machine-outreach.web.cern.ch/lhc-machine-outreach/lhc_in_pictures.htm.

- [43] Aram Apyan and Markus Klute. “Electroweak physics and evidence for a Higgs boson decaying to a pair of tau leptons with the CMS detector”. Presented 15 Nov 2016. PhD thesis. MIT, Cambridge, Dept. Phys., Nov. 2017. URL: <https://cds.cern.ch/record/2290872?ln=en>.
- [44] Lucas Taylor. “CMS detector design”. In: (Nov. 2011). URL: <http://cms.web.cern.ch/news/cms-detector-design>.
- [45] Maximilien Brice and Claudia Marcelloni. *The central part of CMS is lowered. Descente dans la caverne de la partie centrale du détecteur de particules CMS (Compact Muon Solenoid)*. CERN-EX-0702022. Feb. 2007. URL: <https://cds.cern.ch/record/1020311>.
- [46] CMS Collaboration. *The CMS muon project: Technical Design Report*. Technical Design Report CMS. Geneva: CERN, 1997. URL: <https://cds.cern.ch/record/343814>.
- [47] Jeremie Alexandre Merlin, Jean-Marie Brom, and Archana Sharma. “Study of long-term sustained operation of gaseous detectors for the high rate environment in CMS”. Presented 25 Apr 2016. PhD thesis. Apr. 2016. URL: <https://cds.cern.ch/record/2155685>.
- [48] private communication W.J. Stirling. *Standard Model cross sections as a function of collider energy (2012 version)*. 2012. URL: <http://www.hep.ph.ic.ac.uk/~wstirlin/plots/plots.html>.
- [49] A. D. Martin et al. “Parton distributions for the LHC”. In: *The European Physical Journal C* 63.2 (2009), pp. 189–285. DOI: [10.1140/epjc/s10052-009-1072-5](https://doi.org/10.1140/epjc/s10052-009-1072-5).
- [50] ZEUS Collaboration. “The ZEUS detector: Status report 1993”. en. In: *597 pp. (1993)*. (1993). DOI: [10.3204/pubdb-2017-12635](https://doi.org/10.3204/pubdb-2017-12635).
- [51] Sergio Cittolin, Attila Rácz, and Paris Sphicas. *CMS The TriDAS Project: Technical Design Report, Volume 2: Data Acquisition and High-Level Trigger. CMS trigger and data-acquisition project*. Technical Design Report CMS. Geneva: CERN, 2002. URL: <https://cds.cern.ch/record/578006>.
- [52] V. Khachatryan et al. “The CMS trigger system”. In: *Journal of Instrumentation* 12.01 (Jan. 2017), P01020–P01020. DOI: [10.1088/1748-0221/12/01/p01020](https://doi.org/10.1088/1748-0221/12/01/p01020). URL: <https://cds.cern.ch/record/2212926?ln=en>.

- [53] CMS Collaboration. *CMS Technical Design Report for the Level-1 Trigger Upgrade*. Tech. rep. CERN-LHCC-2013-011. CMS-TDR-12. Additional contacts: Jeffrey Spalding, Fermilab, Jeffrey.Spalding@cern.ch Didier Contardo, Universite Claude Bernard-Lyon I, didier.claude.contardo@cern.ch. June 2013. URL: <http://cds.cern.ch/record/1556311>.
- [54] J Erö et al. “The CMS Drift Tube Trigger Track Finder”. In: *Journal of Instrumentation* 3.08 (Aug. 2008), P08006–P08006. DOI: 10.1088/1748-0221/3/08/p08006.
- [55] Andrea Perrotta. “Performance of the CMS High Level Trigger”. In: *Journal of Physics: Conference Series* 664.8 (Dec. 2015), p. 082044. DOI: 10.1088/1742-6596/664/8/082044.
- [56] R. E. Kalman. “A New Approach to Linear Filtering and Prediction Problems”. In: *Journal of Basic Engineering* 82.1 (1960), p. 35. DOI: 10.1115/1.3662552. URL: <http://www.cs.unc.edu/~welch/media/pdf/Kalman1960.pdf>.
- [57] R. Frühwirth and S. Frühwirth-Schnatter. “On the treatment of energy loss in track fitting”. In: *Computer Physics Communications* 110.1-3 (1998), pp. 80–86. DOI: 10.1016/s0010-4655(97)00157-4.
- [58] R Frühwirth. “Track fitting with non-Gaussian noise”. In: *Computer Physics Communications* 100.1-2 (Feb. 1997), pp. 1–16. DOI: 10.1016/s0010-4655(96)00155-5.
- [59] W Adam et al. “Reconstruction of electrons with the Gaussian-sum filter in the CMS tracker at the LHC”. In: *Journal of Physics G: Nuclear and Particle Physics* 31.9 (July 2005), N9–N20. DOI: 10.1088/0954-3899/31/9/n01. URL: <https://cds.cern.ch/record/815410?ln=en>.
- [60] Rene Brun and Fons Rademakers. “ROOT - An Object Oriented Data Analysis Framework”. In: *Nucl. Inst. & Meth. in Phys. Res. A* 389 (Sept. 1996). See also <http://root.cern.ch/>, pp. 81–86. URL: <https://root.cern.ch/publications>.
- [61] G L Bayatyan, Michel Della Negra, and Achille Petrilli. “CMS: The computing project. Technical design report”. In: *Geneva : CERN* CERN-LHCC-2005-023 (2005). URL: <http://cds.cern.ch/record/838359>.

- [62] S. Agostinelli et al. “Geant4—a simulation toolkit”. In: *Nuclear Instruments and Methods in Physics Research Section A: Accelerators, Spectrometers, Detectors and Associated Equipment* 506.3 (July 2003), pp. 250–303. DOI: 10.1016/s0168-9002(03)01368-8.
- [63] G. Charpak et al. “The use of multiwire proportional counters to select and localize charged particles”. In: *Nuclear Instruments and Methods* 62.3 (1968), pp. 262–268. DOI: 10.1016/0029-554x(68)90371-6.
- [64] F. Sauli. “GEM: A new concept for electron amplification in gas detectors”. In: *Nuclear Instruments and Methods in Physics Research Section A: Accelerators, Spectrometers, Detectors and Associated Equipment* 386.2-3 (Feb. 1997), pp. 531–534. DOI: 10.1016/s0168-9002(96)01172-2.
- [65] Fabio Sauli and Archana Sharma. “Micropattern Gaseous Detectors”. In: *Annual Review of Nuclear and Particle Science* 49.1 (1999), pp. 341–388. DOI: 10.1146/annurev.nucl.49.1.341.
- [66] “A GEM of a detector”. In: *CERN Courier* 38.9 (Dec. 1998), pp. 19–20. URL: <https://cds.cern.ch/record/1732870>.
- [67] Maxim Titov. “Radiation damage and long-term ageing in gas detectors”. In: *Innovative Detectors for Supercolliders*. WORLD SCIENTIFIC, 2004. DOI: 10.1142/9789812702951_0014.
- [68] M. Titov et al. “Summary and outlook of the international workshop on aging phenomena in gaseous detectors (DESY, Hamburg, October 2001)”. In: *IEEE Transactions on Nuclear Science* 49.4 (2002), pp. 1609–1621. DOI: 10.1109/tns.2002.801666.
- [69] P. Abbon et al. “The COMPASS experiment at CERN”. In: *Nuclear Instruments and Methods in Physics Research Section A: Accelerators, Spectrometers, Detectors and Associated Equipment* 577.3 (2007), pp. 455–518. DOI: 10.1016/j.nima.2007.03.026.
- [70] V Berardi et al. *TOTEM: Technical Design Report*. Tech. rep. CERN-LHCC-2004-002 ; TOTEM-TDR-001. 2004. URL: <http://cds.cern.ch/record/704349>.

- [71] The LHCb Collaboration et al. “The LHCb Detector at the LHC”. In: *Journal of Instrumentation* 3.08 (2008), S08005–S08005. DOI: 10.1088/1748-0221/3/08/s08005.
- [72] *Kapton Sheet (Tradename of Du Pont Co., Wilmington, DE, USA)*. URL: <http://www.dupont.com/products-and-services/membranes-films/polyimide-films/brands/kapton-polyimide-film.html>.
- [73] J. Benlloch et al. “Development of the gas electron multiplier (GEM)”. In: *IEEE Transactions on Nuclear Science* 45.3 (1998), pp. 234–243. DOI: 10.1109/23.682386.
- [74] S. Bachmann et al. “Discharge studies and prevention in the gas electron multiplier (GEM)”. In: *Nuclear Instruments and Methods in Physics Research Section A: Accelerators, Spectrometers, Detectors and Associated Equipment* 479.2-3 (2002), pp. 294–308. DOI: 10.1016/s0168-9002(01)00931-7.
- [75] D. Abbaneo et al. “GEM based detector for future upgrade of the CMS forward muon system”. In: *Nuclear Instruments and Methods in Physics Research Section A: Accelerators, Spectrometers, Detectors and Associated Equipment* 718 (2013), pp. 383–386. DOI: 10.1016/j.nima.2012.10.058.
- [76] D. Abbaneo et al. “Characterization of GEM detectors for application in the CMS muon detection system”. In: *IEEE Nuclear Science Symposium & Medical Imaging Conference*. IEEE, 2010. DOI: 10.1109/nssmic.2010.5874006.
- [77] D. Abbaneo et al. “Test beam results of the GE1/1 prototype for a future upgrade of the CMS high- η muon system”. In: *2011 IEEE Nuclear Science Symposium Conference Record*. IEEE, 2011. DOI: 10.1109/nssmic.2011.6154688.
- [78] D. Abbaneo et al. “Beam test results for new full-scale GEM prototypes for a future upgrade of the CMS high- η Muon System”. In: *2012 IEEE Nuclear Science Symposium and Medical Imaging Conference Record (NSS/MIC)*. IEEE, Oct. 2012. DOI: 10.1109/nssmic.2012.6551293.
- [79] D. Abbaneo et al. “The status of the GEM project for CMS high- η muon system”. In: *Nuclear Instruments and Methods in Physics Research Section A: Accelerators, Spectrometers, Detectors and Associated Equipment* 732 (2013), pp. 203–207. DOI: 10.1016/j.nima.2013.08.015.

- [80] Jeremie Alexandre Merlin. “Study of long-term operation of triple-GEM detectors for the high rate environment in CMS”. In: CMS-CR-2013-279. Oct. 2013. URL: <https://cds.cern.ch/record/1621595>.
- [81] P Aspell et al. *VFAT2: A front-end system on chip providing fast trigger information, digitized data storage and formatting for the charge sensitive readout of multi-channel silicon and gas particle detectors.* eng. 2007. DOI: 10.5170/cern-2007-007.292.
- [82] F. Licciulli et al. “Calibration, bias and monitoring system for the VFAT3 ASIC of the CMS GEM detector”. In: *2017 7th IEEE International Workshop on Advances in Sensors and Interfaces (IWASI)*. IEEE, 2017. DOI: 10.1109/iwasi.2017.7974222.
- [83] Roberto Cecchi and Maria Grazia Bagliesi. “The Turbo Board and Software”. Siena University. May 2011. URL: <https://indico.cern.ch/event/136793/contributions/1360602/attachments/112026/159286/TURBO-PaulMeeting.pdf>.
- [84] P. Aspell et al. “The VFAT production test platform for the TOTEM experiment”. In: *Electronics for particle physics. Proceedings, Topical Workshop, TWEPP-08, Naxos, Greece, 15-19 September 2008*. 2008, pp. 544–548. URL: <http://doc.cern.ch/yellowrep/2008/2008-008/p544.pdf>.
- [85] TOTEM group. *TurboSoftware*. GitHub. Updated by Ram Krishna Sharma for CMS GEM test beam. URL: <https://github.com/ram1123/TurboSoftware>.
- [86] *KANOMAX dust particle counter Model 3887*. URL: https://www.kanomax-usa.com/wp-content/uploads/2015/10/3887_manual.pdf.
- [87] S. Bachmann et al. “Charge amplification and transfer processes in the gas electron multiplier”. In: *Nuclear Instruments and Methods in Physics Research Section A: Accelerators, Spectrometers, Detectors and Associated Equipment* 438.2-3 (1999), pp. 376–408. DOI: 10.1016/s0168-9002(99)00820-7.
- [88] M. Posik and B. Surrow. “Optical and electrical performance of commercially manufactured large GEM foils”. In: *Nuclear Instruments and Methods in Physics Research Section A: Accelerators, Spectrometers, Detectors and Associated Equipment* 802 (2015), pp. 10–15. DOI: 10.1016/j.nima.2015.08.048.

- [89] Ulrich Becker, Brian Tamm, and Scott Hertel. “Test and evaluation of new GEMs with an automatic scanner”. In: *Nuclear Instruments and Methods in Physics Research Section A: Accelerators, Spectrometers, Detectors and Associated Equipment* 556.2 (2006), pp. 527–534. DOI: 10.1016/j.nima.2005.11.056.
- [90] D. Abbaneo et al. “Quality control and beam test of GEM detectors for future upgrades of the CMS muon high rate region at the LHC”. In: *Journal of Instrumentation* 10.03 (2015), pp. C03039–C03039. DOI: 10.1088/1748-0221/10/03/c03039.
- [91] *MIT Megger 420*. URL: <https://www.instrumart.com/products/35023/megger-mit420-insulation-tester>.
- [92] *Keithley 6517B picoammeter*. URL: <https://www.tek.com/keithley-low-level-sensitive-and-specialty-instruments/keithley-high-resistance-low-current-electrom>.
- [93] O. J. P. Éboli, M. C. Gonzalez-Garcia, and J. K. Mizukoshi. “ $pp \rightarrow jj e^\pm \mu^\pm \nu\nu$ and $jj e^\mp \mu^\pm \nu\nu$ at $\mathcal{O}(\alpha_{em}^6)$ and $\mathcal{O}(\alpha_{em}^4 \alpha_s^2)$ for the study of the quartic electroweak gauge boson vertex at CERN LHC”. In: *Phys. Rev. D* 74 (2006), p. 073005. DOI: 10.1103/PhysRevD.74.073005. arXiv: hep-ph/0606118 [hep-ph].
- [94] Albert M Sirunyan et al. “Observation of electroweak production of same-sign W boson pairs in the two jet and two same-sign lepton final state in proton-proton collisions at $\sqrt{s} = 13$ TeV”. In: *Phys. Rev. Lett.* 120.8 (2018), p. 081801. DOI: 10.1103/PhysRevLett.120.081801. arXiv: 1709.05822 [hep-ex].
- [95] Georges Aad et al. “Evidence for Electroweak Production of $W^\pm W^\pm jj$ in pp Collisions at $\sqrt{s} = 8$ TeV with the ATLAS Detector”. In: *Phys. Rev. Lett.* 113 (2014), p. 141803. DOI: 10.1103/PhysRevLett.113.141803. arXiv: 1405.6241 [hep-ex].
- [96] Vardan Khachatryan et al. “Study of Vector Boson Scattering and Search for New Physics in Events with Two Same-Sign Leptons and Two Jets”. In: *Phys. Rev. Lett.* 114 (2015), p. 051801. DOI: 10.1103/PhysRevLett.114.051801. arXiv: 1410.6315 [hep-ex].

- [97] Morad Aaboud et al. “Measurement of $W^\pm W^\pm$ vector-boson scattering and limits on anomalous quartic gauge couplings with the ATLAS detector”. In: *Phys. Rev.* D96.1 (2017), p. 012007. DOI: 10.1103/PhysRevD.96.012007. arXiv: 1611.02428 [hep-ex].
- [98] Georges Aad et al. “Measurements of $W^\pm Z$ production cross sections in pp collisions at $\sqrt{s} = 8\text{TeV}$ with the ATLAS detector and limits on anomalous gauge boson self-couplings”. In: *Phys. Rev. D* 93 (2016), p. 092004. DOI: 10.1103/PhysRevD.93.092004. arXiv: 1603.02151 [hep-ex].
- [99] Albert M Sirunyan et al. “Measurement of vector boson scattering and constraints on anomalous quartic couplings from events with four leptons and two jets in proton–proton collisions at $\sqrt{s} = 13\text{ TeV}$ ”. In: *Phys. Lett.* B774 (2017), pp. 682–705. DOI: 10.1016/j.physletb.2017.10.020. arXiv: 1708.02812 [hep-ex].
- [100] Vardan Khachatryan et al. “Evidence for exclusive $\gamma\gamma \rightarrow W^+W^-$ production and constraints on anomalous quartic gauge couplings in pp collisions at $\sqrt{s} = 7$ and 8TeV ”. In: *JHEP* 08 (2016), p. 119. DOI: 10.1007/JHEP08(2016)119. arXiv: 1604.04464 [hep-ex].
- [101] Vardan Khachatryan et al. “Measurement of the cross section for electroweak production of $Z\gamma$ in association with two jets and constraints on anomalous quartic gauge couplings in proton–proton collisions at $\sqrt{s} = 8\text{TeV}$ ”. In: *Phys. Lett. B* 770 (2017), p. 380. DOI: 10.1016/j.physletb.2017.04.071. arXiv: 1702.03025 [hep-ex].
- [102] Vardan Khachatryan et al. “Measurement of electroweak-induced production of $W\gamma$ with two jets in pp collisions at $\sqrt{s} = 8\text{TeV}$ and constraints on anomalous quartic gauge couplings”. In: *JHEP* 06 (2017), p. 106. DOI: 10.1007/JHEP06(2017)106. arXiv: 1612.09256 [hep-ex].
- [103] Morad Aaboud et al. “Studies of $Z\gamma$ production in association with a high-mass dijet system in pp collisions at $\sqrt{s} = 8\text{ TeV}$ with the ATLAS detector”. In: *JHEP* 07 (2017), p. 107. DOI: 10.1007/JHEP07(2017)107. arXiv: 1705.01966 [hep-ex].

- [104] M. Aaboud et al. “Search for anomalous electroweak production of WW/WZ in association with a high-mass dijet system in pp collisions at s=8 TeV with the ATLAS detector”. In: *Physical Review D* 95.3 (2017). DOI: 10.1103/physrevd.95.032001.
- [105] Christoph Englert, Emanuele Re, and Michael Spannowsky. “Pinning down Higgs triplets at the LHC”. In: *Phys. Rev. D* 88 (2013), p. 035024. DOI: 10.1103/PhysRevD.88.035024. arXiv: 1306.6228 [hep-ph].
- [106] Albert M Sirunyan et al. “Search for Charged Higgs Bosons Produced via Vector Boson Fusion and Decaying into a Pair of W and Z Bosons Using pp Collisions at $\sqrt{s} = 13$ TeV”. In: *Phys. Rev. Lett.* 119.14 (2017), p. 141802. DOI: 10.1103/PhysRevLett.119.141802. arXiv: 1705.02942 [hep-ex].
- [107] G. Aad et al. “Search for a Charged Higgs Boson Produced in the Vector-Boson Fusion Mode with Decay $H^\pm \rightarrow W^\pm Z$ using pp Collisions at $\sqrt{s} = 8$ TeV with the ATLAS Experiment”. In: *Phys. Rev. Lett.* 114 (2015), p. 231801. DOI: 10.1103/PhysRevLett.114.231801. arXiv: 1503.04233.
- [108] S. Chatrchyan et al. “The CMS experiment at the CERN LHC”. In: *JINST* 3 (2008), S08004. DOI: 10.1088/1748-0221/3/08/S08004.
- [109] S. Agostinelli et al. “GEANT4—a simulation toolkit”. In: *Nucl. Instrum. Meth. A* 506 (2003), p. 250. DOI: 10.1016/S0168-9002(03)01368-8.
- [110] J. Alwall et al. “The automated computation of tree-level and next-to-leading order differential cross sections, and their matching to parton shower simulations”. In: *JHEP* 07 (2014), p. 079. DOI: 10.1007/JHEP07(2014)079. arXiv: 1405.0301 [hep-ph].
- [111] Alessandro Ballestrero et al. “PHANTOM: A Monte Carlo event generator for six parton final states at high energy colliders”. In: *Comput. Phys. Commun.* 180 (2009), pp. 401–417. DOI: 10.1016/j.cpc.2008.10.005. arXiv: 0801.3359 [hep-ph].
- [112] Olivier Mattelaer. “On the maximal use of Monte Carlo samples: re-weighting events at NLO accuracy”. In: *The European Physical Journal C* 76.12 (2016). DOI: 10.1140/epjc/s10052-016-4533-7.
- [113] Olivier Mattelaer. *Madgraph - Reweight*. URL: <https://cp3.irmp.ucl.ac.be/projects/madgraph/wiki/Reweight>.

- [114] Simone Alioli et al. “NLO vector-boson production matched with shower in POWHEG”. In: *JHEP* 07 (2008), p. 060. doi: 10.1088/1126-6708/2008/07/060. arXiv: 0805.4802 [hep-ph].
- [115] Paolo Nason. “A new method for combining NLO QCD with shower Monte Carlo algorithms”. In: *JHEP* 11 (2004), p. 040. doi: 10.1088/1126-6708/2004/11/040. arXiv: hep-ph/0409146.
- [116] Stefano Frixione, Paolo Nason, and Carlo Oleari. “Matching NLO QCD computations with parton shower simulations: the POWHEG method”. In: *JHEP* 11 (2007), p. 070. doi: 10.1088/1126-6708/2007/11/070. arXiv: 0709.2092 [hep-ph].
- [117] S. Alioli et al. “A General Framework for Implementing NLO Calculations in Shower Monte Carlo Programs: the POWHEG BOX”. In: *JHEP* 06 (2010), p. 043. doi: 10.1007/JHEP06(2010)043.
- [118] Torbjörn Sjöstrand et al. “An Introduction to PYTHIA 8.2”. In: *Computer Physics Communications* 191 (2015), pp. 159–177. doi: 10.1016/j.cpc.2015.01.024. arXiv: hep-ph/1410.3012.
- [119] P. Skands, S. Carrazza, and J. Rojo. “Tuning PYTHIA 8.1: the Monash 2013 tune”. In: *Eur. Phys. J. C* 74 (2014), p. 3024. doi: 10.1140/epjc/s10052-014-3024-y. arXiv: 1404.5630 [hep-ph].
- [120] V. Khachatryan et al. “Event generator tunes obtained from underlying event and multiparton scattering measurements”. In: *Eur. Phys. J. C* 76 (2016), p. 155. doi: 10.1140/epjc/s10052-016-3988-x. arXiv: 1512.00815 [hep-ex].
- [121] R. D. Ball et al. “Parton distributions for the LHC Run II”. In: *JHEP* 04 (2015), p. 040. doi: 10.1007/JHEP04(2015)040. arXiv: 1410.8849 [hep-ph].
- [122] Vardan Khachatryan et al. “Measurements of Inclusive W and Z Cross Sections in pp Collisions at $\sqrt{s} = 7$ TeV”. In: *JHEP* 01 (Dec. 11, 2010), p. 080. doi: 10.1007/JHEP01(2011)080. arXiv: <http://arxiv.org/abs/1012.2466v2> [hep-ex].

- [123] CMS Collaboration. “Performance of electron reconstruction and selection with the CMS detector in proton-proton collisions at $\sqrt{s} = 8$ TeV”. In: *JINST 10 (2015) P06005* (Feb. 9, 2015). DOI: 10.1088/1748-0221/10/06/P06005. arXiv: <http://arxiv.org/abs/1502.02701v2> [physics.ins-det].
- [124] Jana Novakova. “Electron Efficiency Measurement”. In: *Standard Model Measurements with the ATLAS Detector*. Springer International Publishing, 2013, pp. 31–50. DOI: 10.1007/978-3-319-00810-3_4.
- [125] R. Frühwirth. “Application of Kalman filtering to track and vertex fitting”. In: *Nuclear Instruments and Methods in Physics Research Section A: Accelerators, Spectrometers, Detectors and Associated Equipment* 262.2-3 (1987), pp. 444–450. DOI: 10.1016/0168-9002(87)90887-4.
- [126] Ilse Krätschmer. “Muon reconstruction and identification in CMS Run I and towards Run II”. In: *Nuclear and Particle Physics Proceedings* 273-275 (2016), pp. 2500–2502. DOI: 10.1016/j.nuclphysbps.2015.09.438.
- [127] CMS Collaboration. *Particle-flow commissioning with muons and electrons from J/Psi and W events at 7 TeV*. Tech. rep. CMS-PAS-PFT-10-003. CERN, 2010. URL: <https://cds.cern.ch/record/1279347>.
- [128] M. Cacciari, G. P. Salam, and G. Soyez. “The anti- k_t jet clustering algorithm”. In: *JHEP* 04 (2008), p. 063. DOI: 10.1088/1126-6708/2008/04/063. arXiv: 0802.1189 [hep-ph].
- [129] M. Cacciari, G. P. Salam, and G. Soyez. “FastJet user manual”. In: *Eur. Phys. J. C* 72 (2012), p. 1896. DOI: 10.1140/epjc/s10052-012-1896-2. arXiv: 1111.6097 [hep-ph].
- [130] M. Cacciari and G. P. Salam. “Dispelling the N^3 myth for the k_t jet-finder”. In: *Phys. Lett. B* 641 (2006), p. 57. DOI: 10.1016/j.physletb.2006.08.037. arXiv: hep-ph/0512210 [hep-ph].
- [131] Daniele Bertolini et al. “Pileup Per Particle Identification”. In: *JHEP* 10 (2014), p. 59. DOI: 10.1007/JHEP10(2014)059. arXiv: 1407.6013 [hep-ph].
- [132] Mrinal Dasgupta et al. “Towards an understanding of jet substructure”. In: *JHEP* 09 (2013), p. 029. DOI: 10.1007/JHEP09(2013)029. arXiv: 1307.0007 [hep-ph].

- [133] Andrew J. Larkoski et al. “Soft Drop”. In: *JHEP* 05 (2014), p. 146. DOI: 10.1007/JHEP05(2014)146. arXiv: 1402.2657 [hep-ph].
- [134] J. Thaler and K. Van Tilburg. “Identifying Boosted Objects with N-subjettiness”. In: *JHEP* 03 (2011), p. 015. DOI: 10.1007/JHEP03(2011)015. arXiv: 1011.2268 [hep-ph].
- [135] *MET Analysis*. CERN. URL: https://twiki.cern.ch/twiki/bin/view/CMSPublic/WorkBookMetAnalysis#Type_I_Correction.
- [136] Albert M Sirunyan et al. “Search for a heavy resonance decaying to a pair of vector bosons in the lepton plus merged jet final state at $\sqrt{s} = 13$ TeV”. In: (2018). arXiv: 1802.09407 [hep-ex].
- [137] D. L. Rainwater, R. Szalapski, and D. Zeppenfeld. “Probing color singlet exchange in $Z +$ two jet events at the CERN LHC”. In: *Phys. Rev. D* 54 (1996), p. 6680. DOI: 10.1103/PhysRevD.54.6680. arXiv: hep-ph/9605444 [hep-ph].
- [138] CMS Collaboration. “Search for massive resonances decaying into WW, WZ or ZZ bosons in proton-proton collisions at $\text{sqrt}(s) = 13$ TeV”. In: *JHEP* 03 (2017) 162 (Dec. 29, 2016). DOI: 10.1007/JHEP03(2017)162. arXiv: <http://arxiv.org/abs/1612.09159v2> [hep-ex].
- [139] CMS Collaboration. *Search for anomalous couplings in semileptonic WW and WZ decays at $\text{sqrt}(s) = 13$ TeV*. Tech. rep. CMS-PAS-SMP-16-012. CERN, 2016. URL: <http://cds.cern.ch/record/2209148>.
- [140] CMS Collaboration. “Determination of Jet Energy Calibration and Transverse Momentum Resolution in CMS”. In: *JINST* 6 (2011) 11002 (July 21, 2011). DOI: 10.1088/1748-0221/6/11/P11002. arXiv: <http://arxiv.org/abs/1107.4277v1> [physics.ins-det].
- [141] JetMET POG. *Jet Energy Resolution and Corrections (JERC) Subgroup*. Twiki Page. 2016. URL: <https://twiki.cern.ch/twiki/bin/view/CMS/JetEnergyScale>.
- [142] *W/Z-tagging of Jets*. Tech. rep. URL: <https://twiki.cern.ch/twiki/bin/viewauth/CMS/JetWtagging>.
- [143] CMS Collaboration. *Estimating Systematic Errors Due to Pileup Modeling*. Twiki Page. 2012. URL: <https://twiki.cern.ch/twiki/bin/viewauth/CMS/PileupSystematicErrors>.

- [144] Michiel Botje et al. “The PDF4LHC Working Group Interim Recommendations”. In: (Jan. 3, 2011). arXiv: <http://arxiv.org/abs/1101.0538v1> [hep-ph].
- [145] Sergey Alekhin et al. “The PDF4LHC Working Group Interim Report”. In: (Jan. 3, 2011). arXiv: <http://arxiv.org/abs/1101.0536v1> [hep-ph].
- [146] Hung-Liang Lai et al. “New parton distributions for collider physics”. In: *Physical Review D* 82.7 (Oct. 2010). DOI: [10.1103/physrevd.82.074024](https://doi.org/10.1103/physrevd.82.074024).
- [147] Richard D. Ball et al. “Impact of Heavy Quark Masses on Parton Distributions and LHC Phenomenology”. In: *Nucl.Phys.B* 849:296-363,2011 (Jan. 6, 2011). DOI: [10.1016/j.nuclphysb.2011.03.021](https://doi.org/10.1016/j.nuclphysb.2011.03.021). arXiv: <http://arxiv.org/abs/1101.1300v3> [hep-ph].
- [148] Jon Butterworth et al. “PDF4LHC recommendations for LHC Run II”. In: *J. Phys. G: Nucl. Part. Phys.* 43 023001 (2016) (Oct. 13, 2015). DOI: [10.1088/0954-3899/43/2/023001](https://doi.org/10.1088/0954-3899/43/2/023001). arXiv: <http://arxiv.org/abs/1510.03865v2> [hep-ph].
- [149] T. Junk. “Confidence level computation for combining searches with small statistics”. In: *Nucl. Instrum. Meth. A* 434 (1999), p. 435. DOI: [10.1016/S0168-9002\(99\)00498-2](https://doi.org/10.1016/S0168-9002(99)00498-2). arXiv: [hep-ex/9902006](http://arxiv.org/abs/hep-ex/9902006) [hep-ex].
- [150] A. L. Read. “Presentation of search results: the CL_s technique”. In: *J. Phys. G* 28 (2002), p. 2693. DOI: [10.1088/0954-3899/28/10/313](https://doi.org/10.1088/0954-3899/28/10/313).
- [151] Glen Cowan et al. “Asymptotic formulae for likelihood-based tests of new physics”. In: *The European Physical Journal C* 71.2 (Feb. 2011). Erratum of this article: <https://doi.org/10.1140/epjc/s10052-013-2501-z>, pp. 1–19. DOI: [10.1140/epjc/s10052-011-1554-0](https://doi.org/10.1140/epjc/s10052-011-1554-0).
- [152] M. Zaro and H. Logan. *Recommendations for the interpretation of LHC searches for H_5^0 , H_5^\pm , and $H_5^{\pm\pm}$ in vector boson fusion with decays to vector boson pairs*. CERN Report LHCHXSWG-2015-001. 2015. URL: <https://cds.cern.ch/record/2002500>.
- [153] M Wallmark et al. “Operating range of a gas electron multiplier for portal imaging”. In: *Nuclear Instruments and Methods in Physics Research Section A: Accelerators, Spectrometers, Detectors and Associated Equipment* 471.1-2 (2001), pp. 151–155. DOI: [10.1016/s0168-9002\(01\)00980-9](https://doi.org/10.1016/s0168-9002(01)00980-9).

- [154] Edward Tsyganov et al. “Gas Electron Multiplying Detectors for medical applications”. In: *Nuclear Instruments and Methods in Physics Research Section A: Accelerators, Spectrometers, Detectors and Associated Equipment* 597.2-3 (2008), pp. 257–265. DOI: 10.1016/j.nima.2008.09.002.
- [155] Ronald A. Remillard et al. “Gas electron multiplier (GEM) detectors for an advanced x-ray monitor”. In: *X-Ray and Gamma-Ray Instrumentation for Astronomy XI*. Ed. by Kathryn A. Flanagan and Oswald H. W. Siegmund. SPIE, 2000. DOI: 10.1117/12.409152.
- [156] K. Gnanvo et al. “Detection and Imaging of High-Z Materials with a Muon Tomography Station Using GEM Detectors”. In: (Nov. 14, 2010). DOI: 10.1109/NSSMIC.2010.5873822. arXiv: <http://arxiv.org/abs/1011.3231v2> [physics.ins-det].